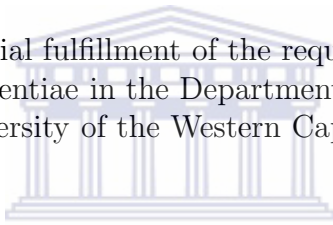

DEVELOPING A SORTING CODE
FOR COULOMB EXCITATION
DATA ANALYSIS

Craig Mehl

A thesis submitted in partial fulfillment of the requirements for the degree
of Magister Scientiae in the Department of Physics,
University of the Western Cape



Supervisor: Prof. J. N. Orce, University of the Western Cape

Co-supervisor: Dr. P. M. Jones, iThemba LABS

Co-supervisor: Prof. S. Triambak, University of the Western
Cape

November 2015

KEYWORDS

Coulomb excitation

Semiclassical approximation

Reorientation effect

Sorting code

S3 detector

AFRODITE array

MTsort

MIDAS

Gosia simulation

iThemba LABS



Abstract

This thesis aims at developing a sorting code for Coulomb excitation studies at iThemba LABS. In Coulomb excitation reactions, the inelastic scattering of the projectile transfers energy to the partner nucleus (and vice-versa) through a time-dependent electromagnetic field. At energies well below the Coulomb barrier, the particles interact solely through the well known electromagnetic interaction, thereby excluding nuclear excitations from the process [2], [3]. The data can therefore be analyzed using a semiclassical approximation.

The sorting code was used to process and analyze data acquired from the Coulomb excitation of ^{20}Ne beams at 73 and 96 MeV, onto a ^{194}Pt target. The detection of gamma rays was done using the AFRODITE HPGe clover detector array, which consists of nine clover detectors, in coincidence with the ^{20}Ne particles detected with an S3 double-sided silicon detector. The new sorting code includes Doppler-correction effects, charge-sharing, energy and time conditions, kinematics and stopping powers, among others, and can be used for any particle- γ coincidence measurements at iThemba LABS. Results from other Coulomb excitation measurements at iThemba LABS will also be presented.

Declaration

I declare that *DEVELOPING A SORTING CODE FOR COULOMB EXCITATION DATA ANALYSIS* is my own work, that it has not been submitted for any degree or examination in any other university, and that all sources I have used or quoted have been indicated and acknowledged by complete references.



Craig Mehl

November 2015

Signature:

Acknowledgments

I wish to express my sincere gratitude to the following for making the realization of this thesis possible:

- The Almighty **GOD** for His grace.
- Prof J. N. Orce for the opportunity to do this work, and for the continuous support, guidance, training, expertise and active involvement in the contribution to the final preparation of this work. Thank you Prof.
- Dr P. M. Jones for the expertise, training and active involvement in the contribution to the final preparation of this work. Thank you Dr.
- Prof S. Triambak for the expertise and active involvement in the contribution to the final preparation of this work. Thank you Prof.
- Dr M. Kumar Raju for the discussions and active involvement in the contribution to the final preparation of this work.
- Mr N. Erasmus for the assistance with the Geant simulations.
- Dr D. Negi and Prof P. Papka for the expertise and assistance with data analysis software.
- Dr S. Majola, Dr T. Dinoko and Ms N. Khumalo for the assistance with the preliminary data analysis procedures.
- The collaborators of the PR181B and PR181C experiments: M. Wiedeking, C. Swartz, J. N. Orce, D. Negi, P. Papka, E. Lawrie, J. Lawrie, T. Dinoko, P. Jones, S. Majola, V. Kheswa, B. Singh, S. Triambak, D. Butcher and N. Erasmus.
- Mr M. Mokgolobotho, Mr B. Singh, Mr G. Andrews, Mr W. Jacobus and fellow comrades.
- The Physics department at UWC and iThemba LABS for the opportunity to this work.
- The National Research Foundation for the financial support.
- My Parents and family for the support and sacrifices.

Contents

1	Introduction	1
1.1	Scientific motivation	4
2	Coulomb excitation theory	10
2.1	Semiclassical approximation	11
2.1.1	Rutherford scattering	11
2.2	Time-dependent perturbation theory	13
2.3	<i>Gosia</i> simulations	21
2.3.1	Coupled channel method	21
2.3.2	Calculation of γ -ray intensities	22
2.3.3	Count rate calculations	24
3	Experimental details	26
3.1	The S3 Detector	26
3.2	HPGe clover detectors	27
3.2.1	Modes of operation	28
3.3	The AFRODITE array	29
3.4	Electronics	29
3.5	Digital data acquisition system	32
3.6	Preliminary experimental considerations	34
3.6.1	Maximum safe bombarding energy criteria	34
3.7	Results of the <i>Gosia</i> simulation	35
3.8	The $^{194}\text{Pt}(^{20}\text{Ne}, ^{20}\text{Ne}^*)^{194}\text{Pt}^*$ experiment	37
3.8.1	$^{194}\text{Pt}(^{20}\text{Ne}, ^{20}\text{Ne}^*)^{194}\text{Pt}^*$ experiment at backward angles	37
3.8.2	$^{194}\text{Pt}(^{20}\text{Ne}, ^{20}\text{Ne}^*)^{194}\text{Pt}^*$ experiment at forward angles	38
3.9	The $^{208}\text{Pb}(^{40}\text{Ar}, ^{40}\text{Ar}^*)^{208}\text{Pb}^*$ experiment	38
4	Data analysis and sorting code	41
4.1	Calibrations	41
4.1.1	Efficiency calibration	41
4.1.2	HPGe clover detector energy calibrations	44

4.1.3	S3 detector energy calibrations	44
4.2	<i>GEANT4</i> simulations	45
4.3	Particle energy loss	47
4.4	Sorting code	49
4.4.1	Particle coincidence conditions	49
4.4.2	Particle- γ coincidence conditions	50
4.4.3	Energy sharing condition	51
4.4.4	Inelastic conditions	53
4.4.5	Doppler corrections	54
5	Results and Discussion	57
5.1	The $^{194}\text{Pt}(^{20}\text{Ne}, ^{20}\text{Ne}^*)^{194}\text{Pt}^*$ experiment	57
5.1.1	$^{194}\text{Pt}(^{20}\text{Ne}, ^{20}\text{Ne}^*)^{194}\text{Pt}^*$ experiment at backward angles	58
5.1.2	$^{194}\text{Pt}(^{20}\text{Ne}, ^{20}\text{Ne}^*)^{194}\text{Pt}^*$ experiment at forward angles	63
5.2	The $^{208}\text{Pb}(^{40}\text{Ar}, ^{40}\text{Ar}^*)^{208}\text{Pb}^*$ experiment	66
5.3	Discussions	69
6	Conclusion	72
	Appendices	74
A	Development of sort codes	75
A.1	Introduction	75
A.2	Installation	75
A.3	Sorting code options	75
A.3.1	Online sorting code	76
A.3.2	Offline sorting code for calibrations	76
A.3.3	Sorting code optimized for Coulomb excitation	77
A.3.4	Clover detector geometry	77
A.4	Input file	78
A.5	Data files	79
A.6	Examples of generated sortfiles	79
A.6.1	Online sorting code (option 1 example)	79
A.6.2	Offline sorting code for calibrations (option 2 example)	88
A.6.3	Offline sorting code (basic option 3 example)	100
A.7	Input file example	121
B	Non-relativistic kinematics	122

C S3 detector tables	127
C.1 S3 detector ring radii	128
C.2 S3 detector cabling	129
C.2.1 Ring cabling	129
C.2.2 Sector cabling	130
C.3 <i>MIDAS</i> digital parameters	131



List of Figures

1.1	Charge distributions in the intrinsic frame.	2
1.2	Experimental and calculated $Q_S(2_1^+)$ values	4
1.3	r_q vs A for even-A even-Z nuclei for $20 \leq A \leq 208$	5
1.4	$\frac{E(4^+)}{E(2^+)}$ vs A for even-A even-Z nuclei for $20 \leq A \leq 208$	6
1.5	Clustering transition in fermionic systems	7
1.6	Q_α values for 4n self-conjugate nuclei	7
1.7	^{20}Ne DD-ME2 and Skyrme SLy4 EDF calculations	8
2.1	Rutherford scattering trajectory.	12
2.2	The reorientation effect.	18
3.1	Schematic of the S3 double-sided silicon detector.	27
3.2	Schematic of the front face of an HPGe clover detector.	28
3.3	The AFRODITE HPGe clover detector array.	29
3.4	MHV-4 bias unit and MSCF-16 F	30
3.5	MPR-32 multichannel preamplifiers	30
3.6	Schematic of electronics setup.	31
3.7	Schematic of the DDAS.	33
3.8	$s(\vartheta)$ as a function of average ϑ	35
3.9	Integrated yields calculated with <i>Gosia</i> at backward angles	36
3.10	Integrated yields calculated with <i>Gosia</i> at forward angles.	36
3.11	The S3 detector (left) and the AFRODITE array (right).	37
3.12	Shielding setup for the $^{208}\text{Pb}(^{40}\text{Ar}, ^{40}\text{Ar}^*)^{208}\text{Pb}^*$ experiment.	39
4.1	Singles γ -ray spectrum of ^{56}Co source.	42
4.2	Singles γ -ray spectrum for the ^{152}Eu source.	42
4.3	HPGe clover detector efficiency calibration.	43
4.4	Particle spectra for the seven innermost rings	45
4.5	Kinematics and GEANT4 predicted energies	46
4.6	center of target scattering event.	47
4.7	Particle coincidence gates used to remove background.	49

4.8	Particle- γ $\Delta t'$ spectrum	50
4.9	2D particle energy histogram.	51
4.10	2D Energy sharing histograms	52
4.11	Inelastic particle tagging.	53
4.12	Coordinate system used for the Doppler Correction.	54
4.13	S3 detector (θ, ϕ) angles.	56
5.1	Singles γ -ray energy spectrum for the $^{194}\text{Pt}(^{20}\text{Ne}, ^{20}\text{Ne}^*)^{194}\text{Pt}^*$	57
5.2	Broad particle energy gate	58
5.3	Raw (left) and improved (right) particle $\Delta t'$ spectra.	59
5.4	2D histograms for particle- γ histograms.	60
5.5	Improved particle (left) and particle- γ (right) $\Delta t'$ spectra.	61
5.6	Non-Doppler corrected γ -ray spectrum at backward angles.	62
5.7	Doppler corrected γ -ray spectrum at backward angles.	62
5.8	Singles γ -ray energy spectrum for the $^{194}\text{Pt}(^{20}\text{Ne}, ^{20}\text{Ne}^*)^{194}\text{Pt}^*$	63
5.9	^{20}Ne broad particle energy gate at 96 MeV.	64
5.10	^{20}Ne no Doppler correction at 96 MeV.	65
5.11	^{20}Ne Doppler correction at 96 MeV.	65
5.12	^{40}Ar broad particle energy gate at 96 MeV.	66
5.13	Particle (left) and particle- γ (right) $\Delta t'$ spectra.	67
5.14	^{40}Ar no Doppler correction.	68
5.15	^{40}Ar Doppler correction.	68
5.16	2D ring- γ energy histogram.	69
5.17	Effect of coincidence conditions.	70
5.18	2D ring- γ energy histogram.	71
A.1	Execution order of programs	79
B.1	Two-body scattering	123
B.2	Lab and CM frame angles.	125

List of Tables

1.1	Experimental determinations of $Q_S(2_1^+)$	5
3.1	Geometry of the AFRODITE array	38
3.2	Geometry of the AFRODITE array	39
4.1	Fit parameters for efficiency calibration.	43
A.1	Input file format	78



Chapter 1

Introduction

The study of nuclear structure through Coulomb excitation measurements has played a pivotal role in the advancement of our understanding of fundamental nuclear properties such as nuclear shapes and nuclear collectivity. Coulomb excitation is the excitation of nuclei solely through the electromagnetic interaction. In order to perform such measurements, certain experimental precautions need to be taken to ensure that contributions from nuclear excitation are negligible. Although the results of such investigations have been well documented over the past few decades, the accuracy and precision to which the results of such measurements could be determined were in many cases limited by the technology available at that time.

With the recent advancements in radiation and particle detector technology, particle accelerators, computational power and the production of heavy ion beams, these measurements can now be made with greater accuracy and precision. As a consequence, Coulomb excitation studies have received much attention in recent years, primarily because the technique can be used to distinguish between nuclear shapes directly [1]. The simplest nuclear shape that has been investigated in the laboratory frame is the electric quadrupole moment of ground states and the first excited states in even A - even Z nuclei. The electric quadrupole moment of a nucleus is a measure of the extent to which the shape of the nucleus under investigation, deviates from that of a sphere. The electric quadrupole operator, \hat{Q} , is defined as follows [2]

$$e\hat{Q} = \sqrt{\frac{16\pi}{5}} \int r^2 Y_{20}(\theta, \phi) \rho(\vec{r}) dV, \quad (1.1)$$

here e denotes the elementary charge, (r, θ, ϕ) are the nuclear spherical coordinates, $\rho(\vec{r})$, the nuclear charge distribution and Y_{20} a spherical harmonic.

The expectation value of this operator with respect to the intrinsic or the center of mass frame of the nucleus, Q_0 , is referred to as the intrinsic quadrupole moment

$$Q_0 = \langle \hat{Q} \rangle_{intrinsic}. \quad (1.2)$$

The expectation value of \hat{Q} in the laboratory frame, $Q_S(J^\pi)$, is referred to as the spectroscopic quadrupole moment.

$$Q_S(J^\pi) = \langle \hat{Q} \rangle_{lab}, \quad (1.3)$$

where J denotes the spin of the state at which the spectroscopic quadrupole moment is evaluated and π denotes the parity. The relation between the intrinsic quadrupole moment and the deviation from spherical symmetry yields the shapes in figure 1.1

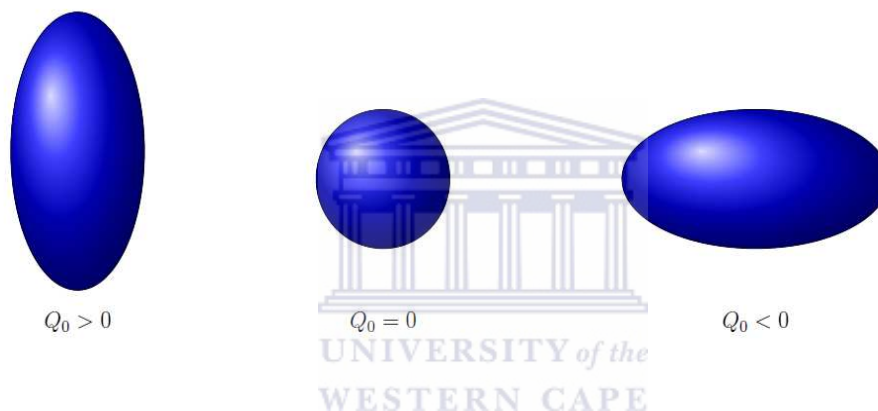


Figure 1.1: Prolate (left), spherical (center) and oblate (right) charge distributions in the intrinsic frame.

Figure 1.1 shows the dependence of the nuclear shape on the sign of Q_0 . A positive value of Q_0 corresponds to a prolate distribution (left), a negative value corresponds to an oblate distribution, and $Q_0 = 0$ corresponds to a spherical distribution for $J \neq 0$ or $J \geq \frac{1}{2}$ [3] or equal probabilities for prolate and oblate distributions. In order to compare the values of Q_0 and Q_S for a particular nucleus, Q_S can be converted to Q_0 by invoking some nuclear model, such as the collective model, where the nucleus is assumed to be an axially symmetric rotor [4]. Within this model, Q_0 is used as a parameter that relates $Q_S(2_1^+)$ to the value of the reduced transition probability, $B(E2, 0_1^+ \rightarrow 2_1^+)$, for an electric excitation of multipole order 2 as follows [5], [6]

$$B(E2, 0_1^+ \rightarrow 2_1^+) = \frac{5}{16\pi} Q_0^2. \quad (1.4)$$

Within the rotational model [4], the intrinsic and spectroscopic quadrupole moments are related by

$$Q_S(2_1^+) = \frac{3K^2 - J(J+1)}{(2J+3)(J+1)} Q_0(2_1^+), \quad (1.5)$$

where K denotes the projection of the total angular momentum onto the axis of symmetry [4] which reduces to

$$Q_S(2_1^+) = -\frac{2}{7} Q_0, \quad (1.6)$$

for $K = 0$ and $J = 2$. Thus, measurements of Q_S can be used to discriminate between the predictions of various nuclear models [7]. Among the various experimental methods that have been used to determine Q_S values of various nuclei, the reorientation effect (RE) in Coulomb excitation, has been found to be one of the most reliable methods [2]. The RE relates the Coulomb excitation probability with Q_S . In earlier work, this method also provided some unreliable results, which have been useful in providing valuable information on the precautions and corrections that should be considered when performing such experiments [2]. The RE will be explained in Chapter 2.

A new setup at the iThemba LABS facility has recently been built to conduct the first series of Coulomb excitation experiments with the combination of the AFRODITE HPGe clover detector array and double-sided silicon detectors. The scientific motivation behind these experiments will now be presented.

1.1 Scientific motivation

At present the current nuclear collective and mean field models such as the shell model [2] and Hartree-Fock-Bogoliubov [2] have not been successful in calculating the $Q_S(2_1^+)$ value at 1.634 MeV in ^{20}Ne . In particular, the magnitude of the calculated values were found to be about 30 % [2] less than the accepted values obtained experimentally using the RE [2]. Figure 1.2 shows the predicted $Q_S(2_1^+)$ values in ^{20}Ne and ^{40}Ar together with the accepted experimental values in units of $\text{e}\cdot\text{fm}^2$.

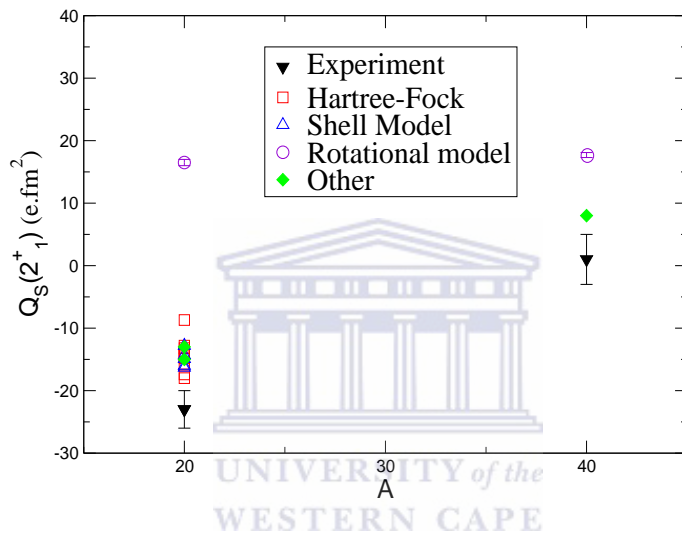


Figure 1.2: Experimental and calculated $Q_S(2_1^+)$ values in ^{20}Ne and ^{40}Ar [2].

To date only three RE measurements were made in ^{20}Ne [8], [9], [10]. This scarce information was due to the difficulty associated with the production of Ne ion beams in Tandem accelerators. Table 1.1 shows the experimental determinations of $Q_S(2_1^+)$ in ^{20}Ne performed using the RE in Coulomb excitation measurements. As shown in Table 1.1, two of the three previous RE measurements possessed high bombarding beam energies that were associated with the separation between nuclear surfaces, s_{min} , equal to 3.8 and 4.2 fm [2]. In addition, these measurements failed to show that the maximum bombarding beam energies could be deemed as safe [2]. For light nuclei, Spear [2] showed that $s_{min} \geq 6.5$ fm.

Author	Year	$Q_S(2_1^+)$ (e·fm ²)	Projectile/Target	s_{min} (fm)
Nakai	1970	-24 ± 3	$^{20}\text{Ne}/^{120}\text{Sn}, ^{130}\text{Te}, ^{148}\text{Sm}$	3.8
Schwalm	1972	-23 ± 8	$^{32}\text{S}/^{20}\text{Ne}$	7.1
Olsen	1974	-20 ± 5	$^{20}\text{Ne}/\text{Pt}, \text{Au}$	4.2
Adopted value:		-23 ± 8 e·fm ²		

Table 1.1: Experimental determinations of $Q_S(2_1^+)$ values in ^{20}Ne using the RE, [[2] [8], [9], [10]].

The only RE measurement of $Q_S(2_1^+)$ using safe energies was done by Schwalm and co-workers [9] (Table 1.1). In addition, the RE coefficient for target excitation is proportional to $\frac{A_p}{Z_t}$, thus the RE is larger for projectile excitation if a target with a higher Z value is used. Accordingly, the accepted value for $Q_S(2_1^+)$ should be -23 ± 8 e·fm². A smaller RE coefficient for target excitation gives rise to further corrections and uncertainties of comparable size, hence the large uncertainty associated with the measurement done by Schwalm and collaborators [2], [9]. In addition, the ratio of $Q_S(2_1^+)$ to the value obtained from the $B(E2)$, using the collective model of Bohr and Mottelson [4], $Q_S(2_1^+)_B$, is given by equation,

$$Q_S(2_1^+)_B = \pm \sqrt{\frac{16\pi}{5}} \frac{\sqrt{B(E2)_{J_i \rightarrow J_f}}}{|(J_i, 2, K, 0 | J_f, K)|}, \quad (1.7)$$

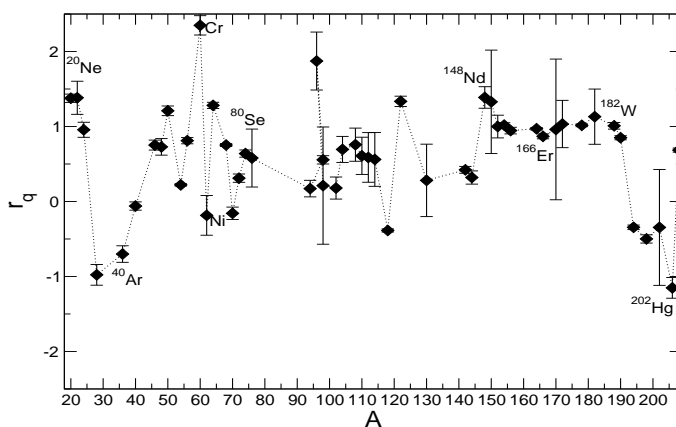


Figure 1.3: r_q vs A for even- A even- Z nuclei with $20 \leq A \leq 208$ [11], [12].

assumes that the nucleus is a symmetric rotor. This ratio is defined as the spectroscopic quadrupole ratio, r_q , where $\langle J_i, 2, K, 0 | J_f, K \rangle$ denotes a Clebsch-Gordan coefficient. In the case of a transition from the ground state where $J_i = 0$ to an $J_f = 2$ state, the coefficient reduces to one. For the $K = 0$ ground state band, r_q , is given by [6]

$$r_q = \frac{Q_S(2_1^+)}{Q_S(2_1^+)_B} = -\frac{7}{8} \sqrt{\frac{5}{\pi}} \frac{Q_S(2_1^+)}{\sqrt{B(E2)}} \quad (1.8)$$

which as shown in figure 1.3, takes on a value that is approximately equivalent to one for an axially symmetric rotor [5]. Figure 1.3 shows a plot of r_q vs A for even- A even- Z nuclei, ranging from $A = 20$ to $A = 208$ [11], [12].

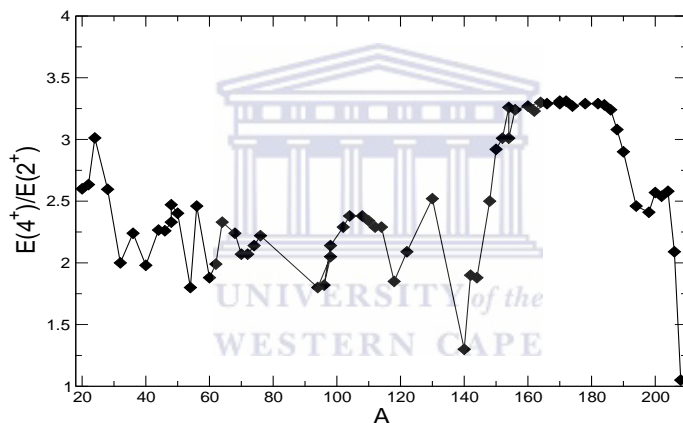


Figure 1.4: $\frac{E(4^+)}{E(2^+)}$ vs A for even- A even- Z nuclei for $20 \leq A \leq 208$ [13]

A large value of $r_q \approx 1.4$ is determined for ^{20}Ne [6]. This value is consistent with a rotor because of the large uncertainty, as shown in figure 1.3. Figure 1.4 shows a plot of $\frac{E(4^+)}{E(2^+)}$ vs A for even-even nuclei with $20 \leq A \leq 208$ [13]. However, a value of 2.6 for the ratio of the energies of the first 4^+ to 2^+ states is determined for ^{20}Ne [6], whereas $\frac{E(4^+)}{E(2^+)} = 3.33$ for an axially symmetric rotor [5], and $\frac{E(4^+)}{E(2^+)} = 2$ for a spherical vibrator.

Furthermore, predictions that the nucleus ^{20}Ne possesses super-deformed cluster states in which the ratio of the oscillations that are perpendicular, and

parallel to the deformation axis is two to one, have been made using a cluster model based on the harmonic oscillator [14]. As shown in figure 1.5, clustering in fermionic systems can be considered as a transitional phenomenon between crystalline and quantum-liquid phases [15].

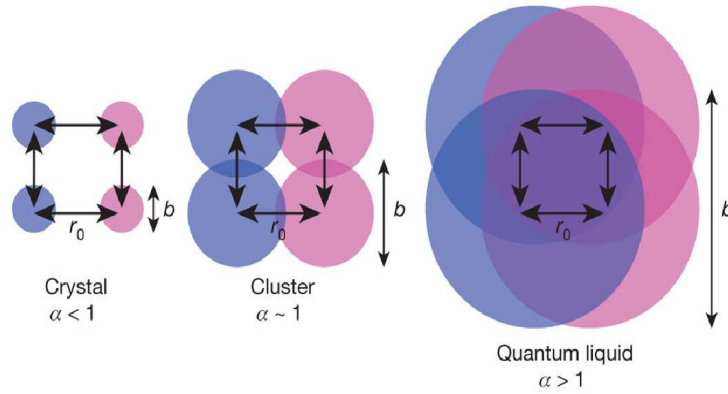


Figure 1.5: Clustering transition in fermionic systems [15].

Morinaga [16] postulated that the gradual emergence of clustering phenomena is likely to occur as the internal energy of the nucleus increases.

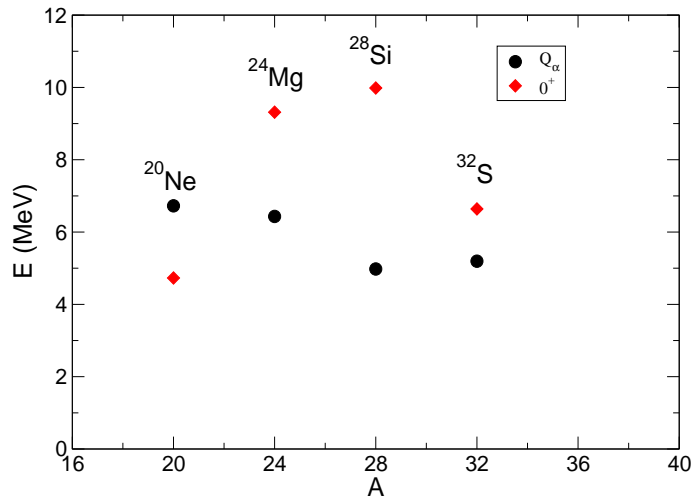


Figure 1.6: Q_α values for $4n$ self-conjugate nuclei in the sd -shell between shell closures.

It has been suggested that the fully realized cluster should appear when the binding energy of the clustering state, ($J^\pi = 0^+$) is within close proximity to the α -decay threshold, Q_α [14]. Figure 1.6 shows a plot in which the binding energy of the second 0^+ states, 0_2^+ , and Q_α values are plotted as a function of A for $4n$ self-conjugate nuclei in the sd-shell between shell closures [14]. As shown in figure 1.6, the Q_α values ^{24}Mg , ^{28}Si and ^{32}S lie above the binding energies of the 0_2^+ states. For these nuclei, the experimental $Q_S(2_1^+)$ values are in agreement with those predicted by the mean field and collective models. In the case of ^{20}Ne , the Q_α value lies below the binding energy of the 0_2^+ state. It has been suggested that ^{20}Ne is one of the best examples of a light nucleus in which the clustering phenomenon is manifested [14].

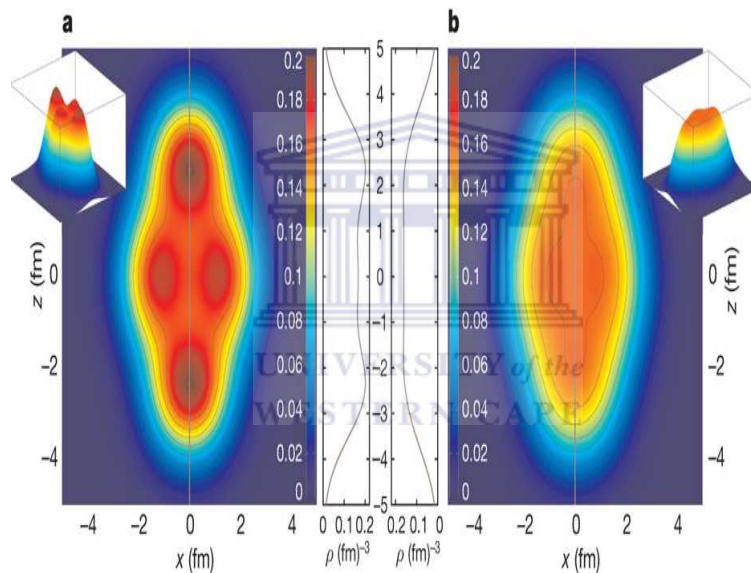


Figure 1.7: DD-ME2 (left) and Skyrme SLy4 (right) EDF calculations for the ground state of ^{20}Ne [15].

Figure 1.7 shows the self-consistent ground-state densities of ^{20}Ne that have been calculated using energy density functional theory [15]. In particular, it shows the single nucleon densities for ^{20}Ne predicted by two energy density functional (EDF) calculations. The plot on the left was calculated with the relativistic DD-ME2 EDF [15], [18], in this case, the formation of cluster structures is already observed in the ground state. The second, is the non-relativistic Skyrme SLy4 EDF [15], [19]. As shown on the right of figure

1.7, the Skyrme SLy4 EDF predicts a smooth behavior analogous to that of a Fermi-liquid [15]. These results, together with the large $\rho^2(E0) \times 10^3$ values obtained from the E0 matrix elements determined through (e,e') experiments, which suggest shape mixing of states with $J^\pi = 0^+$ [17]. This would support the idea of a cluster structure for the 2_1^+ in ^{20}Ne , proposed by Morinaga [16].

The purpose of this work is the development of a sorting code for Coulomb excitation data analysis, that can be used for online and offline data analysis of Coulomb excitation measurements at the iThemba LABS. The rest of the thesis aims at the sorting and data analysis of the $^{194}\text{Pt}(^{20}\text{Ne}, ^{20}\text{Ne}^*)^{194}\text{Pt}^*$ and $^{208}\text{Pb}(^{40}\text{Ar}, ^{40}\text{Ar}^*)^{208}\text{Pb}^*$ experiments, which were the first ones performed at iThemba LABS, using the AFRODITE HPGe Clover detector array and an S3 double sided silicon detector.

The theoretical background of the Coulomb excitation that was considered in the planning of the experiments discussed here will be presented in chapter two. The experimental setup is discussed in chapter three. Chapter four addresses the data analysis and the conditions implemented in the sorting code to perform the analysis. The fifth chapter presents the results of the data analysis as well as a discussion of the results. The sixth and final chapter presents the concluding remarks and the future work. The appendix contains information on how to generate the sorting codes, as well as other information related to this work.

Chapter 2

Coulomb excitation theory

Coulomb excitation is referred to as the inelastic scattering process between an incident charged particle and a target nucleus that results in the transfer of energy to the projectile and target nuclei through a time-dependent electromagnetic interaction. This process describes the excitation of nuclei induced by the bombarding projectile at beam energies, chosen so that the separation between nuclear surfaces, $s_{min} \geq 6.5$ fm (for light nuclei) to exclude the contributions of nuclear excitations. If this condition is satisfied, the projectile and target nuclei interact solely through the electromagnetic interaction. Coulomb excitation is a well known experimental technique and can be used to probe the collective structure of the nucleus.

Various approximations can be used to simplify the quantitative description of the Coulomb excitation. As such, the validity of these approximations, as well as their applicability are governed by various experimental parameters; whose mathematical expressions depend directly on the values of well-known spectroscopic quantities such as the beam energy, the masses and charge numbers of the beam and target, and various kinematic variables. The first of these parameters is the Sommerfeld parameter, η , which is defined as the ratio between the distance of closest approach in head-on-collision, a^1 , and the reduced de Broglie wavelength, λ . In the c.g.s system,

$$\eta = \frac{a}{\lambda} = \frac{Z_p Z_t e^2}{\hbar v_p}, \quad (2.1)$$

where $\lambda = \frac{\lambda}{2\pi}$, v_p denotes the initial velocity of the projectile, while Z_p and Z_t denote the charge of the projectile and target, respectively, and $e^2=1.44$

¹ a is half the distance of closest approach in a head-on collision, at which the potential energy of the projectile and target system equals the kinetic energy in the center of mass frame, that is $\frac{Z_p Z_t e^2}{b} = \frac{\mu v_p^2}{2}$, so $a = \frac{b}{2}$.

MeV·fm. For $\eta \ll 1$ the excitation mechanism is described by the Born approximation [21]. For $\eta \gg 1$, the Coulomb excitation process can be described by the semiclassical approximation [21], which will now be discussed.

2.1 Semiclassical approximation

Within the semiclassical approximation, the trajectory of the projectile particle is assumed to follow the classical Rutherford hyperbolic trajectory, while the excitation process is treated using time-dependent perturbation theory [21].

2.1.1 Rutherford scattering

The elastic scattering process between two charged particles is referred to as Rutherford scattering. Figure 2.1 shows a schematic of the Rutherford scattering trajectory of a projectile, where m_p and m_t denote the mass of the projectile and target, respectively, $\vec{b}(\vartheta)$ is the impact parameter, and ϑ the scattering angle in the center of mass frame. Since the collision is elastic, the charged particles interact through the Coulomb interaction. When the projectile approaches the target nucleus, the projectile moves along a hyperbolic trajectory as shown in figure 2.1. In this case, the Lagrangian for the system in the center of mass frame, \mathcal{L} , is given by

$$\mathcal{L} = \frac{1}{2}\mu\dot{r}^2 + \frac{Z_p Z_t e^2}{r}. \quad (2.2)$$

Here $\mu = \frac{m_p m_t}{m_p + m_t}$ denotes the reduced mass of the system. Since the Coulomb field depends only on the radial distance between the two particles, the Coulomb force \vec{F} , between the two particles is parallel to \vec{r} (figure 2.1). In this case the moment of \vec{F} acting on the projectile particle, $\vec{\tau} = \vec{r} \times \vec{F} = 0$,

$$\vec{\tau} = \frac{d\vec{L}}{dt} = \vec{0}, \quad (2.3)$$

where \vec{L} denotes the angular momentum of the projectile particle about any fixed point, \vec{r}_0 . Thus, \vec{L} is constant and the projectile particle will be confined to the plane, given by

$$(\vec{r} - \vec{r}_0) \cdot \vec{L} = 0. \quad (2.4)$$

These observations can be used to obtain explicit expressions for the trajectory of the projectile. In Coulomb excitation experiments the quantities of

interest are the deflection angle, ϑ , the impact parameter, b , and the Rutherford differential cross section, $\frac{d\sigma_R}{d\Omega}$, since these parameters can be varied experimentally to ensure that the projectile follows a hyperbolic trajectory. In addition, knowledge on the projectile trajectory can be used to determine whether or not nuclear excitations are present.

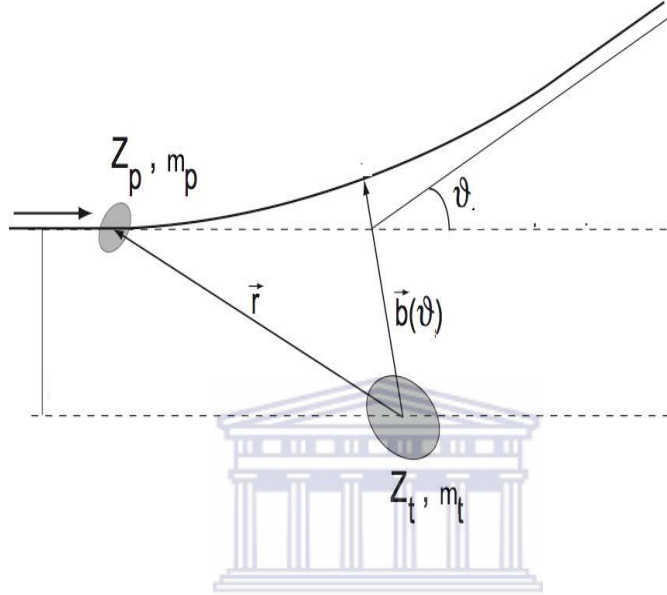


Figure 2.1: Rutherford scattering trajectory.

By solving the Lagrange equations of motion for equation 2.2, $b(\vartheta)$ can be written as

$$b(\vartheta) = \frac{a}{2} \cot \frac{\vartheta}{2}. \quad (2.5)$$

From equation 2.5 it follows that $b(\vartheta)$ is maximum for values of $\vartheta \in (0, \frac{\pi}{2})$ and minimum for $\vartheta \in (\frac{\pi}{2}, \pi)$. In addition, for a given beam energy and distance to the particle detector, $b(\vartheta)$ can be increased by using a heavier target.

Rutherford scattering cross-section

Using the expression for $b(\vartheta)$ given in equation 2.5, the expression for the Rutherford differential cross-section can be deduced by considering the probability of scattering between ϑ and $\vartheta + d\vartheta$. This probability will be proportional to the area of a ring of radius b , and thickness, db , in which case $\frac{d\sigma_R}{d\Omega}$

in the center of mass frame is given by [21],

$$\frac{d\sigma_R}{d\Omega} = \left(\frac{a}{2}\right)^2 \frac{1}{\sin^4 \frac{\vartheta}{2}}. \quad (2.6)$$

2.2 Time-dependent perturbation theory

The differential cross-section for Coulomb excitation, $\frac{d\sigma_C}{d\Omega}$, is related to the $\frac{d\sigma_R}{d\Omega}$ given by equation (2.6), through the probability that the incident beam or target is excited through a time-dependent electromagnetic interaction, $P_{i \rightarrow f}$, from a initial state, $|i\rangle = |J_i, m_i\rangle$, to a final state $|f\rangle = |J_f, m_f\rangle$, which can be expressed as [21]

$$P_{i \rightarrow f} = \frac{1}{2J_i + 1} \sum_{m_i = -J_i}^{J_i} \sum_{m_f = -J_f}^{J_f} |c_{if}|^2; \quad (2.7)$$

where J_i and J_f denote the initial and final spin of the nuclear states, m_i and m_f , the corresponding magnetic substates and c_{if} , the time-dependent transition amplitudes. If $P_{i \rightarrow f}$ for a single encounter is much less than one the explicit expressions for these transition amplitudes can be obtained using first-order time-dependent perturbation theory [21].

If the nucleus which undergoes Coulomb excitation is in a state, $|i\rangle$, at $t = -\infty$, the time-dependent transition amplitudes can be obtained by solving the following system of differential equations,

$$\frac{dc_f(t)}{dt} = -\frac{i}{\hbar} \sum_i \langle i | V(t) | f \rangle e^{\frac{i}{\hbar}(E_f - E_i)t} c_i(t). \quad (2.8)$$

At non-relativistic energies, only the electric excitations are considered, hence the time-dependent potential, $V(t)$, can be obtained by expressing the classical expression for $V(t)$ as the sum of electric multipoles [21]

$$V(t) = Z_p e \int \frac{\rho_n(\vec{r})}{r_p} \sum_{\lambda=0}^{\infty} \left(\frac{r}{r_p}\right)^\lambda P_\lambda(\cos(\gamma)) d\tau, \quad (2.9)$$

where r_p is the position of the projectile in the center of mass frame of the nucleus, ρ_n the nuclear charge density operator and γ denotes the angle between r and r_p . By using the addition theorem for spherical harmonics, $P_\lambda(\cos(\gamma))$ can be expressed as [21]

$$P_\lambda(\cos(\gamma)) = \frac{4\pi}{2\lambda + 1} \sum_{\mu=-\lambda}^{\lambda} Y_\lambda^\mu(\theta, \phi) Y_\lambda^\mu(\theta_p, \phi_p). \quad (2.10)$$

Now by inserting equation 2.10 in equation 2.9, $V(t)$ can be written as [21],

$$V(t) = 4\pi Z_p e \sum_{\lambda=1}^{\infty} \sum_{\mu=-\lambda}^{\lambda} \frac{1}{2\lambda+1} \left(\frac{1}{r_p}\right)^{\lambda+1} Y_{\lambda}^{\mu}(\theta_p, \phi_p) \left(\int r^{\lambda} \rho_n(\vec{r}) Y_{\lambda}^{\mu}(\theta, \phi) d\tau \right)^*, \quad (2.11)$$

by noting that [21]

$$\left(\int r^{\lambda} \rho_n(\vec{r}) Y_{\lambda}^{\mu}(\theta, \phi) d\tau \right)^* = (\hat{M}(E\lambda, \mu))^*, \quad (2.12)$$

where ‘*’, denotes the complex conjugate of the electric multipole moment operator $\hat{M}(E\lambda, \mu)$, given by

$$\hat{M}(E\lambda, \mu) = \int r^{\lambda} \rho_n(\vec{r}) Y_{\lambda}^{\mu}(\theta, \phi) d\tau. \quad (2.13)$$

Equations 2.8 to 2.13 can be used in conjunction with the expression for $V(t)$, given in equation 2.11 to express c_{if} in the following manner [21]

$$c_{if} = \frac{4\pi Z_p e}{i\hbar} \sum_{\lambda=1}^{\infty} \sum_{\mu=-\lambda}^{\lambda} \frac{1}{2\lambda+1} \langle i | \hat{M}(E\lambda, \mu) | f \rangle \left(\int_{-\infty}^{\infty} \left[\left(\frac{1}{r_p}\right)^{\lambda+1} Y_{\lambda}^{\mu}(\theta_p, \phi_p) e^{i\omega_{if}t} \right] dt \right), \quad (2.14)$$

where $\omega_{if} = \frac{E_f - E_i}{\hbar}$. The fact that the electric multipole operators are spherical tensors can be used in conjunction with the Wigner-Eckart theorem [22] to express $\hat{M}(E\lambda, \mu)$ as a product of a Clebsch-Gordan coefficient and the reduced matrix element $\langle J_i || \hat{M}(E\lambda) || J_f \rangle$. The latter is related to the reduced transition probability of a electric multipole of order λ , $B(E\lambda, J_i \rightarrow J_f)$, by [21]

$$B(E\lambda, J_i \rightarrow J_f) = \frac{|\langle J_i || \hat{M}(E\lambda) || J_f \rangle|^2}{2J_i + 1}. \quad (2.15)$$

Since the transition occurs from the initial state $|i\rangle$ to the final state $|f\rangle$, only one term will contribute to the sum over the multipole order λ [22]. Consequently, $P_{i \rightarrow f}$ is described by [21],

$$P_{i \rightarrow f} = \left(\frac{4\pi Z_p e}{\hbar} \right)^2 \frac{B(E\lambda, J_i \rightarrow J_f)}{(2\lambda+1)^3} \sum_{\mu=-\lambda}^{\lambda} \left(\int_{-\infty}^{\infty} \left[\left(\frac{1}{r_p}\right)^{\lambda+1} Y_{\lambda}^{\mu}(\theta_p, \phi_p) e^{i\omega t} \right] dt \right)^2. \quad (2.16)$$

The integral in equation 2.16 can be simplified by introducing the orbital integrals, $I_{\lambda, \mu}(\vartheta, \xi)$, adopted and tabulated by Alder [21] and observing that

the projectile trajectory lies in the plane spanned by (r_p, ϕ_p) so that $\theta_p = \frac{\pi}{2}$ and $\phi_p = 0$ in which case [21]

$$\int_{-\infty}^{\infty} \left[\left(\frac{1}{r_p} \right)^{\lambda+1} Y_{\lambda}^{\mu}(\theta_p, \phi_p) e^{i\omega t} \right] dt = \frac{1}{a^{\lambda} v_p} Y_{\lambda}^{\mu} \left(\frac{\pi}{2}, 0 \right) I_{\lambda, \mu}(\vartheta, \xi). \quad (2.17)$$

These integrals are obtained by parametrizing the hyperbolic trajectory of the projectile in the focal plane of the hyperbola [21] and depends on ϑ , the eccentricity of the projectile orbit, $\epsilon = \frac{1}{\sin \frac{\vartheta}{2}}$, a parameter w defined to be equal zero in a head collision and the adiabaticity parameter, ξ . The resulting expression for $I_{\lambda, \mu}(\vartheta, \xi)$ in terms of these parameters is given by [21],

$$I_{\lambda, \mu}(\vartheta, \xi) = \int_{-\infty}^{\infty} e^{i\xi(\epsilon \sinh w + w)} \frac{(\cosh w + \epsilon + i\sqrt{\epsilon^2 - 1} \sinh w)^{\mu}}{(\epsilon \cosh w + 1)^{\lambda + \mu}} dw. \quad (2.18)$$

The values of these integrals evaluated at various values of ϑ and ξ , as well their properties can be found in the tables of the classical orbital integrals in Coulomb excitation [24].

In addition to η , the adiabaticity parameter, ξ given by [7]

$$\xi = \frac{\tau_{col}}{\tau_{nuc}} = \frac{a}{v_p} \omega_{if}, \quad (2.19)$$

plays an important role in the semiclassical approximation of Coulomb excitation. In the above expression, $\tau_{col} = \frac{a}{v_p}$ is the collision time [7] and $\tau_{nuc} = \frac{\hbar}{\Delta E} = \frac{1}{\omega_{if}}$, is the lifetime of the excited level at an excitation energy, ΔE [7]. This parameter can be used in conjunction with ϵ to obtain the parameter, $\xi(\vartheta)$ given by

$$\xi(\vartheta) = \xi \epsilon = \frac{\xi}{\sin(\frac{\vartheta}{2})}, \quad (2.20)$$

which quantifies the degree to which the process is adiabatic [21], in which case $\xi(\vartheta) > 1$. When $\xi(\vartheta) < 1$, the approximation is sudden [21]. Furthermore, to ensure that the projectile trajectory does not deviate from the classical Rutherford trajectory, the following condition must also be satisfied,

$$\frac{\Delta E}{E_p} \ll 1, \quad (2.21)$$

where, E_p , is the incident energy of the projectile. The above condition must be introduced into the semiclassical approximation to ensure that the

resulting predictions are in agreement with quantum mechanics [7], [21]. To compensate for this, the symmetrization of the Coulomb excitation parameters, η and ξ have been found to satisfy equation 2.21, thereby bringing the predictions of the semiclassical approximation closer to the quantum mechanical predictions [21]. The symmetrization considers corrections to the energy loss of the recoiling ions for each final state due to inelastic scattering and the resultant modification of the trajectory by replacing v_p , with $v_{i,p}$ and $v_{f,p}$, in the expressions of a , η and ξ in the following manner,

$$a_{if} = \frac{Z_p Z_t e^2}{\mu v_{i,p} v_{f,p}}, \quad (2.22)$$

$$\eta_{if} = \frac{a_{if}}{\lambda}, \quad (2.23)$$

and

$$\xi_{if} = \frac{\mu}{\hbar} a_{if} (v_{f,p} - v_{i,p}), \quad (2.24)$$

where a_{if} , η_{if} and ξ_{if} denote the symmetrized values of a , η and ξ , respectively. From this point the parameters a , η and ξ will be replaced by their symmetrized analogues.

The expression for $P_{i \rightarrow f}$ obtained using first-order time-dependent perturbation theory, is then given by [23]

$$P_{i \rightarrow f} = \left(\frac{4\pi Z_p e}{\hbar} \right)^2 \frac{B(E\lambda, J_i \rightarrow J_f)}{(2\lambda + 1)^3} \sum_{\mu=-\lambda}^{\lambda} \left(|S_{E\lambda,\mu}(\vartheta, \xi)|^2 \right), \quad (2.25)$$

where [21]

$$S_{E\lambda,\mu}(\vartheta, \xi) = \frac{1}{a_{if}^\lambda \sqrt{v_{i,p} v_{f,p}}} Y_\lambda^\mu \left(\frac{\pi}{2}, 0 \right) I_{\lambda,\mu}(\vartheta, \xi_{if}). \quad (2.26)$$

The method is valid if $P_{i \rightarrow f}$ is much less than one. In order to characterize the validity of the perturbation approximation used to determine $P_{i \rightarrow f}$, an additional parameter, $\chi_{i \rightarrow f}^{(\lambda)}$, is used to describe the Coulomb excitation process [7]. This parameter is referred to as the strength parameter of the transition through, which the state $|i\rangle$ couples to the state $|f\rangle$ following the Coulomb excitation [7] of the projectile or the target and corresponds to the square root of $P_{i \rightarrow f}$ when the projectile scattering angle is π and the collision is of sudden impact [23], that is,

$$\chi_{i \rightarrow f}^{(\lambda)} = \pm \sqrt{P_{i \rightarrow f}(\vartheta = \pi, \xi_{if} = 0)} \quad (2.27)$$

where $\chi_{i \rightarrow f}^{(\lambda)}$ takes on the same sign as $\langle J_i | \hat{M}(E\lambda) | J_f \rangle$ of the nucleus undergoing Coulomb excitation. The explicit expression for $\chi_{i \rightarrow f}^{(\lambda)}$ depends on whether the beam or the target nucleus is excited. The symmetrized $\chi_{i \rightarrow f}^{(\lambda)}$ for an $E\lambda$ transition in the target is given by [7],

$$\chi_{i \rightarrow f}^{(\lambda)} = 4\sqrt{\pi} \frac{(\lambda + 1)!}{(2\lambda + 1)!!} \frac{Z_t e}{\hbar \sqrt{v_{i,p} v_{f,p}}} \frac{\langle J_i | \hat{M}(E\lambda) | J_f \rangle}{a_{if}^\lambda \sqrt{2J_i + 1}}. \quad (2.28)$$

For projectile excitation, the symmetrized $\chi_{i \rightarrow f}^{(\lambda)}$ for an $E\lambda$ transition is given by [7]

$$\chi_{i \rightarrow f}^{(\lambda)} = 4\sqrt{\pi} \frac{(\lambda + 1)!}{(2\lambda + 1)!!} \frac{Z_p e}{\hbar \sqrt{v_{i,p} v_{f,p}}} \frac{\langle J_i | \hat{M}(E\lambda) | J_f \rangle}{a_{if}^\lambda \sqrt{2J_i + 1}}. \quad (2.29)$$

Consequently, the expression for $P_{i \rightarrow f}$ given in equation 2.16 can be expressed as the product of $\chi_{i \rightarrow f}^{(\lambda)}$ and a function $K_{\lambda,\mu}(\vartheta, \xi_{if})$ in the following manner [7],

$$P_{i \rightarrow f} = \frac{1}{2\lambda + 1} \sum_{\mu=-\lambda}^{\lambda} \left[\chi_{i \rightarrow f}^{(\lambda)}(\vartheta, \xi_{if}) K_{\lambda,\mu}(\vartheta, \xi_{if}) \right]^2, \quad (2.30)$$

where $K_{\lambda,\mu}(\vartheta, \xi_{if})$ contains the dependence of $P_{i \rightarrow f}$ on the classical orbit of the projectile which can be written in terms of $S_{E\lambda,\mu}(\vartheta, \xi_{if})$ as follows [7],

$$K_{\lambda,\mu}(\vartheta, \xi_{if}) = \sqrt{v_{i,p} v_{f,p}} a_{if}^\lambda \sqrt{\pi} \frac{(2\lambda - 1)!!}{(\lambda - 1)!} |S_{E\lambda,\mu}(\vartheta, \xi_{if})|. \quad (2.31)$$

The validity of the perturbation approximation as well as its dependence on the values of the parameters ξ_{if} , $\chi_{i \rightarrow f}^{(\lambda)}$ and the multipole order λ within the semiclassical approximation, have been found to be valid for $\chi_{i \rightarrow f}^{(\lambda)} \ll 1$ [7], when the value of the parameter ξ_{if} is arbitrary and for multiple orders λ ranging from one to four [7]. In this case, the differential cross section for Coulomb excitation, $d\sigma_C$ is proportional to the product of $P_{i \rightarrow f}$ and $d\sigma_R$,

$$\left(\frac{d\sigma_C}{d\Omega} \right)_{i \rightarrow f} = P_{i \rightarrow f} \frac{d\sigma_R}{d\Omega} \quad (2.32)$$

When $\chi_{i \rightarrow f}^{(\lambda)} \ll 1$ and $\xi_{if} < 1$, the time-dependent transition amplitudes can be obtained using higher order time-dependent perturbation theory [7]. For the sudden approximation, or the case where $\chi_{i \rightarrow f}^{(\lambda)} \gg 1$, the perturbation approximations are no longer valid and the time-dependent transition amplitudes have to be found by solving a coupled system of differential equations [[7], [21], [23]]. In this case, the states of interest may be populated indirectly

through multiple excitation and the expressions for the Coulomb excitation probability can be found using the theory of multiple Coulomb excitation, within the semiclassical approximation [[7], [21]].

To second order, the excitation process can be viewed as a two step process in which the projectile is excited from $|i\rangle$ to an intermediate state $|k\rangle$, from which it undergoes a transition to the final state $|f\rangle$. The Coulomb excitation probability will therefore depend on the transition amplitudes between $|i\rangle$ and $|f\rangle$, as well as the transition amplitudes between both $|i\rangle$ and $|k\rangle$ and $|k\rangle$ and $|f\rangle$. In addition, the second-order Coulomb excitation probability will also depend on the static features of the final state $|f\rangle$ [7]. Figure 2.2 shows a schematic of the RE, in which the nucleus, undergoing the excitation process is excited from the 0^+ ground state through E2 radiation to the 2^+ state. The probability for the Coulomb excitation of the 2^+ state is proportional to the reduced transition probability for an electric transition of multipole order 2 (fig 2.2 (a)). Figure 2.2 (b) shows the reorientation effect for the 2^+ state, which causes the splitting of the magnetic substates. In this case the probability for the Coulomb excitation is proportional, in second order, to $Q_S(2^+)$.

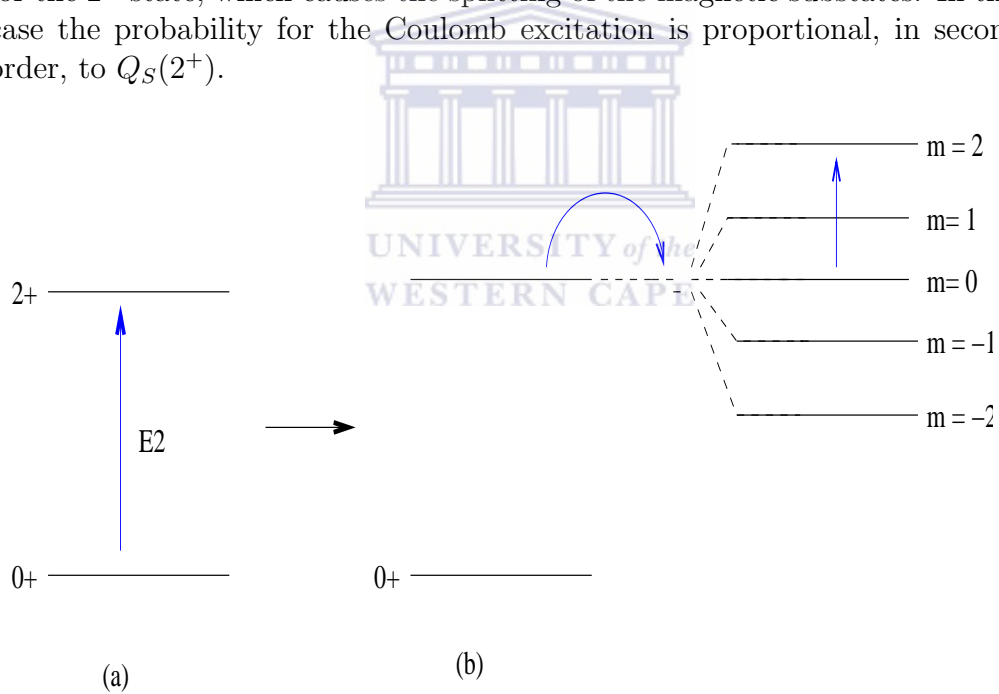


Figure 2.2: The reorientation effect.

The RE is of particular interest in this work. Here, the Coulomb excitation probability depends on both the transition amplitudes between the final and

the initial state, as well as the spectroscopic quadrupole moment of the final state [7]. The expressions for $P_{i \rightarrow f}$ for an excitation $0_1^+ \rightarrow 2_1^+$, obtained using second-order time-dependent perturbation theory can be calculated under the assumption that no other 2^+ state is in the vicinity of the first 2^+ state. The Coulomb excitation probability to second order, $P_{i \rightarrow f}^{(2)}$, can be expressed as the sum of two terms in the following manner

$$P_{i \rightarrow f}^{(2)} = P_{i \rightarrow f}^{(11)} + P_{i \rightarrow f}^{(12)}, \quad (2.33)$$

where $P_{i \rightarrow f}^{(11)}$, is the first order contribution to $P_{i \rightarrow f}^{(2)}$, given by

$$P_{i \rightarrow f}^{(11)} = \frac{1}{5} \left[\chi_{i \rightarrow f}^{(2)} \right]^2 \sum_{\mu=-2}^2 \left[K_{2,\mu}(\vartheta, \xi_{if}) \right]^2, \quad (2.34)$$

where

$$K_{2,\mu}(\vartheta, \xi_{if}) = Y_{2\mu}\left(\frac{\pi}{2}, 0\right) I_{2,\mu}(\vartheta, \xi_{if}), \quad (2.35)$$

and $P_{i \rightarrow f}^{(12)}$ is given by,

$$P_{i \rightarrow f}^{(12)} = \frac{27\pi^{\frac{3}{2}}}{\sqrt{5}} \chi_{f \rightarrow f}^{(2)} \left[\chi_{i \rightarrow f}^{(2)} \right]^2 \sum_{\mu=-2}^2 \left[K_{2,\mu}(\vartheta, \xi_{if}) \right]^2 B_{2\mu}^{(22)}(\xi_{if}, 0, \vartheta). \quad (2.36)$$

The terms $\frac{1}{5} \sum_{\mu=-2}^2 \left[K_{2,\mu}(\vartheta, \xi_{if}) \right]^2$ and $\frac{1}{\sqrt{5}} \sum_{\mu=-2}^2 \left[K_{2,\mu}(\vartheta, \xi_{if}) \right]^2 B_{2\mu}^{(22)}(\xi_{if}, 0, \vartheta)$ can be obtained from the tables of the classical orbital integrals in Coulomb excitation [24], and represent the dependence of $P_{i \rightarrow f}^{(12)}$ on the trajectory of the projectile, while the term $\chi_{f \rightarrow f}^{(2)}$, is given by [7]

$$\chi_{f \rightarrow f}^{(2)} = \frac{1}{3} \sqrt{\frac{7}{10}} \frac{Z_p e^2}{\hbar v_p} \frac{Q_S(2_1^+)}{a_{if}}, \quad (2.37)$$

where $Q_S(2_1^+)$ is for the projectile nucleus. The RE can therefore be used to determine $Q_S(2_1^+)$ directly from the Coulomb excitation probability, $P_{i \rightarrow f}^{(2)}$. The symmetrized differential cross section for the Coulomb excitation process, to second order, can be obtained by using the expression for $P_{i \rightarrow f}^{(2)}$ in conjunction with the symmetrized Rutherford differential cross section, as follows

$$\left(\frac{d\sigma_C}{d\Omega} \right)_{i \rightarrow f} = P_{i \rightarrow f}^{(2)} \frac{d\sigma_R}{d\Omega}. \quad (2.38)$$

In practice, the RE is usually quantified by the coefficient, r_{eff} , through an expression, which involves the ratio of the Coulomb excitation probabilities

$P_{i \rightarrow f}^{(11)}$ and $P_{i \rightarrow f}^{(12)}$ as opposed to the cross sections, and is given by [7],

$$r_{eff} = \frac{P_{i \rightarrow f}^{(12)}}{P_{i \rightarrow f}^{(11)}}. \quad (2.39)$$

By using equation 2.38 in conjunction with the expression of $\chi_{f \rightarrow f}^{(\lambda)}$ for projectile excitation, in equation 2.28, the RE coefficient for projectile excitation, r_{eff}^p can be expressed as [7],

$$r_{eff}^p = \frac{m_p \Delta E}{Z_p (1 + \frac{m_p}{m_t})} \langle 2_1^+ | \hat{M}(E\lambda) | 2_1^+ \rangle K(\vartheta, \xi_{if}), \quad (2.40)$$

where $K(\vartheta, \xi_{if})$ in equation 2.41 given by,

$$K(\vartheta, \xi_{if}) = 1.135 \frac{\sum_{\mu=-2}^2 [K_{2,\mu}(\vartheta, \xi_{if})]^2 B_{2\mu}^{(22)}(\xi_{if}, 0, \vartheta)}{\xi_{if} \sum_{\mu=-2}^2 [K_{2,\mu}(\vartheta, \xi_{if})]^2}, \quad (2.41)$$

and can be obtained from tables [7]. In the case of target excitation, r_{eff}^t is given by [7]

$$r_{eff}^t = \frac{m_p \Delta E}{Z_t (1 + \frac{m_p}{m_t})} \langle 2_1^+ | \hat{M}(E\lambda) | 2_1^+ \rangle K(\vartheta, \xi_{if}). \quad (2.42)$$

Depending on the type of excitation (projectile or target), equations 2.41 or 2.42 can be used to express $P_{i \rightarrow f}^{(2)}$ as,

$$P_{i \rightarrow f}^{(2)} = P_{i \rightarrow f}^{(11)} (1 + r_{eff}). \quad (2.43)$$

By using equation 2.43 in conjunction with equations 2.28 and 2.29, the relation between the symmetrized $d\sigma_C$ and r_{eff} , can be obtained by substituting equation 2.43 into equation 2.31 hence,

$$\left(\frac{d\sigma_C}{d\Omega} \right)_{i \rightarrow f} = P_{i \rightarrow f}^{(11)} (1 + r_{eff}) \frac{d\sigma_R}{d\Omega}. \quad (2.44)$$

This section explored the theoretical framework of Coulomb excitation within the semiclassical approximation that is relevant to the work that will be discussed in the chapters that follow. In particular it was found that three parameters, namely the Sommerfeld parameter, η , the adiabaticity parameter ξ

and the strength parameter, $\chi_{i \rightarrow f}^{(\lambda)}$ can be used to describe the validity of the semiclassical approximation. Furthermore, the expressions for the Coulomb excitation probabilities to first and second-order were presented. In the case of the first-order Coulomb excitation probability, the Coulomb excitation cross section was found to be proportional to $B(E\lambda)$, while the Coulomb excitation cross section obtained using second-order time-dependent perturbation theory was found to be proportional to the values of $B(E\lambda)$ and $Q_S(2_1^+)$, which was described in terms of the RE. The expressions for the RE coefficients for projectile, r_{eff}^p , and target, r_{eff}^t , excitation were presented. Based on these explicit expressions, it was found that the RE and, hence, the value of $Q_S(2_1^+)$, is enhanced for projectile excitation. In addition, it was found that the RE can be enhanced by choosing the scattering angles, the safe beam energy and the value of $Q_S(2_1^+)$ appropriately, so that the choice of these parameters maximize the value of r_{eff} .

2.3 *Gosia* simulations

The Coulomb excitation cross sections were simulated using the semiclassical coupled channel least squares code *Gosia* [27]. This code takes inputs, such as the experimental γ -ray intensities, lifetimes, matrix elements, stopping powers and the geometry of the experimental setup. Using these input, the code performs a least squares minimization of a χ^2 function that is based on the input data and the calculated γ -ray intensities, to generate a set of matrix elements that have been optimized to replicate the experimental data, which can be used to determine matrix. The details of the *Gosia* simulations performed in this work will be presented next.

2.3.1 Coupled channel method

Gosia assumes that the nucleus is initially in its ground state, $|i\rangle = |\Phi_i\rangle$, at some time, $t = -\infty$. Then it undergoes Coulomb excitation to an final state, $|f\rangle = |\Phi_f\rangle$. The final state can be expressed in terms the transition amplitudes $c_f(t = \infty)$. The system of coupled differential equations for the transition amplitudes is obtained according to equation 2.8, where $V(t) = V_{p,t}(t)$ denotes the time-dependent monopole-multipole interaction potential, so that the charge of the unexcited nucleus (projectile or target)

interacts with appropriate multipole moment of the excited nucleus (target or projectile) [27]. Equation 2.8 is then expressed according to the type of excitation. For electric excitation [27],

$$\frac{dc_f(t)}{dt} = q_{1,2}^i(t) \left[\sum_{\lambda,\mu} \zeta_{\lambda,\mu} S_{\lambda,\mu}^E \langle i | \hat{M}(E\lambda, -\mu) | f \rangle \right], \quad (2.45)$$

where $Z_{p,t}$ denotes the charge number of the unexcited nucleus and $\hat{M}(E\lambda, \mu)$ is given by equation 2.13. For magnetic excitation equation, 2.8 is given by [27]

$$\frac{dc_f(t)}{dt} = q_{1,2}^i(t) \left[\sum_{\lambda,\mu} \frac{\zeta_{\lambda,\mu}}{\lambda c} \vec{r}(t) \cdot (\vec{r} \times \vec{\nabla}) S_{\lambda,\mu}^E \langle i | \hat{M}(M\lambda, -\mu) | f \rangle \right] \quad (2.46)$$

where $\zeta_{\lambda,\mu} = \frac{(-1)^\mu}{2\lambda+1}$,

$$q_{1,2}^i(t) = \frac{4\pi Z_{1,2}e}{i\hbar} \sum_i c_i(t) e^{i\omega_{if}t}, \quad (2.47)$$

$S_{\lambda,\mu}^E$ is given by,

$$S_{\lambda,\mu}^E = \frac{Y_{\lambda,\mu}(\theta(t), \phi(t))}{[r(t)]^{\lambda+1}}, \quad (2.48)$$

and [27]

$$\hat{M}(M\lambda, \mu) = \int r^\lambda \vec{j}(\vec{r}) (\vec{r} \times \vec{\nabla}) Y_\lambda^\mu(\theta, \phi) d\tau. \quad (2.49)$$

Here, $\vec{j}(\vec{r})$ is the nuclear current density and the integration is carried out in the frame in which the nucleus undergoing the excitation is at rest [27]. The above expressions are transformed into a coordinate system which simplifies the evaluation of the Coulomb excitation amplitudes. The resulting expression for $\frac{dc_f(t)}{dt}$ is then used in conjunction with numerical values of the constants involved in the above expressions to obtain iterative forms of equations 2.46 and 2.47 that are used to approximate the solutions to $\frac{dc_f(t)}{dt}$ using various numerical methods [27]. The resulting solutions are then used to determine the level populations and γ -ray yields resulting from the Coulomb excitation process.

2.3.2 Calculation of γ -ray intensities

The excited states populated in the Coulomb excitation, de-excite via electron conversion, or, the emission of γ radiation [7]. The latter depends

on the direction of polarization through an angular distribution, as well as the direction of the projectile particle through an angular correlation. The measured γ -ray intensities will therefore depend on the angular distribution through the differential cross section of the γ decay for a $J_i \rightarrow J_f$ transition $\frac{d^2\sigma(J_i \rightarrow J_f)}{d\Omega_p d\Omega_\gamma}$, where $d\Omega_p$ and $d\Omega_\gamma$ denote the solid angles of particle and γ -ray detection, respectively. The *Gosia* code computes $\frac{d^2\sigma(J_i \rightarrow J_f)}{d\Omega_p d\Omega_\gamma}$ by constructing a set of irreducible tensor operators, $\rho_{k,\chi}(J, J)$, known as statistical tensors [27] to express the wave functions of the excited state in terms of the state of polarization of the excited level [27]. The resulting expression obtained by taking the average of these $\rho_{k,\chi}(J, J)$, over all of the possible polarizations of the unpolarized ground state is given by [27]

$$\rho_{k,\chi}(J, J) = \kappa(J, J_0) \sum_{M_0, M, M'} \frac{(-1)^{J-M-k}}{\sqrt{2J+1}} Z(J, M, M', M_0, K, \chi), \quad (2.50)$$

where $\kappa(J, J_0) = \frac{\sqrt{2J+1}}{2J_0+1}$ and $Z(J, M, M', M_0, k, \chi) = \langle J, k, -M', \chi | J, k, J - M \rangle a_{JM'}^*(M_0) a_{JM}(M_0)$, M_0 denotes the magnetic substate belonging to the ground state J_0 , χ denotes the index of the polarization [27]. The value of $\frac{d^2\sigma(J_i \rightarrow J_f)}{d\Omega_p d\Omega_\gamma}$ is then computed by transforming to the coordinate frame in which the statistical tensors are computed to the laboratory frame, where the origin is at the position of the target and the z-axis is directed along the beam axis so that [27],

$$\frac{d^2\sigma(J_i \rightarrow J_f)}{d\Omega_p d\Omega_\gamma} = \frac{d\sigma_R}{d\Omega_p} \sum_{k\chi} \frac{G_k \rho_{k,\chi}}{2\gamma(J)\sqrt{\pi}} \sum_{\lambda\lambda'} \left[\delta_\lambda \delta_{\lambda'}^* F_k(\lambda\lambda', JJ_f) Y_{k,\chi}(\vartheta_\gamma, \phi_\gamma) \right], \quad (2.51)$$

where the γ -ray emission probability, which is related to the $J_i \rightarrow J_n$ transition amplitudes, $\delta(J_i \rightarrow J_n)$, with multipolarity λ , $\gamma(J)$ is given by [27]

$$\gamma(J) = \sum_{\lambda,n} |\delta(J_i \rightarrow J_n)|^2, \quad (2.52)$$

with,

$$\delta(J_i \rightarrow J_n) = \frac{i^{n(\lambda)}}{(2\lambda+1)!! \hbar^{\lambda+1}} \left(\sqrt{\frac{8\pi(\lambda+1)E_\gamma}{c\lambda}} \right) \left(\frac{E_\gamma}{c} \right)^\lambda \frac{\langle J_n || E(M)\lambda || J \rangle}{\sqrt{2J+1}}, \quad (2.53)$$

where E_γ denotes the γ -ray energy, and $n(\lambda) = \lambda$ for a electric transition of the multipole order λ , or $n(\lambda) = \lambda + 1$ in the case of a magnetic transition of multipole order λ [27]. $F_k(\lambda\lambda', JJ_f)$ denotes the γ - γ correlation coefficients

[27] and G_k denotes a correction coefficient [27]. The expression for $\frac{d^2\sigma(J_i \rightarrow J_f)}{d\Omega_p d\Omega_\gamma}$ assumes that the detector, is a point detector, whose detection efficiency $\epsilon_\gamma \approx 1$. The detector material, geometry, E_γ and absorbers are incorporated into the computation of $\frac{d^2\sigma(J_i \rightarrow J_f)}{d\Omega_p d\Omega_\gamma}$ by introducing a set of attenuation coefficients [27]. These attenuation coefficients, $Q_k(E_\gamma)$ are given by [27],

$$Q_k(E_\gamma) = \frac{C_2 Q_k(E_0) + C_1 Q_k(E_\gamma - E_0)^2}{C_2 + (E_\gamma - E_0)^2}, \quad (2.54)$$

where C_1 and C_2 are fitting parameters, while the coefficient, E_0 , depend on the material of the absorbers. For the $^{194}\text{Pt}(^{20}\text{Ne}, ^{20}\text{Ne}^*)^{194}\text{Pt}^*$ experiment, $E_0 = 50$ keV was used since no absorbers were utilized [27]. The γ -ray intensities, $Y(J_i \rightarrow J_f, \vartheta_p, E_p)$, are then computed by using equations 2.50 to 2.54 together with the user input. By transforming the result of integrating $\frac{d^2\sigma(J_i \rightarrow J_f)}{d\Omega_p d\Omega_\gamma}$ with respect $d\Omega_p$ to the laboratory frame and integrating the result with respect to the target thickness, the total integrated γ -ray yield, $Y(J_i \rightarrow J_f)$ can then be expressed as [27],

$$Y(J_i \rightarrow J_f) = \int_{E_p^{lab, min}}^{E_p^{lab, max}} \frac{Y(J_i \rightarrow J_f, E_p^{lab})}{\frac{dE}{dx}} dE_p^{lab}. \quad (2.55)$$

2.3.3 Count rate calculations

In this work *Gosia* was used to simulate the γ -ray integrated yields for various scattering angular ranges. The resulting γ -ray yields for each γ -ray detector was extracted from the output file for each γ -ray detector corresponding to a particular angular range of the particle detector. The absolute particle- γ -ray coincidence count rates expected from experiment were calculated using the equation

$$N_m = \frac{I_p N_A \epsilon}{10^{30} A_p} Y(J \rightarrow J_f)_m \Delta, \quad (2.56)$$

where $N_A = 6.023 \times 10^{23}$ atoms·mol⁻¹, I_p , denotes the beam current, m denotes the γ -ray detector number, ranging from one to nine, and ϵ denotes product of the efficiencies of the particle, ϵ_p and ϵ_γ .

The beam current to be used prior to the experiments, was chosen to prevent damage to the particle detector. For heavy ions, silicon detectors can take 10^9 ions·cm⁻², before damage becomes apparent in the particle spectra (e.g., loses on particle energy, which can be seen in the elastic peaks moving to lower energies, and by an elastic peak that is observed as two peaks, as

opposed to a single peak). The calculations involved in estimating the total damage, consisted of calculating the minimum and average angular coverage for each ring of the S3 detector, at a fixed distance from the target, and using the geometric specifications given in appendix C.

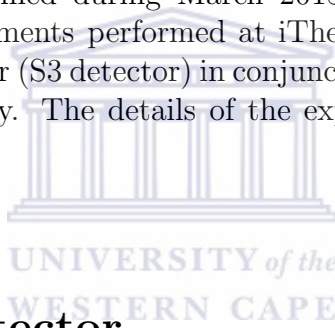
The calculated angles were then used to perform kinematics, energy loss, Rutherford cross sections and Coulomb excitation cross sections calculations for the average angular range. The results of these calculations were then used to compute the counts expected per hour using according to equation 2.56. The results of these calculations were then compared with a *Geant4* simulation of the S3 detector [30].



Chapter 3

Experimental details

Two Coulomb excitation experiments were performed at iThemba LABS during this work: 1) the $^{194}\text{Pt}(^{20}\text{Ne}, ^{20}\text{Ne}^*)^{194}\text{Pt}^*$ Coulomb excitation carried out over the course of two weekends in 2013; and 2) the $^{208}\text{Pb}(^{40}\text{Ar}, ^{40}\text{Ar}^*)^{208}\text{Pb}^*$ Coulomb excitation performed during March 2015. These were the first Coulomb excitation experiments performed at iThemba LABS using an S3 double-sided silicon detector (S3 detector) in conjunction with the AFRODITE HPGe clover detector array. The details of the experimental setup is presented in this chapter.



3.1 The S3 Detector

The detection of $^{20}\text{Ne}^{3+}$ ions was carried out using an S3 detector, which was originally designed for Coulomb excitation studies involving radioactive ion beams [34] by Micron Semiconductors in the UK. This detector is a segmented silicon strip detector based on ion implantation technology and composed of 24 rings on the junction side and 32 sectors on the ohmic side which are electrically separated from one another.

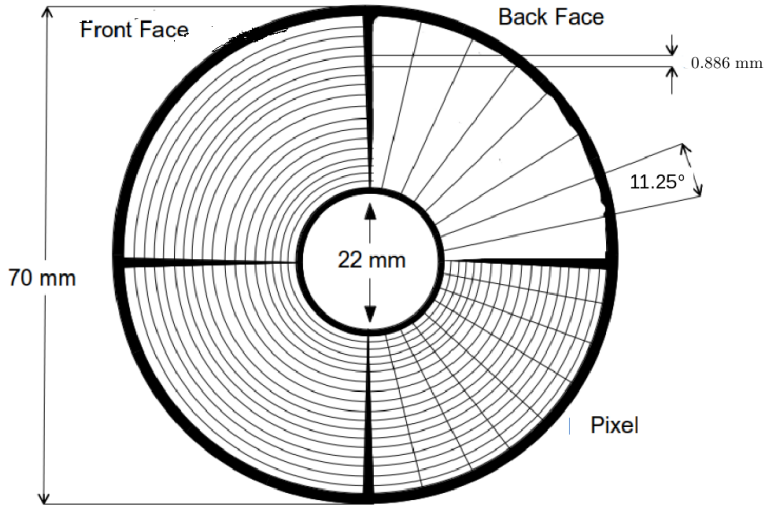


Figure 3.1: Schematic of the S3 double-sided silicon detector.

Figure 3.1 shows a schematic of the S3 detector utilized in this work. The top left region shows the 24 rings of the S3 detector. Each ring has a width of $886 \mu\text{m}$. The bottom right region shows the quasi pixels formed when the 24 rings are superimposed on the 32 sectors. The top right region shows the back face of the S3 detector consisting of 32 sector strips. Each of the individual sectors possess a width of 11.25° , while the inner and outer active diameters of the S3 detector are 22 mm and 70 mm respectively.

3.2 HPGe clover detectors

The HPGe clover detector (clover detector) was initially developed by Eurisys Measures [35] to improve the detection characteristics of composite Ge detectors. The clover detector consists of four Germanium crystals of type n, in which the geometric configuration when viewed from the front is similar to that of a four leaf clover, as shown in figure 3.2

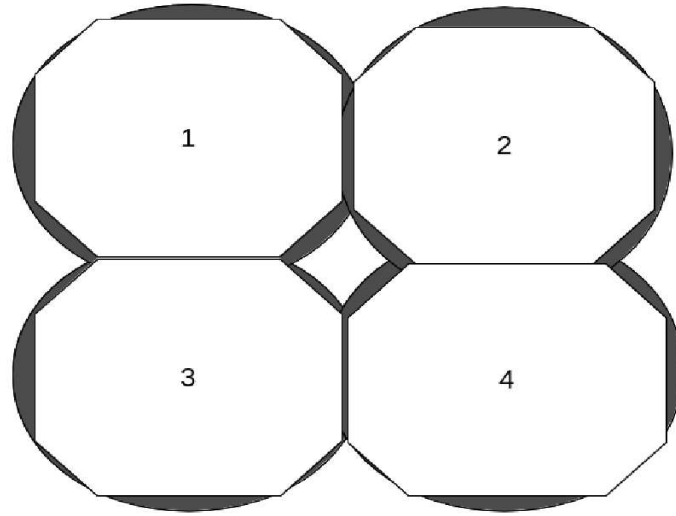


Figure 3.2: Schematic of the front face of an HPGe clover detector.

In order to achieve an active volume that is as close to the original crystal volume, each Ge crystal is grown separately so that a distance of 0.2 mm between two of the Ge crystals can be achieved. Each crystal within the detector has a diameter of 50 mm and a length of 70 mm [39]. The Ge crystals share a common cryostat in which each individual crystal is joined to a grip that is attached to the rear side of each Ge crystal [39]. A capacitance coupling is used to acquire signals from each of the four crystals, whose inner contacts are connected up to a common high ground voltage [39].

3.2.1 Modes of operation

The clover detector offers two modes of detection. The first mode is known as the coincidence mode. This mode may be triggered when multiple γ -rays are detected instantaneously in two or more of the Ge crystals. The second mode is the direct (singles) mode of detection, where each of the individual Ge crystals is used as a single Ge detector. The use of n-type Ge crystals offers the advantage of reduced neutron damage [39], while the use of multiple crystals allow for the option of using the detector as a Compton polarimeter [36]. In addition, the use of four n-type coaxial Ge crystals offers the possibility for Doppler correction.

3.3 The AFRODITE array

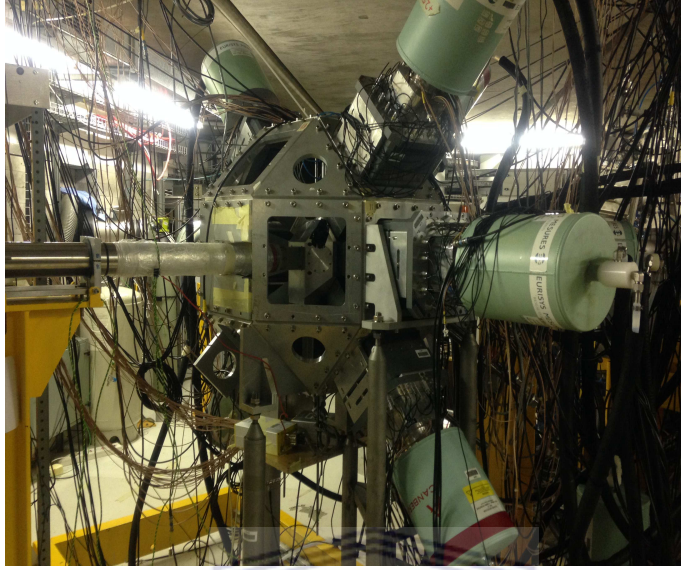


Figure 3.3: The AFRODITE HPGe clover detector array.

The African Omni-purpose Detector for Innovative Techniques and Experiments (AFRODITE) is the clover detector array that was used to detect the de-excited γ -rays during the Coulomb excitation experiments performed at iThemba LABS. The configuration of the AFRODITE array consisted of nine detectors arranged in a rhomboidal octahedral configuration, as shown in figure 3.3. Six of the nine clover detectors were positioned at 90° with respect to the beam axis, while the remaining three clover detectors were positioned at 135° with respect to the beam axis. The distance between the target and the clover detectors was 196 mm.

3.4 Electronics

A new target chamber manufactured at iThemba LABS was used to house the target ladder which held an enriched ^{194}Pt target having a thickness of $1.2 \text{ mg}\cdot\text{cm}^2$, together with the S3 detector that was connected to a Yamaichi 64-way R/A connector.

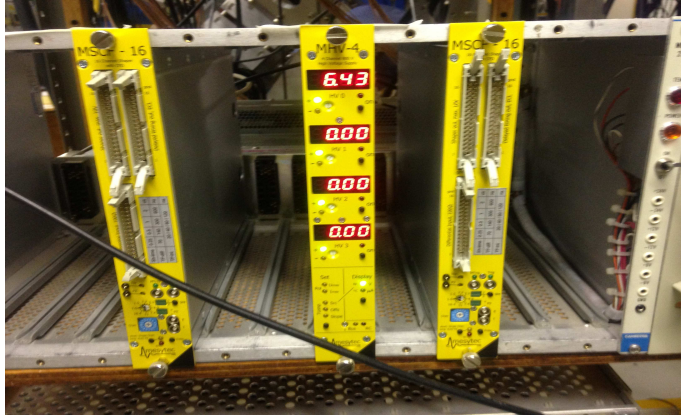


Figure 3.4: MHV-4 bias unit used during the measurements.

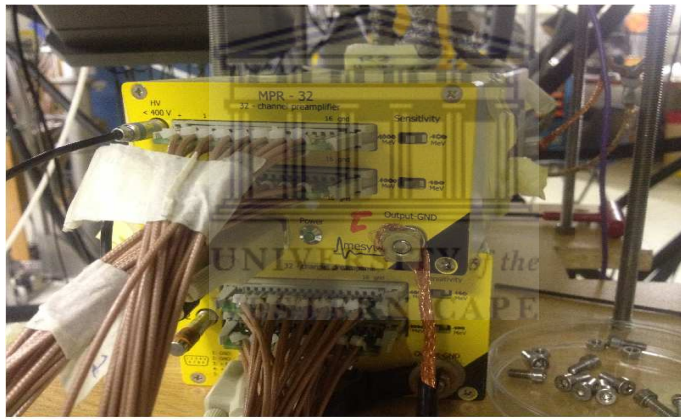


Figure 3.5: MPR-32 multichannel preamplifiers and S1, S2, R1 and R2 cables.

BLOCK DIAGRAM- S3 CD Detector Setup

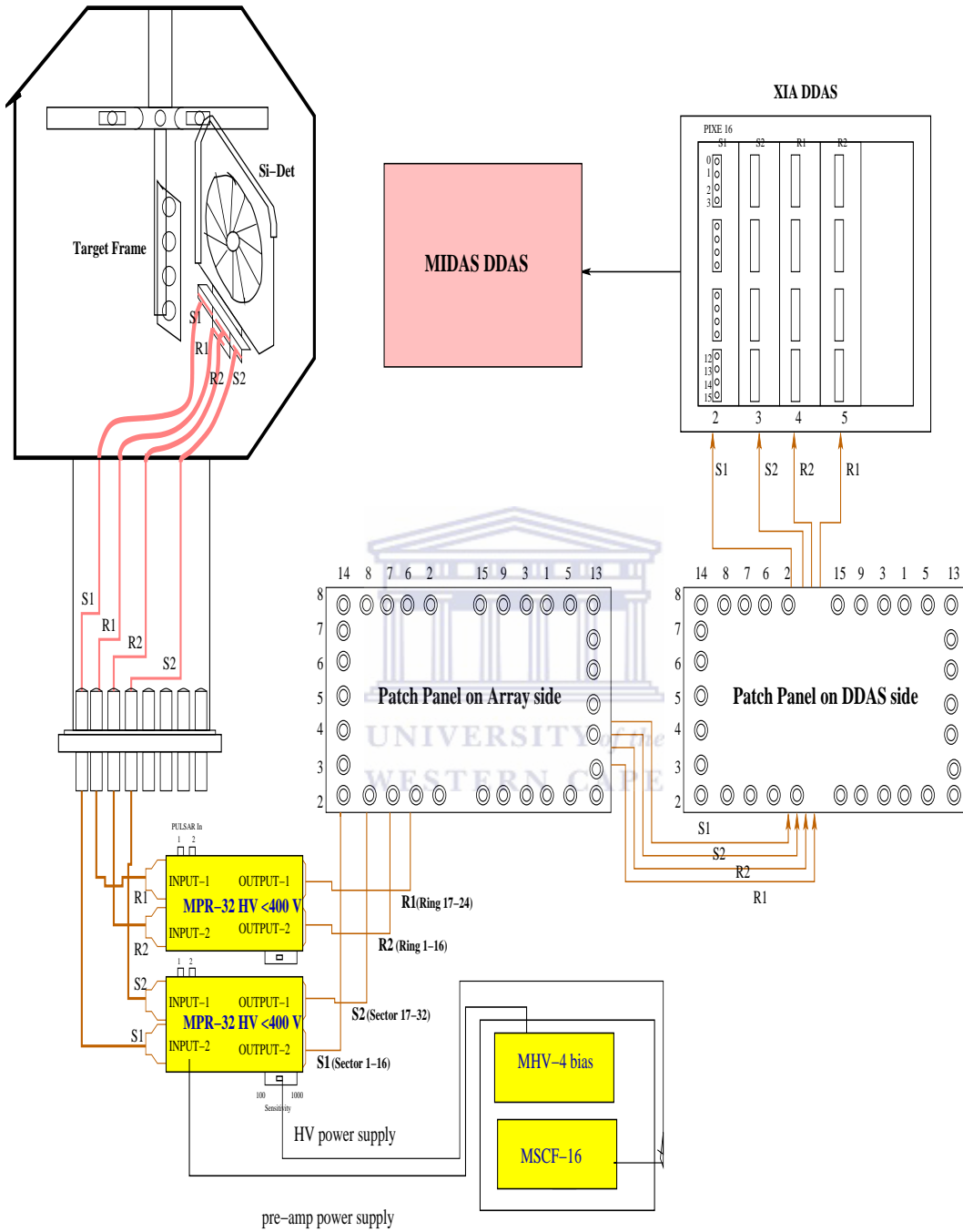


Figure 3.6: Schematic of electronics setup used for the Coulomb excitation measurements.

The signals from the 24 rings and 32 sectors were transported using four Mesytec mesh-shielded vacuum cables S1, S2, R1 and R2. These cables were connected to a PCB board. The S1 and S2 cables were used for the sector signals, where each of these cables can accommodate 16 signals, whereas the R1 and R2 cables were used for the rings. The mapping of the rings and sectors to the cables can be found in the appendix C. The S1, S2, R1 and R2 signals were input to the two Mesytec MPR-32 multichannel preamplifiers that were connected to a Mesytec 4-channel MHV-4 bias unit [46].

The MHV-4 (figure 3.4) is a high precision bias supply unit used to bias the S3 detector and monitor the leakage current during the Coulomb excitation measurements. The MHV-4 bias unit comes together with a front end user interface that can be used to adjust the voltages from zero to a maximum of 400 V [46]. The MHV-4 bias unit was used to bias the Mesytec MPR-32 multichannel preamplifiers. The MPR-32 multichannel preamplifiers [45] (figure 3.5) can be used with positive and negative polarities and is commercially available in several gain ranges. The range used for the ^{20}Ne and ^{40}Ar experiments were 20-100 MeV and 100-1000 MeV, respectively. The S1, S2, R1 and R2 cables were output from the MPR-32 multichannel preamplifiers to patch panels which were sent to the XIA modules connected to the digital data acquisition system.

3.5 Digital data acquisition system

The digital data acquisition system (DDAS) used in the present work is a XIA based digital system which consists of two PXI crates. These PXI crates are capable of housing multiple 16-channel Pixie-16, 100 MHz digital gamma finder cards. Data consisting of 48-bit time-stamps, baseline information together with the energy signals are extracted from events registered in the detectors [43]. These data are then read out using a simple polled method on a per card basis and transferred over an ethernet connection to a collection unit where the data are filtered and marked by processors referred to as "collectors". These collectors check and correct the time-ordering of each card associated with an active crate [43]. The data from the collectors is then sent to a data merging unit, where it undergoes the time ordering process using methods similar to that of the Total Data Readout method [44] to generate a single time ordered stream of data [43].

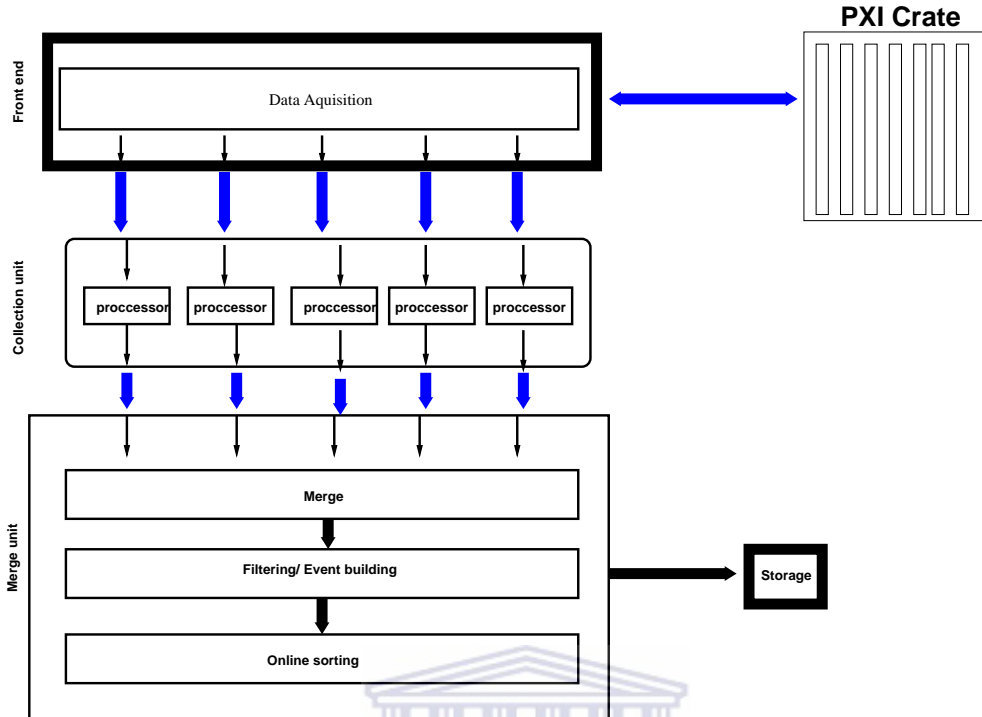


Figure 3.7: Schematic of the DDAS.

The time ordered data is sent from the data merge unit to the event builder, where the data undergoes further filtering before the events are built and written to the run files. The latter are stored on a separate server computer running the multi-instance data acquisition software, *MIDAS* [37] and *MTsort* [38], which is used to control the running and sorting of the data acquisition process.

The cabling of the S3 detector shown in figure 3.6 was used in conjunction with the default cabling of the AFRODITE array to send the signals to a patch panel connected to the DDAS modules. The look-up table for the mapping of the detector to the DDAS modules and XIA module used in the experiments can be found in appendix C. A ^{226}Ra α source was used to select the energy risetime, the energy flat top and peak separation parameters that reproduced the best peak shape and energy resolution. A schematic of the DDAS is shown in figure 3.7, where the black arrows indicate the direction in which the internal data flows and the blue arrows indicate the Ethernet communication [43].

3.6 Preliminary experimental considerations

The calculations of the parameters required for a safe Coulomb excitation measurement are presented here.

3.6.1 Maximum safe bombarding energy criteria

One of the most important considerations in Coulomb excitation measurements concerns the minimum distance of closest approach between the projectile and target, d_{min} , which is given by

$$d_{min} \geq 1.25(A_p^{\frac{1}{3}} + A_t^{\frac{1}{3}}) + s(\vartheta) \quad (3.1)$$

where $s(\vartheta)$ denotes the separation between the nuclear surfaces (projectile and target), in the center of mass frame. The angular range for particle detection can be deduced for equation 3.1 to be satisfied. An empirical expression for $s(\vartheta)$, as a function of ϵ , A_p , A_t and the incident beam energy, E_{lab} , given by [2], [41]

$$s(\vartheta) = \frac{Z_p Z_t e^2}{E_{lab}} \left(1 + \frac{A_p}{A_t}\right) (1 + \epsilon) - 1.25(A_p^{\frac{1}{3}} + A_t^{\frac{1}{3}}). \quad (3.2)$$

Values for $s(\vartheta)$ have been determined from a series of experiments investigating the effect of Coulomb-nuclear interference effect. These experiments considered the maximum bombarding energies at which the contributions of nuclear excitation remain negligible [41]. In addition, experiments aimed at determining $Q_S(2_1^+)$ for nuclei in the sd shell via the RE demonstrated that discrepancies were found for values of $s(\vartheta) < 5.9$ fm [2], while the measurements of $Q_S(2_1^+)$ in ^{18}O and other sd shell nuclei, carried out by Kean and collaborators showed that values of $s(\vartheta) > 6.5$ fm [[2], [41]] gave consistent values. Only one out of the three RE measurements aimed at determining the $Q_S(2_1^+)$ in ^{20}Ne [2], satisfied the safe criteria prescribed by Spear [2],

$$d_{min} \geq 1.25(A_p^{\frac{1}{3}} + A_t^{\frac{1}{3}}) + 6.5 \text{ fm}. \quad (3.3)$$

The maximum safe beam energy involving light nuclei should realize the above criteria [2]. Cline prescribed 5 fm for $s(\vartheta)$ when heavy ions are involved [20]. Plots of $s(\vartheta)$, as a function of average ϑ for the $^{194}\text{Pt}(^{20}\text{Ne}, ^{20}\text{Ne}^*)^{194}\text{Pt}^*$ reaction at 73 (left) and 96 (right) MeV, are shown in figure 3.8.

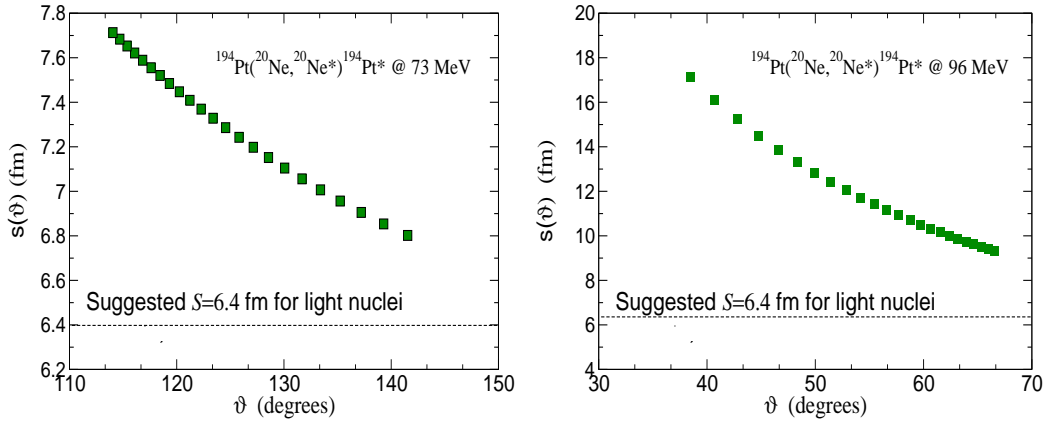


Figure 3.8: $s(\vartheta)$ as a function of average ϑ .

The S3 detector was placed 15 mm from the target position at forward and backward angles with respect to the beam axis. This ensured that the minimum safe distance is well above 6.5 fm for the chosen beam energies and angular ranges.

3.7 Results of the *Gosia* simulation

The integrated count rates per three rings were plotted against the average angular coverage of the scattered particles for the $^{194}\text{Pt}(^{20}\text{Ne}, ^{20}\text{Ne}^*)^{194}\text{Pt}^*$ experiment when the S3 detector is placed 15 mm downstream (figure 3.9) and upstream (figure 3.10) of a $1 \text{ mg}\cdot\text{cm}^2$ thick ^{194}Pt target. In both cases, the simulated results indicate that the measurements carried out at both angular ranges are sensitive to the value of $Q_S(2_1^+)$.

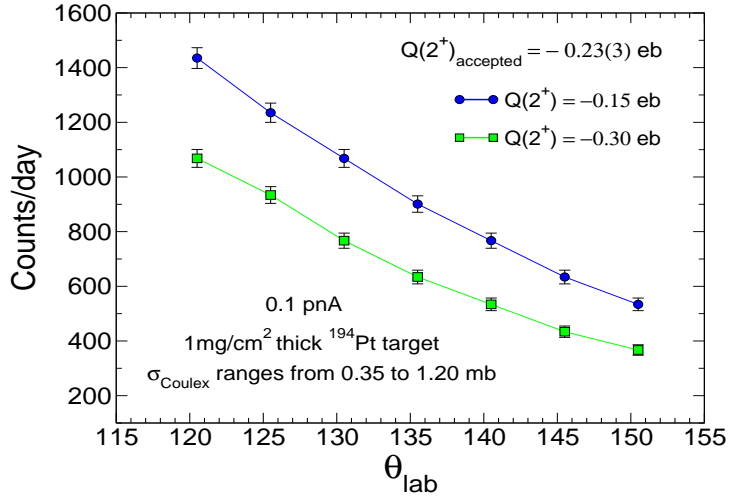


Figure 3.9: Integrated γ -ray yield, calculated with *Gosia* for the $^{194}\text{Pt}(^{20}\text{Ne}, ^{20}\text{Ne}^*)^{194}\text{Pt}^*$ reaction at 73 MeV with an S3 detector at backward angles.

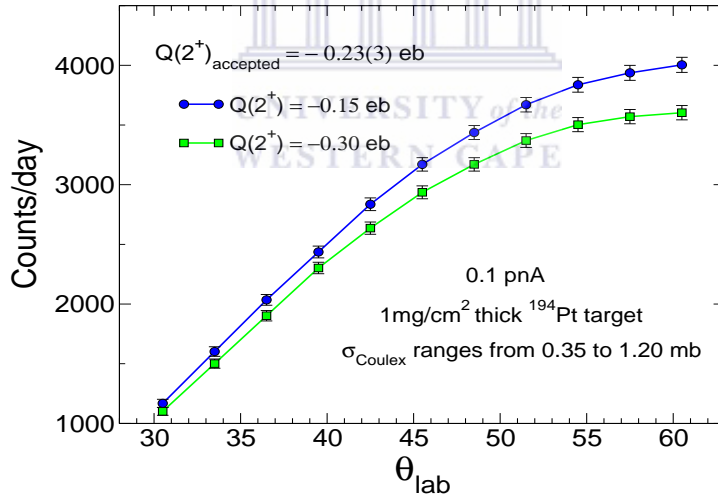


Figure 3.10: Integrated γ -ray yields, calculated with *Gosia* for the $^{194}\text{Pt}(^{20}\text{Ne}, ^{20}\text{Ne}^*)^{194}\text{Pt}^*$ reaction at 96 MeV with an S3 detector at forward angles.

3.8 The $^{194}\text{Pt}(^{20}\text{Ne}, ^{20}\text{Ne}^*)^{194}\text{Pt}^*$ experiment

3.8.1 $^{194}\text{Pt}(^{20}\text{Ne}, ^{20}\text{Ne}^*)^{194}\text{Pt}^*$ experiment at backward angles

The $^{194}\text{Pt}(^{20}\text{Ne}, ^{20}\text{Ne}^*)^{194}\text{Pt}^*$ experiment was carried out at iThemba LABS over the course of two weekends during Nov-Dec 2013. The safe Coulomb excitation of $^{20}\text{Ne}^{3+}$ beams at a beam energy of 73 MeV bombarded a ^{194}Pt target having of $1.2 \text{ mg}\cdot\text{cm}^2$ thickness. The γ -rays were detected using the AFRODITE array shown in the right panel of figure 3.11, consisting of nine clover detectors: six positioned at 90° , and three at 135° . The S3 detector is shown on the left panel of figure 3.11, when placed in the target chamber that had been made for experiments. These measurements were done at backward angles ranging from 113.4° to 141.5° .

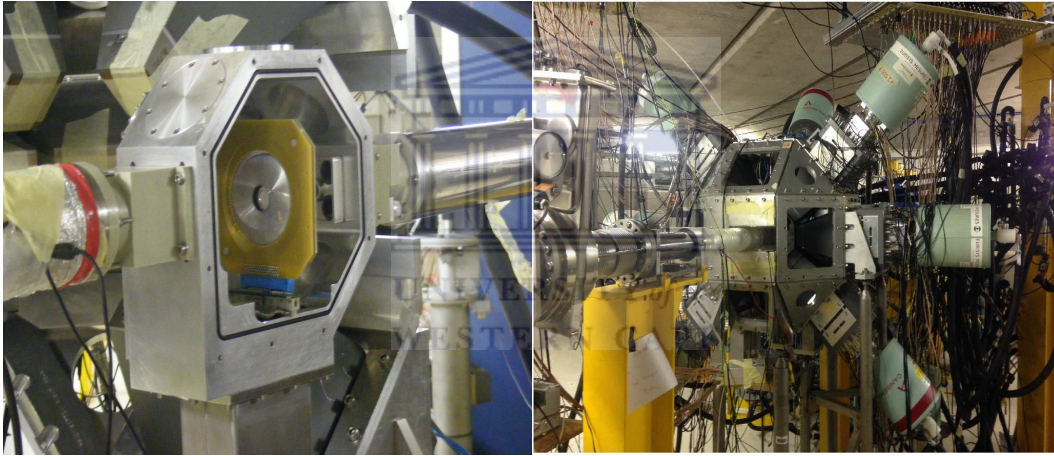


Figure 3.11: The S3 detector (left) and the AFRODITE array (right).

The Sommerfeld parameter for this experiment was $\eta = 70.9$, indicating that the semiclassical approximation is satisfied. The calibrations of the clover detectors were done using standard ^{152}Eu and ^{56}Co radioactive sources, while the S3 detector was calibrated using a ^{226}Ra source. These calibrations were carried out before and after both of the $^{194}\text{Pt}(^{20}\text{Ne}, ^{20}\text{Ne}^*)^{194}\text{Pt}^*$ experiments.

3.8.2 $^{194}\text{Pt}(^{20}\text{Ne}, ^{20}\text{Ne}^*)^{194}\text{Pt}^*$ experiment at forward angles

A $^{20}\text{Ne}^{3+}$ beam at an energy of 96 MeV was bombarded onto a enriched ^{194}Pt target of $2\text{ mg}\cdot\text{cm}^2$ thickness. The $^{20}\text{Ne}^{3+}$ ions were detected with the S3 detector, which was placed at a distance of 15 mm downstream in front of the target and covered a forward angular range of $[38.5^\circ, 66.5^\circ]$. The AFRODITE array was used to detect the γ -rays emitted in the de-excitation of states in ^{20}Ne and ^{194}Pt . The position of the clovers were the same as those utilized during the first weekend of the experiment. The (θ, ϕ) angles of each clover detector is given in table 3.1.

clover	θ ($^\circ$)	ϕ ($^\circ$)
1	90	45
2	90	90
3	90	135
4	90	315
5	135	0
6	90	270
7	135	90
8	90	225
9	135	270

Table 3.1: Geometry of the AFRODITE array: (θ, ϕ) configurations at the center of each clover detector used for the $^{194}\text{Pt}(^{20}\text{Ne}, ^{20}\text{Ne}^*)^{194}\text{Pt}^*$ experiment.

Again, the requirement for nuclear excitation to be negligible was ensured by having $s(\vartheta) > 6.5$ fm at all angles. The Sommerfeld parameter for the ^{194}Pt - ^{20}Ne system at 96 MeV is $\eta = 61.8$, indicating that the semiclassical approximation is satisfied.

3.9 The $^{208}\text{Pb}(^{40}\text{Ar}, ^{40}\text{Ar}^*)^{208}\text{Pb}^*$ experiment

This experiment was conducted in March 2015. A $^{40}\text{Ar}^{7+}$ beam of energy 143 MeV was bombarded onto a $1.4\text{ mg}\cdot\text{cm}^2$ thick ^{208}Pb target. Again, the AFRODITE array was used to detect the γ -rays emitted from the de-excitation of states in the ^{208}Pb and ^{40}Ar nuclei. An S3 detector which had

been placed 10 mm from the target was used to detect the scattered $^{40}\text{Ar}^{7+}$ ions at backward angles ranging from 106.1° to 130.0° .

clover	θ ($^\circ$)	ϕ ($^\circ$)
1	90	90
2	90	45
3	90	225
4	90	315
5	135	0
6	135	180
7	135	90
8	135	270

Table 3.2: Geometry of the AFRODITE array: (θ, ϕ) configurations at the center of each clover detector used for the $^{208}\text{Pb}(^{40}\text{Ar}, ^{40}\text{Ar}^*)^{208}\text{Pb}^*$ experiment.

The (θ, ϕ) angles of each clover are given in table 3.2. Beam focusing problems were avoided by taking special precautions and considered an aluminum collimator with a diameter of 20 mm, wrapped in tantalum foil, placed 110 mm from the target. In addition, a second collimator with a diameter of 12 mm possessing dimensions similar to that of the S3 detector was placed 6 mm downstream in front of a damaged S3 detector. A damaged detector was used for testing purposes to prevent damage to the actual S3 detector.

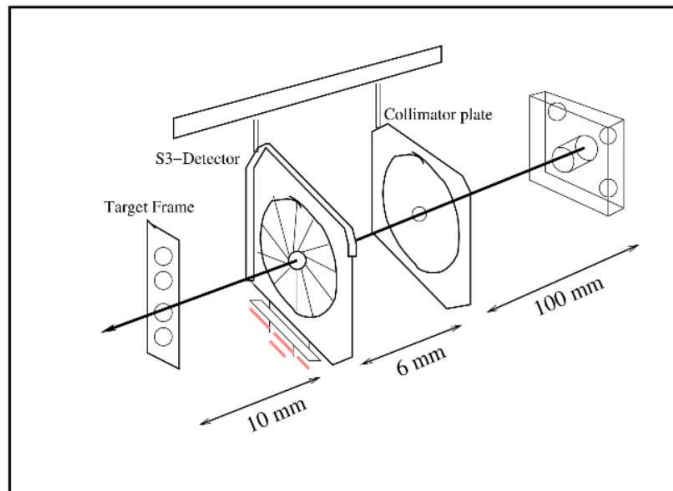


Figure 3.12: Shielding setup for the $^{208}\text{Pb}(^{40}\text{Ar}, ^{40}\text{Ar}^*)^{208}\text{Pb}^*$ experiment.

The collimator was used to prevent the beam from hitting the detector directly. Once the focusing tests were completed the damaged S3 detector was replaced with the S3 detector used during the experiment. A diagram illustrating these modifications is shown in figure 3.12. The requirement that the effects of nuclear interference could be taken to be negligible was ensured by having $s(\vartheta) > 6.5$ fm at all angles. A Sommerfeld parameter of $\eta = 146.6$ indicates that the semiclassical approximation is valid.



Chapter 4

Data analysis and sorting code

4.1 Calibrations

Further data processing was carried out using the Multi Instance Data Acquisition Software (*MIDAS*) analysis package [37] together with *MTsort* [38]. The γ -ray and particle data were calibrated using ^{152}Eu , ^{56}Co and ^{226}Ra radioactive sources, and the resulting calibration coefficients were used in the sorting routine to process the raw data. The use of these calibrations and the methods that were used to perform these calibrations will now be presented.

4.1.1 Efficiency calibration

The efficiency calibration of the clover detectors was carried out by placing ^{56}Co (figure 4.1) and ^{152}Eu (figure 4.2) calibration sources at the target position. Data were taken, both before and after each of the measurements. The *gf3* [48] executable file was then used to run a .cmd file, containing the Radware commands to determine, save and output the values of the centroids, peak areas, peak energies and their associated uncertainties to a .sto file. The .sto file acts as a input file to the *Source* executable which generates a .sou file containing the .sto file together with the energies and relative intensities of standard γ -ray sources. This file is then input to the *effit* executable which fits a efficiency curve to the data using the following expression

$$\ln(\epsilon) = [\epsilon_l + \epsilon_h]^{-\frac{1}{G}}, \quad (4.1)$$

where ϵ_l and ϵ_h denote the efficiencies of the low and high energy regions and G is the interaction parameter between the two regions [48]. The efficiencies ϵ_l and ϵ_h are computed as follows [48]

$$\epsilon_l = (A + Bx + Cx^2)^{-G}, \quad (4.2)$$

here A, B and C denote the fitting parameters for the low energy region of the γ -ray spectrum and, $x = \log\left(\frac{E_\gamma}{E_1}\right)$, with $E_1 = 100$ keV.

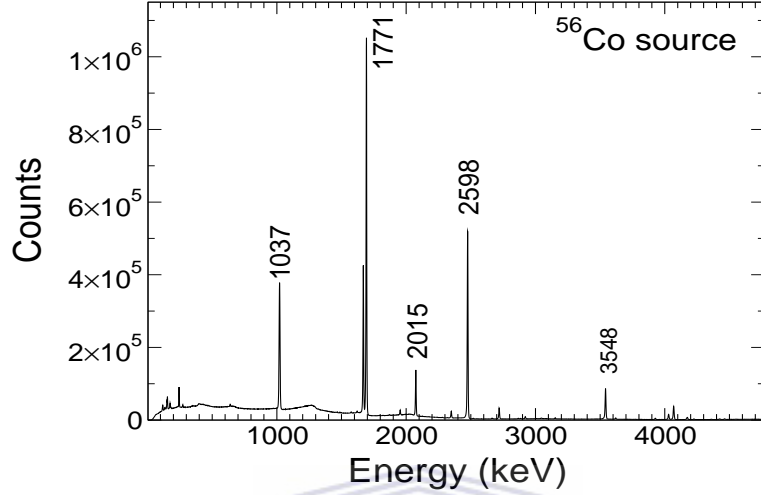


Figure 4.1: Singles γ -ray spectrum of ^{56}Co source.

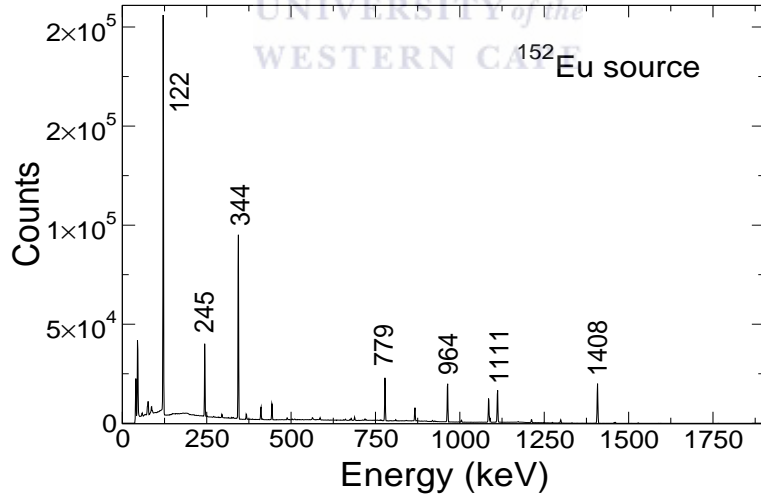


Figure 4.2: Singles γ -ray spectrum for the ^{152}Eu source.

For the high energy region, ϵ_h is given by [48],

$$\epsilon_h = (D + Ey + Fy^2)^{-G}, \quad (4.3)$$

where D, E and F denote the fitting parameters for the low energy region of the γ -ray spectrum and $y = \log(\frac{E}{E_2})$, with $E_2 = 1$ MeV. The program also allows for the addition of data points from another .sou file. In this case, either the ^{56}Co or ^{152}Eu .sou files depending on which of these was input to the *effit* [48] executable.

Parameter	A	B	C	D	E	F	G
value	6.62	0.7	0.0	5.198	-0.588	0.009	15.0

Table 4.1: Fit parameters for efficiency calibration.

The program then determines the normalization factor required to normalize the data from the second data set input to the program to that of the first. The fitting process was then repeated until a minimization was obtained. The fit parameters were output to a .aef file. Table 4.1 shows the resulting fit parameters and figure 4.3 shows the resulting efficiency curve.

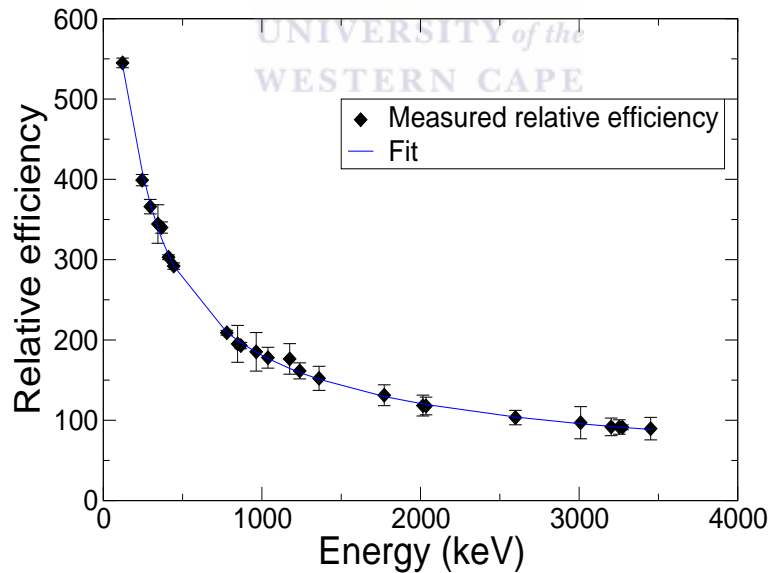


Figure 4.3: HPGe clover detector efficiency calibration.

4.1.2 HPGe clover detector energy calibrations

Energy calibrations for the clovers were carried out using a ^{152}Eu and ^{56}Co source before and after each of the Coulomb excitation experiments. An offline sorting code containing commands to generate raw γ -ray spectra for each of the crystals was input to the *MTsort* [38] and *MIDAS* [37] software packages. The auto-calibration option in the *MIDAS* software package was then used to obtain the coefficients of a polynomial of degree 1, which had to apply to a particular spectrum to obtain one-to-one correspondence between the channel numbers of the centroids in the spectrum corresponding to the energies of seven peaks belonging to the ^{152}Eu source. In the case of the $^{194}\text{Pt}(^{20}\text{Ne}, ^{20}\text{Ne}^*)^{194}\text{Pt}^*$ experiment, the auto-calibration option was able to identify all 7 of the strong ^{152}Eu peaks in most the γ -ray spectra but not all. The channel numbers of the peaks which were not identified as belonging to ^{152}Eu were used to perform the calibration manually. The resulting gain and offset coefficients were then input into the offline sort code which generated calibrated γ -ray spectra as output after being sorted using the *MIDAS* [37] and *MTsort* [38] software packages.

4.1.3 S3 detector energy calibrations

Energy calibrations for each of the 24 rings and 32 sectors were carried out using a two point calibration in which one peak of a ^{226}Ra source was used in conjunction with elastic peaks simulated by *GEANT4*. The resulting gain and offset coefficients were then used in a offline sorting code to generate the calibrated particle energy spectra. The resulting energies are compared with kinematics and energy loss calculations in section (4.2.1) performed independently using a home written code in conjunction with *SRIM* [50]. The kinematics used in this code can be found in appendix B.

The gain and offset coefficients obtained from the two point calibration were used in the offline sorting code containing commands to generate the calibrated particle spectra for each ring and sector. Figure 4.4 shows the particle energy spectra for the first seven rings obtained from the two point calibration.

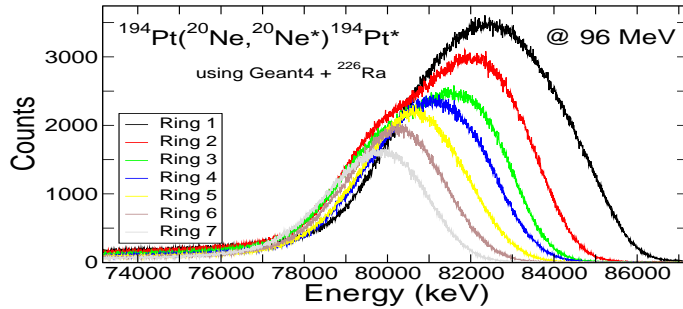


Figure 4.4: Particle spectra for the seven innermost rings calibrated using a ^{226}Ra source in conjunction with *GEANT4* simulations.

4.2 *GEANT4* simulations

GEANT4 is the acronym given to the geometry and tracking *C++* tool-kit that is utilized to perform simulations of the passage of particles through matter. *GEANT4* performs Monte Carlo simulations that consist of various physical models. These physical models accommodate various geometries, particle interactions and processes. When utilizing *GEANT4*, the user constructs 3D simulation environments by defining the volume of the geometry required as well as the materials the system is comprised of. Once the 3D simulation environment has been constructed, the projectile particles can be fired into the simulation environment by specifying the projectile energy and direction. The interaction processes built in the simulation is used to record the energy, position and time information of the events between the projectile particles and the constructed simulation environment.

The *GEANT4* code (version 4.10) utilized in this work was adopted from an existing *GEANT4* code developed by Erasmus [30] to simulate elastic peaks in silicon detectors after Rutherford scattering. A *GEANT4* simulation of the scattered particles incident on the S3 detector were performed using the $^{194}\text{Pt}(^{20}\text{Ne}, ^{20}\text{Ne}^*)^{194}\text{Pt}^*$ Coulomb excitation reaction described earlier. A detailed account of the code can be found in Ref. [30]. The features of the code that were of particular interest to this work were the energy losses and Rutherford scattering processes whose results were used for the calibration of ring and sectors.

The transportation process [31] determines the limit of a step or two points

on the particles trajectory, together with a track of the energy loss and time of flight. The means by which the geometric limit of the step is determined varies and depends on whether or not the particle is charged. If the particle of interest is not charged, the transportation process *GEANT4* is compromised by computing the length of a step with which a track will enter a new volume. Once the track of the particle arrives at the boundary of the volume, the transportation process locates the next track.

For charged particles, the electromagnetic field is responsible for the transportation process [31]. This is done automatically in *GEANT4* in the case of a magnetic or electromagnetic field by solving the equations of motion for the particle of interest and updating the time of flight using the initial velocity. The solutions to these equations of motion are obtained via Runge-Kutta methods, which depend on a numerical analysis used to approximate the field [31].

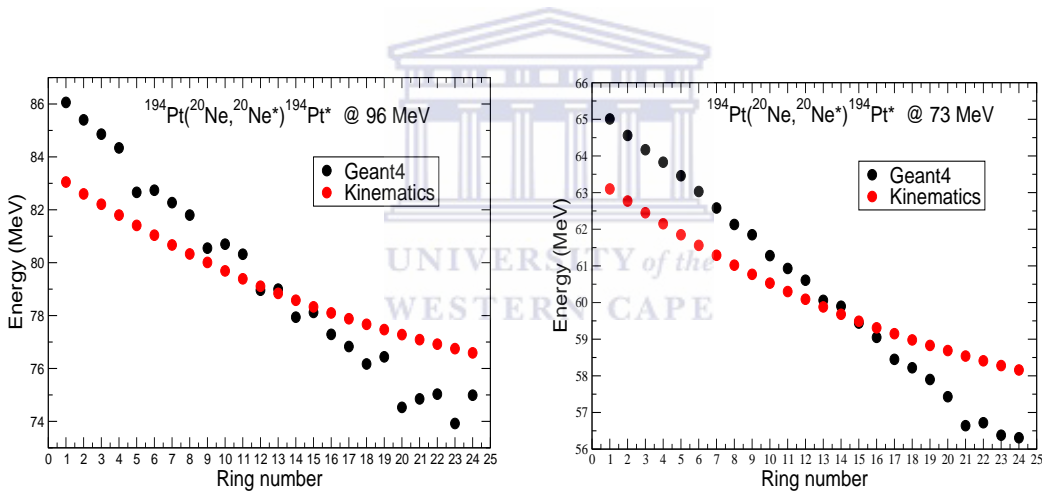


Figure 4.5: Kinematics and GEANT4 predicted energies for the elastic peaks detected on the rings at forward (left) and backward (right) angles.

In the case of fields other than the electromagnetic field, the user can supply the equations of motion. Figure 4.5 shows the results of kinematics calculations compared to a *GEANT4* simulation at forward and backward angles for the elastic peaks scattered on the 24 of the rings of the S3 detector. *GEANT4* utilizes various energy loss processes to compute the discrete and continuous

energy loss of a particle possessing a total incident energy E in a material of density ρ , given the run time and upon completion of a given step. These average energy loss calculations are carried out using the $\frac{dE}{dx}$ stopping powers and inverse range tables from *SRIM* [50].

4.3 Particle energy loss

When charged particles interact with matter they lose energy as a result of the scattering with atomic electrons and with nuclei. In the case where $m_e \ll m_p < m_t$, the projectile losses small fractions of its incident energy as it travels through the target material due to inelastic scattering with the electrons in the target material. Since $Z_t > Z_p$ the number of collisions between the projectile and the electrons in the target material per unit path length is large, and the projectile can transfer a significant amount of energy to these electrons. This is the situation in Coulomb excitation RE measurements. Since these measurements are carried out at safe energies and $m_p < m_t$, the amount of energy transferred to m_t will be much less than the amount transferred to the electrons in the target material, consequently the amount of energy transferred to these electrons will be much greater than the contributions arising from elastic scattering between the m_t and m_p [28].

These scattering processes are statistical and result in small fluctuations

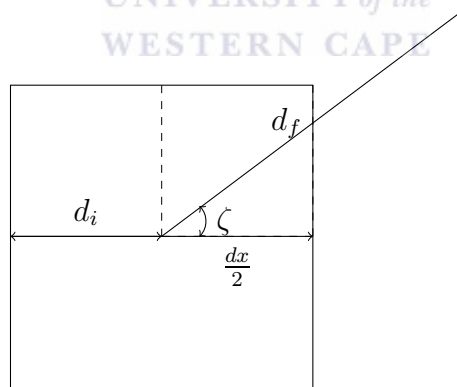


Figure 4.6: center of target scattering event.

[28] in the energy loss, which leads to the concept of the stopping power, $\frac{dE}{dx}$, i.e, the average energy dE loss per unit path length dx . The stopping power

can be computed using the Bethe-Bloch formula, which is given by [28]

$$\frac{dE}{dx} = 2\pi N_a r_e^2 m_e c^2 \rho_t \frac{Z_p Z_t}{A \beta_p^2} \left[\ln \left(\frac{2m_e (v\gamma)^2 W_{max}}{I^2} \right) - 2\beta_p^2 \right]. \quad (4.4)$$

Where $2\pi N_a r_e^2 m_e c^2 = 0.01535 \text{ MeV cm}^2/\text{g}$, I is the mean excitation potential, $\gamma = \frac{1}{\sqrt{1-\beta_p^2}}$ and W_{max} is the maximum energy that can be transferred in a single collision. For a head-on collision W_{max} is given by [29]

$$W_{max} = \frac{2m_e c^2 (\beta_p \gamma)^2}{1 + 2\left(\frac{m_e}{m_p}\right) \sqrt{1 + (\beta_p \gamma)^2 + \left(\frac{m_e}{m_p}\right)^2}}. \quad (4.5)$$

If $m_p \gg m_e$ the expression for W_{max} reduces to $2m_e c^2 (\beta \gamma)^2$ [28]. The value of $\frac{dE}{dx}$ obtained from the Bethe-Bloch formula can be used to compute the energy that the incident beam loses as a result of the scattering with the target. The energy of the beam after the scattering event, E , can be written as

$$E = E_{pf} - \frac{dE}{dx} dx \quad (4.6)$$

where dx is the target thickness and E_{pf} , the energy of the projectile nucleus after scattering. In the case considered here $dx = dx_a$, where dx_a is the apparent thickness of the target. If the scattering event is assumed to occur in the center of the target, dx_a can be found by adding the distance that the incident particle covers before the scattering event to the distance the incident particle covers after the scattering event, as shown in the figure 4.5, where dx_a is given by

$$dx_a = d_i + d_f = \frac{dx}{2} (1 + \sec(\zeta)), \quad (4.7)$$

the energy of the beam projectile after the scattering event, given by equation 4.6, can be written as

$$E = E_{1f} - \frac{dE}{dx} dx_a = E_{if} - \frac{dE}{dx} \left(\frac{dx}{2} (1 + \sec(\zeta)) \right). \quad (4.8)$$

In this work the values of $\frac{dE}{dx}$ were obtained from the *SRIM* program [50] which computes $\frac{dE}{dx}$ using equation 4.4 in conjunction with various corrections.

4.4 Sorting code

The main aim of this study is to develop a sorting code that can be used to extract the γ -ray de-exciting the 2_1^+ states in ^{20}Ne and ^{40}Ar , as well as other nuclei using the particle- γ coincidence technique in Coulomb excitation measurements. The sorting code was used during the offline data analysis by implementing the conditions that will now be presented.

4.4.1 Particle coincidence conditions

Background subtraction in the particle and γ -ray spectra was done by implementing various conditions between the rings and sectors. The background due to hits in non-adjacent rings and sectors observed in the particle energy spectra was reduced by imposing a ring and sector coincidence condition for the acceptance of a valid particle detection event.

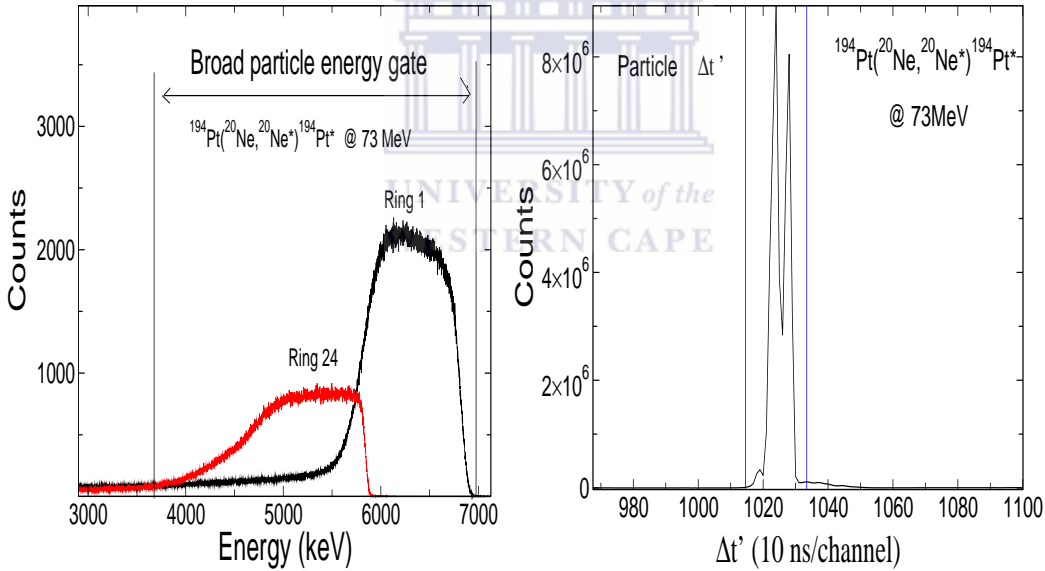


Figure 4.7: Particle coincidence gates used to remove background.

This condition was set up by requiring two simultaneous hits in the S3 detector, one in a ring and one in a sector, together with a ring and sector time

difference (Δt) acceptance gate. In addition, broad particle energy gates were originally applied to the ring spectra. This particle gate or tagging was set so that the particle energy range between the innermost (black) and outermost (red) rings was covered as shown in figure 4.7. From this point onward all time differences will be stated as $\Delta t' = \Delta t + 1024$.

4.4.2 Particle- γ coincidence conditions

The particle- γ coincidence condition was achieved by requiring a combination of a hit in a clover detector and two simultaneous hits in both the rings and the sectors [49], occurring within a time interval equal to the time difference between rings and sectors, which is typically about 100 ns. The time gate on the time difference spectrum between the rings and γ -rays used for the acceptance of a valid γ -ray event, as well the time gates on the background, are shown in figure 4.8. The γ -rays detected outside of this time interval were subtracted. This was done by setting up a two dimensional histogram in which the time difference between the rings and γ -rays were plotted on the x-axis and the γ -ray energies on the y-axis.

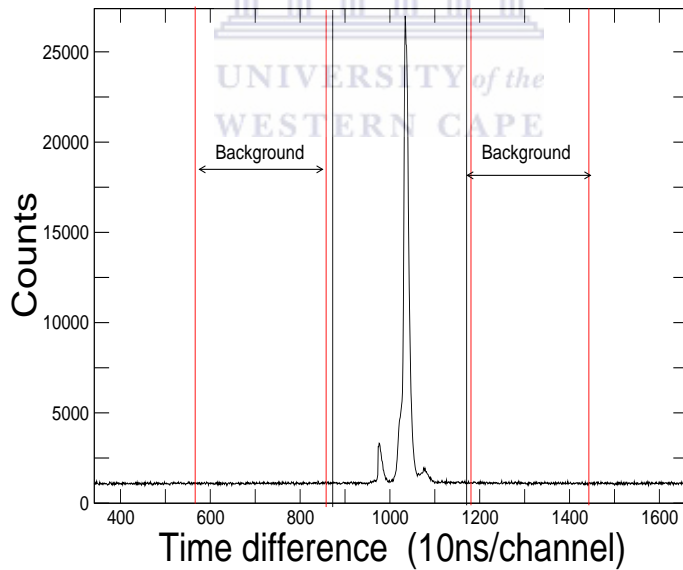


Figure 4.8: Particle- γ $\Delta t'$ spectrum for ^{20}Ne experiment showing the prompt (black) and background (red) particle- γ time gates.

The background subtracted γ -ray spectra were obtained by taking the projection of the events in the coincidence time window and subtracting those outside the coincidence time window onto the y-axis, using the projection option in *MIDAS* GUI [37]. Figure 4.8 shows the prompt time gates for a ring and γ coincidence event (black) and time gates on the background (red) used to reduce the background in the γ -ray spectra.

The θ and ϕ angles of the particles detected in the S3 detector, as well as the θ and ϕ angles at the center of the crystal in which a valid γ -ray detection event occurred were then used to calculate the relative angle between the γ -ray and a particle.

4.4.3 Energy sharing condition

The background in the particle- γ spectra can additionally be reduced using an energy sharing condition. That is, unwanted background events arising when the full energy of a particle is shared between the rings, sectors (active layers) and dead layers of the S3 detector. This background in the γ -ray and particle spectra was reduced by adding an additional particle energy condition to the sorting code which required that $|E_{Sector} - E_{Ring}|$ to be less than a given energy.

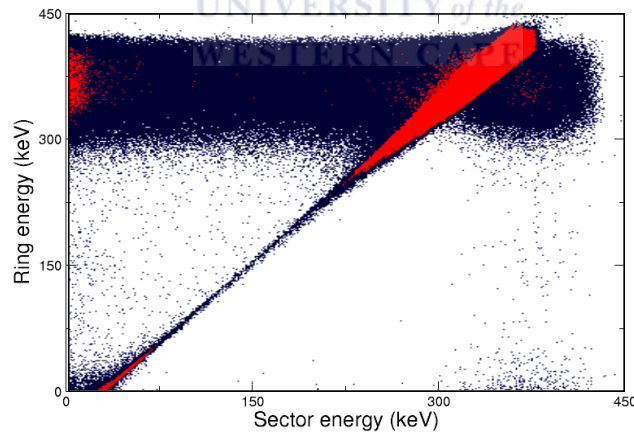


Figure 4.9: 2D histogram of the calibrated sector energy (x-axis) vs ring energy (y-axis) with no energy sharing condition. The off-diagonal events correspond to unwanted background.

This energy condition was chosen by constructing 2D histograms in which the energies of the rings are plotted against the energies of the sectors, similar to that shown in figure 4.9. The upper bound was chosen by incrementing $|E_{Sector} - E_{Ring}|$ in steps of 50 keV ranging from 50 keV to 1050 keV. This condition was used to clean the particle- γ -ray spectra and allows for a better identification of the inelastic peaks and the γ -ray peak of interest. The 2D histograms shown in figure 4.10 below demonstrate the effect of the energy sharing condition. The 2D histogram on the left was generated by imposing the condition requiring two simultaneous hits in the S3 detector together with the ring-sector time coincidence condition. The diagonal line corresponds to the coincidence events, while the off-diagonal events represent the energy sharing events contributing to the background in the γ -ray and particle energy spectra. The 2D histogram on the right shows the effect of imposing a energy sharing condition of 500 keV used to remove the background, while preserving the counts in the γ -ray peak of interest.

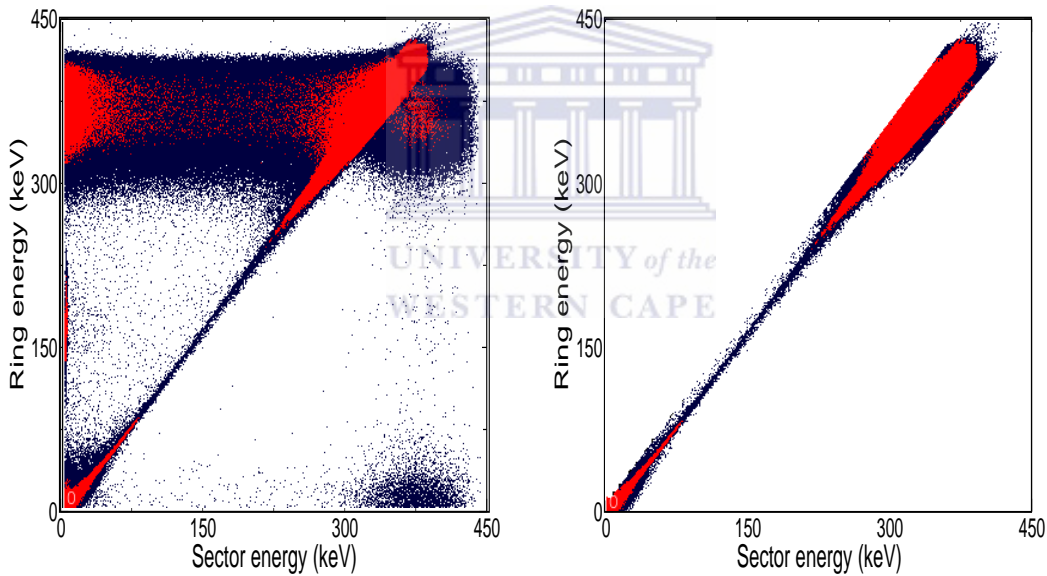


Figure 4.10: 2D energy-sharing histograms, without (left) and, with (right) an energy sharing condition.

4.4.4 Inelastic conditions

Inelastic conditions on the particle energy spectra were used to extract clean γ -ray spectra in coincidence with the particles in the rings. This condition consists of applying particle energy gates where the inelastic peak is expected to appear. In order to ensure that the counts in this region are conserved, the maximum limit of the gate was chosen at an arbitrary distance, ϵ , away from the centroid of the elastic peak, while the minimum limit of the gate was chosen to be at a distance of E_0 , away from the centroid of the elastic peak. Here E_0 denotes the value of the γ -ray emitted in the de-excitation of states in the projectile nuclei, as shown in figure 4.11. The value of ϵ was determined by generating the particle energy spectra for the innermost and outermost rings in which value of ϵ was decreased by increments of 0.5 MeV.

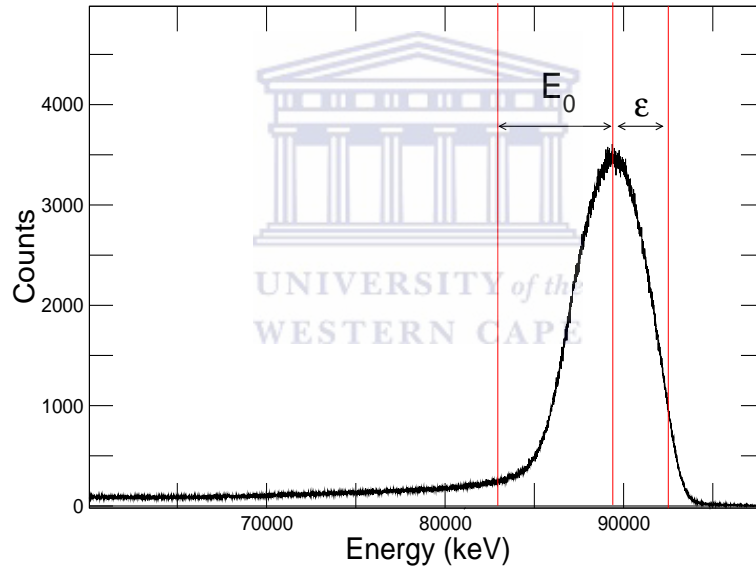


Figure 4.11: Inelastic particle tagging on the first ring of the S3 detector.

Two 2D histograms were used to find choose a suitable value of ϵ . The time difference between the rings and sectors were plotted against the sum of the γ -ray energies on the y-axis, in the first of these 2D histograms. The second 2D histogram was generated by plotting the time difference between the rings and sectors against the ring energy. The ring energy corresponding to each increment of ϵ was then projected onto the x-axis to obtain the time interval

corresponding to the ring energy associated with the corresponding value of ϵ . This time interval was used to generate the associated γ -ray energy spectra by projecting the time interval onto the y-axis. The smallest value of ϵ which preserved the counts in the γ peak in corresponding to E_0 was then used to create a set of inelastic gates for each ring.

4.4.5 Doppler corrections

To correct for the energy shift of the γ -rays emitted by the projectile traveling at $v \approx 0.08c$, a Doppler correction was applied to the γ -ray spectra. This provided a clear identification of the γ -ray of interest. The Doppler correction was carried out using the equation

$$E_{\gamma,k} = \frac{E_{\gamma}(1 - \beta \cos(\theta_{p-\gamma}))}{\sqrt{1 - \beta^2}}, \quad (4.9)$$

where $\beta = \frac{v}{c}$ and $\cos\theta_{p-\gamma} = \frac{\vec{r}_p \cdot \vec{r}_{\gamma}}{|\vec{r}_p||\vec{r}_{\gamma}|}$, denotes the cosine of angle between the projectile nucleus and the emitted γ -ray.

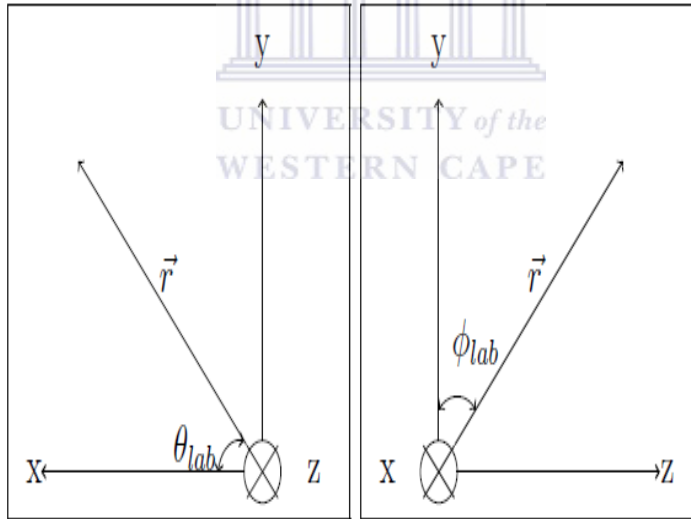


Figure 4.12: Coordinate system used for the Doppler Correction.

The values of β were obtained from the *GEANT4* simulations of the elastic peaks and the ϕ_{γ} and θ_{γ} for each of the crystals were calculated using the

ϕ and θ angles of the center of each clover together with geometric specifications. As mentioned above, the distance from target center to the center of each clover was 196 mm. The implementation of the Doppler correction to the γ -ray used in the sorting code consisted of defining a coordinate system in the laboratory system shown in figure 4.12. Here the positive z-axis points downstream in the direction in which the beam travels and the origin was taken at the center of the target position. The transformation from this coordinate system to the given spherical coordinate system is given by

$$\vec{r}_{\gamma,k} = \begin{pmatrix} d_{ge} \sin(\theta_{kc}) \sin(\phi_{kc}) \\ d_{ge} \sin(\theta_{kc}) \\ d_{ge} \sin(\theta_{kc}) \cos(\phi_{kc}) \end{pmatrix}, \quad (4.10)$$

where $k = 1, \dots, 9$, while d_{ge} denotes the distance from the center of the target position to the center of each clover detector. The given distance to the clover together with ϕ and θ were then used in conjunction with the dimensions of the clover detectors to calculate the (x, y, z) positions at the center of each crystal. The calculation of the ϕ and θ of the S3 detector are carried out by using the specifications of the detector in conjunction with the distance from the target position. The average θ angles of the i^{th} ring of the S3 detector used for the Doppler correction were obtained by using the average of the θ angles, $\bar{\theta}_i$, corresponding to the inner, $r_{i,min}$ (blue) and outer $r_{i,max}$, (green) radii of the i^{th} ring shown in figure 4.13, where d is the distance from the center of the target position to the S3 detector, \bar{r}_i , is the average radius of the i^{th} ring and

$$\bar{\theta}_i = \frac{\tan^{-1}\left(\frac{r_{i,min}}{d}\right) + \tan^{-1}\left(\frac{r_{i,max}}{d}\right)}{2} \quad (4.11)$$

where $i = 1, \dots, 24$. The ϕ angles of the sectors were obtained choosing an arbitrary ϕ_0 , that was added to the average $\bar{\phi}_i$ angle given by,

$$\bar{\phi}_i = \frac{\phi_{i,min} + \phi_{i,max}}{2} \quad i = 1, \dots, 32. \quad (4.12)$$

The result of equation 4.12 was then used to generate 32 sets of ϕ angles to identify the ϕ angle of the first sector. Once the angle of the first sector was identified, the sectors were indexed so that the ϕ angle of the first sector took on the value of ϕ_0 . The value of ϕ_i could be found in the following manner

$$\phi_i = \phi_0 + \bar{\phi}_i. \quad (4.13)$$

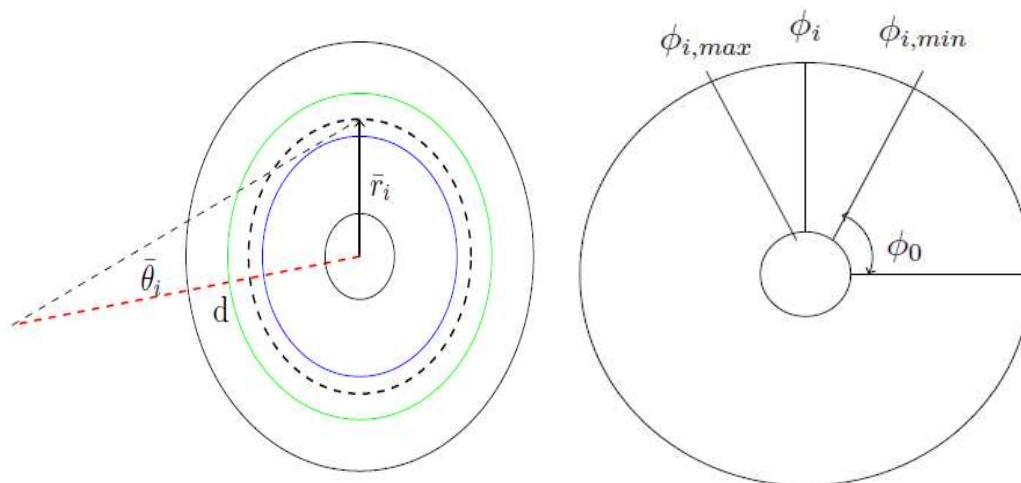


Figure 4.13: S3 detector θ (left) and ϕ (right) angles used in the Doppler correction.

Additional time coincidence gates were then setup for each of the crystals and the rings and sectors of the S3 detectors. The Doppler correction to γ -ray energies for each crystal was then applied to the events which satisfied the energy and time coincidence conditions.

Chapter 5

Results and Discussion

5.1 The $^{194}\text{Pt}(^{20}\text{Ne}, ^{20}\text{Ne}^*)^{194}\text{Pt}^*$ experiment

The $^{194}\text{Pt}(^{20}\text{Ne}, ^{20}\text{Ne}^*)^{194}\text{Pt}^*$ experiment was the first Coulomb excitation experiment at iThemba LABS in which an S3 detector was used in conjunction with the AFRODITE array.

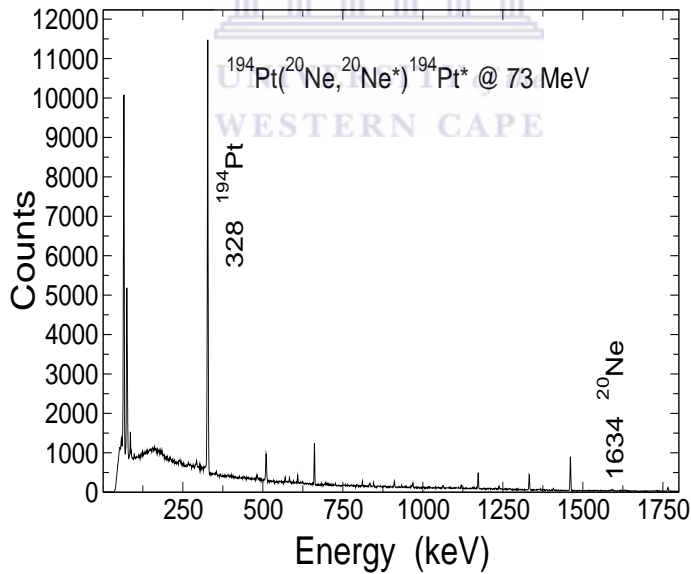


Figure 5.1: Singles γ -ray energy spectrum for the $^{194}\text{Pt}(^{20}\text{Ne}, ^{20}\text{Ne}^*)^{194}\text{Pt}^*$ experiment at backward angles.

The role of the sorting code was to reduce the background in the γ -ray and particle spectra and generate the Doppler corrected γ -ray spectra. This was done so that the peak corresponding to the 2_1^+ state at 1634 keV in ^{20}Ne could be extracted from the raw γ -ray data and used for further Coulomb excitation data analysis in *GOSIA*.

5.1.1 $^{194}\text{Pt}(^{20}\text{Ne}, ^{20}\text{Ne}^*)^{194}\text{Pt}^*$ experiment at backward angles

The calibrated singles γ -ray energy spectrum obtained for this experiment is shown in figure 5.1 without conditions. The peaks that have not been labeled correspond to background lines. Clean information on the peaks of interest can be obtained by imposing the various conditions discussed in the data analysis chapter. The first of these conditions was a broad particle energy gate ranging from 39 MeV to 70 MeV. Figure 5.2 shows the broad energy gate scaled by a factor of 10, covering the range of the elastic peak energies of ring 1 (shown in black) and ring 24 (shown in red).

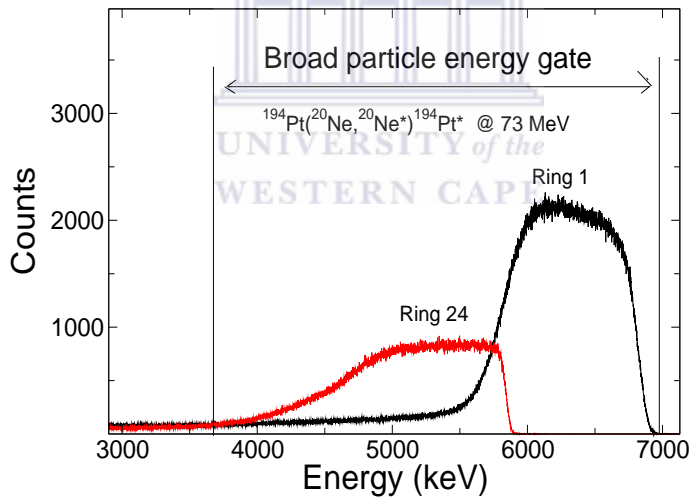


Figure 5.2: Broad particle energy gate for the $^{194}\text{Pt}(^{20}\text{Ne}, ^{20}\text{Ne}^*)^{194}\text{Pt}^*$ experiment at backward angles.

The particles detected within this energy range, together with the ring and sector time coincidence interval, are accepted as valid events, while the particles detected outside these gates are rejected. For the $^{194}\text{Pt}(^{20}\text{Ne}, ^{20}\text{Ne}^*)^{194}\text{Pt}^*$

experiments, the particle $\Delta t'$ spectra were found to have two peaks containing some structures, as shown in the left panel of figure 5.3.

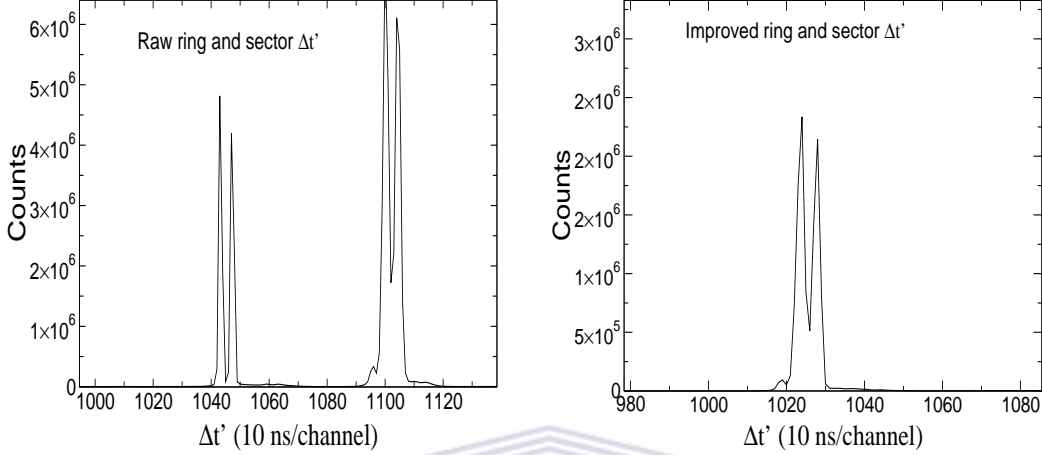


Figure 5.3: Raw (left) and improved (right) particle $\Delta t'$ spectra.

As seen in figure 5.3, the two peaks are separated by about 500 ns. By comparing the $\Delta t'$ spectra for each ring and sector it was found that the first peak was the $\Delta t'$ between the first sixteen rings and the sectors, while the second peak was the $\Delta t'$ between the last 8 rings and sectors. The $\Delta t'$ spectra (figure 5.3) was improved by finding constants, α_i where $i = 1, \dots, 24$ for each ring, and constants β_j , where $j = 1, \dots, 32$ for each sector so that

$$\Delta t_{rs} = (t_s(j) - t_r(i)) + \beta(j) + \alpha(i), \quad (5.1)$$

where Δt_{rs} is the $\Delta t'$ between the rings and sectors of the S3 detector, $t_s(j)$ and $t_r(i)$ denote the timestamps of the j^{th} sector and i^{th} ring respectively, $\beta(j)$ is the constant added to the time stamp of the j^{th} sector, and $\alpha(i)$ is the constant added to the time stamp of the i^{th} ring. The resulting values of $\alpha(i)$ and $\beta(j)$ were used in the sorting code to generate the improved particle $\Delta t'$ spectrum, shown in the right panel of figure 5.3.

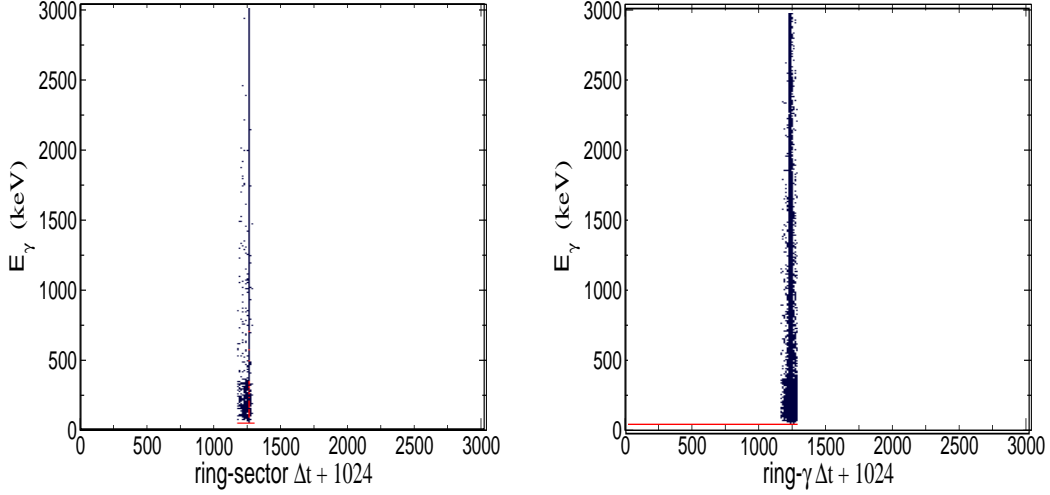


Figure 5.4: 2D histograms for γ energy vs the particle $\Delta t'$ (left) and γ energy vs particle- $\gamma \Delta t'$ (right).

The improved particle $\Delta t'$ spectrum was obtained by using $\beta(j)=0$ for sectors, $\alpha(i)=77$ for rings 1 to 16 and $\alpha(i)=19$ for rings 17 to 24. To compensate for the shift in the $\Delta t'$ between each of the crystals and rings, the values of $\alpha(i)$ together with an additional constant was introduced to align the $\Delta t'$ between the rings and each of the crystals. The improvements to the $\Delta t'$ between each crystal and the sectors resulting from the modifications to the particle $\Delta t'$ were carried out in a similar manner.

2D histograms in which the energy of the γ -ray were plotted against the improved particle- $\gamma \Delta t'$, were used to select the prompt and background time gates used for the particle- γ coincidence conditions and the background subtraction. The 2D histogram shown in the left panel of figure 5.4 shows Doppler corrected γ -ray energy, obtained by adding all of the charge collected in each of the crystals (add-back), for all the rings plotted against the particle $\Delta t'$. The right panel shows the add-back Doppler corrected γ -ray energy for all the rings plotted against the ring and ring- $\gamma \Delta t'$.

The improved $\Delta t'$ spectra were used in conjunction with the broad energy gate (figure 5.2) by imposing the time coincidence gates on the improved ring and sector $\Delta t'$ spectrum shown on the left, (in blue) of figure 5.5. The improved spectra for all of the clover crystals together with the rings are shown

on the right in blue in figure 5.5. The non-Doppler corrected add-back γ -ray spectra for all of the clovers and each of the rings were generated using the particle- γ coincidence conditions. This was done in conjunction with implementing a 1 MeV energy-sharing condition and no inelastic gates as shown in figure 5.6.

The Doppler corrected γ -ray spectrum shown in figure 5.6 for this experiment at backward angles was generated after the energy and time conditions and background subtraction. This was done together with the improved time spectra. The suitable value for the energy sharing condition was selected by generating 2D energy sharing histograms and monitoring the effect of the energy sharing on the Doppler corrected add-back γ -ray spectrum for all rings. These histograms were generated by applying the energy sharing condition in increments of 50 and 100 keV and generating an Doppler corrected add-back γ -ray spectrum for all rings for each increment. From this, a 1 MeV energy sharing condition was selected.

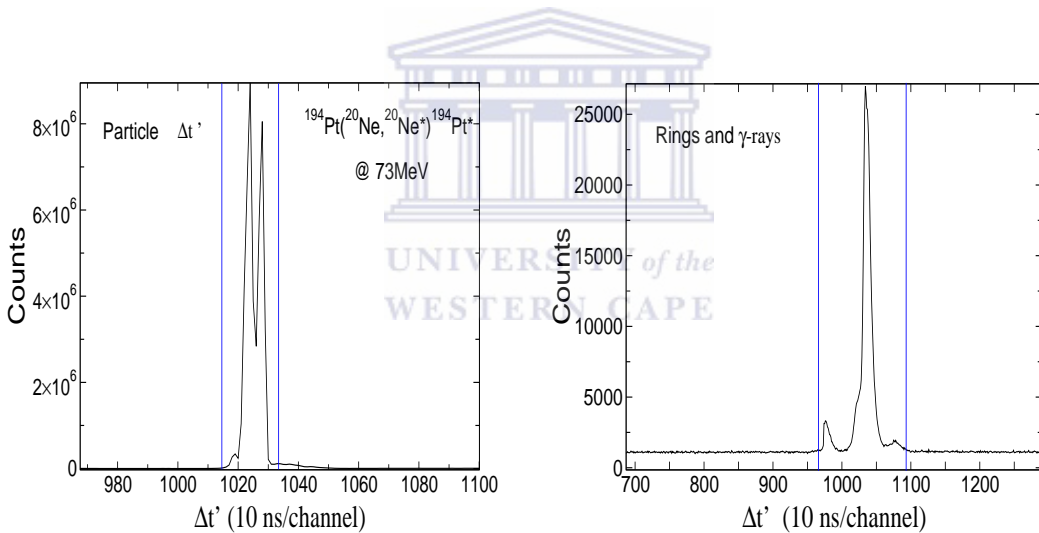


Figure 5.5: Improved particle (left) and particle- γ (right) $\Delta t'$ spectra for the $^{194}\text{Pt}(^{20}\text{Ne}, ^{20}\text{Ne}^*)^{194}\text{Pt}^*$ experiment at backward angles.

As soon as the rings, sectors and γ -rays were put together by applying the particle- γ coincidence conditions the counts in the peak of interest dropped to the point where the peak could not be extracted from the background.

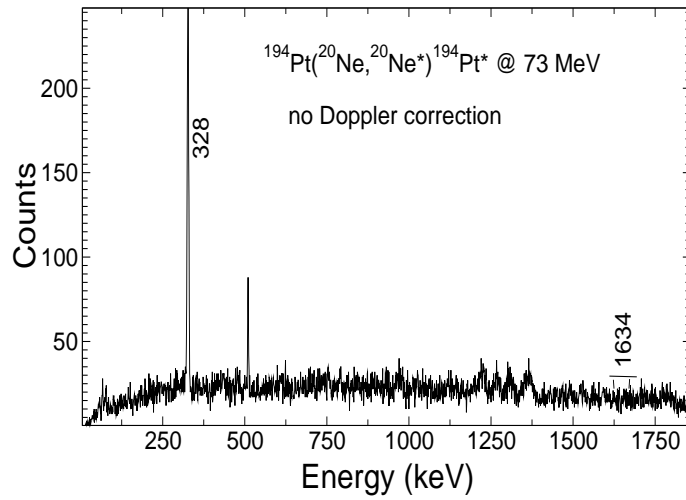


Figure 5.6: Non-Doppler corrected γ -ray spectrum at backward angles.

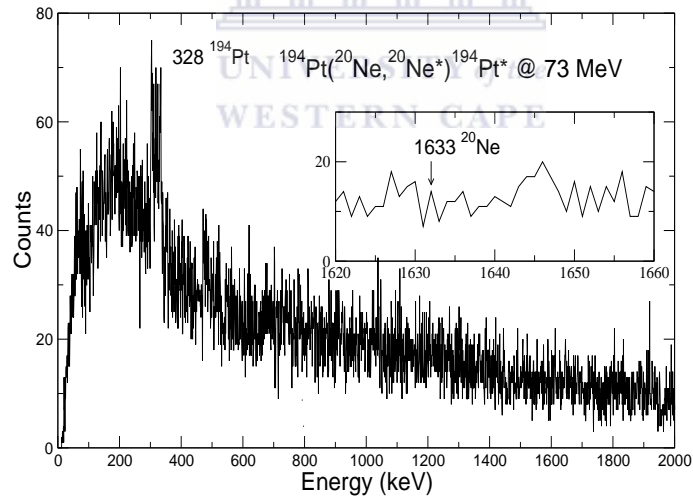


Figure 5.7: Doppler corrected γ -ray spectrum at backward angles.

As a result, the spectrum shown in figure 5.7 shows very little counts for the 1634 keV γ -ray depopulating the 2_1^+ state in ${}^{20}\text{Ne}$ after imposing the

coincidence conditions. The improvement to the timestamps was removed to investigate whether or not the modifications to the timestamps were responsible for the loss of counts in the γ -ray energy spectra.

The result remained unchanged, even though the modifications to the timestamps helped in reducing the background in the γ -ray energy spectra, it did not help in extracting the peak of interest at 1634 keV.

5.1.2 $^{194}\text{Pt}(^{20}\text{Ne},^{20}\text{Ne}^*)^{194}\text{Pt}^*$ experiment at forward angles

The singles γ -ray energy spectrum for the $^{194}\text{Pt}(^{20}\text{Ne},^{20}\text{Ne}^*)^{194}\text{Pt}^*$ experiment conducted at forward angles is shown in figure 5.8. The unmarked peaks correspond to background lines that can be removed by applying the conditions described in the previous chapter.

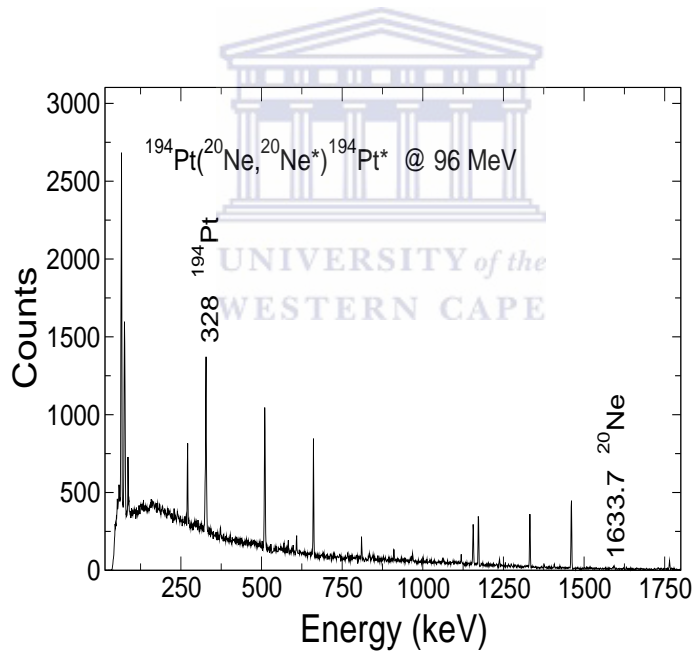


Figure 5.8: Singles γ -ray energy spectrum for the $^{194}\text{Pt}(^{20}\text{Ne},^{20}\text{Ne}^*)^{194}\text{Pt}^*$ experiment at forward angles

The same conditions that were utilized for the first weekend of the experiment and the same set of $\alpha(i)$ and $\beta(j)$ values were used to improve the

timestamps. A broad particle energy gate which took on a minimum value of 72.5 MeV and a maximum value of 98.5 MeV was setup for the rings and sectors.

The particle energy spectra corresponding to the innermost (black) and outermost ring (red) for this experiment are shown in figure 5.9 together with the broad particle energy gate. Here the energies are shown divided by a factor of 2. The coincidence condition required that hits in both a ring and a sector occur within a time interval equal to the Δt between rings and sectors. The energy sharing condition and the inelastic condition removed most of counts in the range 1500 to 1700 keV. Figure 5.11 shows the non-Doppler corrected add-back γ -ray energy spectrum in coincidence with the rings. The Doppler corrected add-back γ -ray energy spectra for the second $^{194}\text{Pt}(^{20}\text{Ne}, ^{20}\text{Ne}^*)^{194}\text{Pt}^*$ experiment is shown in figure 5.12. Again, the improvement to the timestamps was removed to investigate whether or not the modifications to the timestamps were responsible for the loss of counts in the γ -ray energy spectra, but the result remained unchanged.

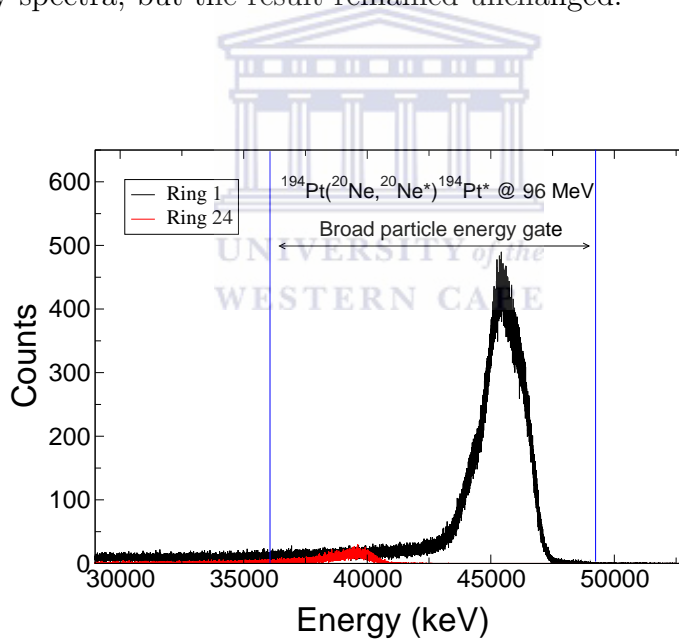


Figure 5.9: Broad particle energy gate for the $^{194}\text{Pt}(^{20}\text{Ne}, ^{20}\text{Ne}^*)^{194}\text{Pt}^*$ experiment at forward angles.

Analogous to the $^{194}\text{Pt}(^{20}\text{Ne}, ^{20}\text{Ne}^*)^{194}\text{Pt}^*$ experiment conducted at backward angles the peak of interest at 1634 keV could not be extracted after applying

the coincidence conditions.

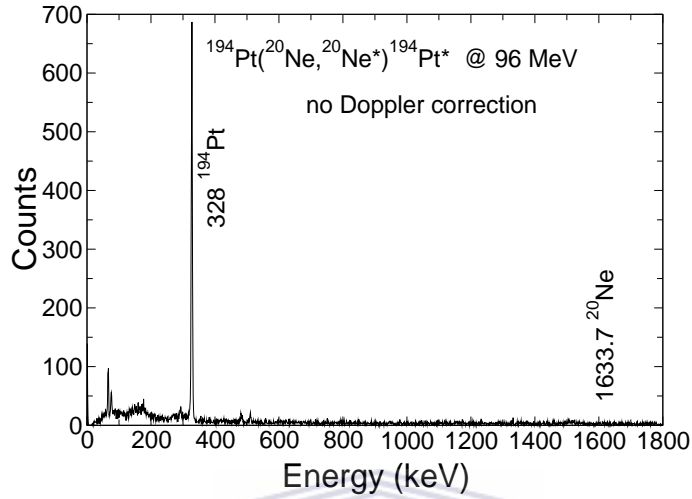


Figure 5.10: Non-Doppler corrected γ -ray spectrum at forward angles.

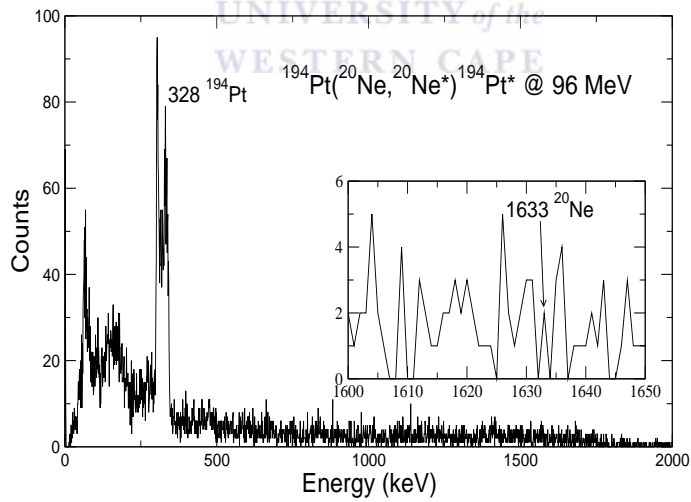


Figure 5.11: Doppler corrected γ -ray spectrum at forward angles.

5.2 The $^{208}\text{Pb}(^{40}\text{Ar}, ^{40}\text{Ar}^*)^{208}\text{Pb}^*$ experiment

The analysis of the data obtained from the $^{208}\text{Pb}(^{40}\text{Ar}, ^{40}\text{Ar}^*)^{208}\text{Pb}^*$ experiment was carried out using a similar sorting code to the one used for the ^{20}Ne experiments. A broad particle energy gate which took on a minimum value of 45 MeV and a maximum value of 150 MeV was setup for the rings and sectors. The particle energy spectra corresponding to the innermost and outermost rings for the experiment is shown scaled by a factor of 10 in figure 5.12.

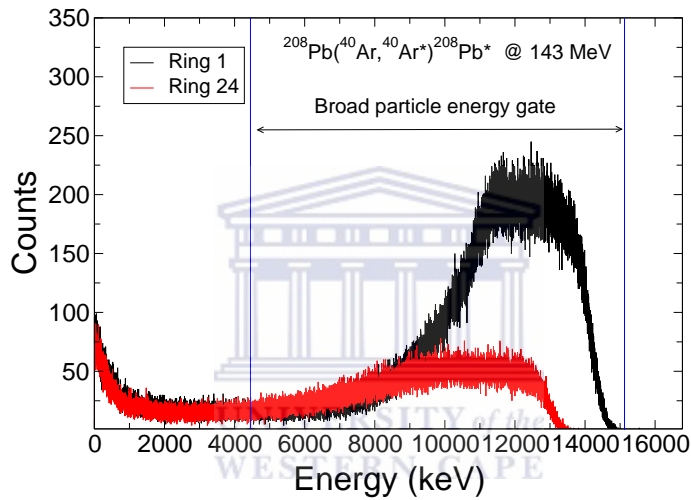


Figure 5.12: Broad particle energy gate for the $^{208}\text{Pb}(^{40}\text{Ar}, ^{40}\text{Ar}^*)^{208}\text{Pb}^*$ experiment.

The broad particle energy gate used for the $^{208}\text{Pb}(^{40}\text{Ar}, ^{40}\text{Ar}^*)^{208}\text{Pb}^*$ experiment data analysis (blue vertical lines in figure 5.12), covering the range of the elastic peak energies of the inner (black) and outermost (red) rings was used in conjunction with the particle- γ coincidence condition between the rings, sectors and clovers. This time interval was used together with time gates on the ring- γ $\Delta t'$, as well as the sector- γ $\Delta t'$, as shown in figure ??.

Figure ?? shows the gates (in red) imposed on the $\Delta t'$ spectra between the rings and clovers (left) as well as the particle $\Delta t'$ spectrum (right) that were used to setup the time coincidence conditions for the acceptance of valid

detection events.

The relatively high background in the particle and γ -ray energy spectra after imposing the time and energy coincidence conditions was reduced by setting up 24 energy sharing gates, as well as 24 inelastic particle energy gates for each ring.

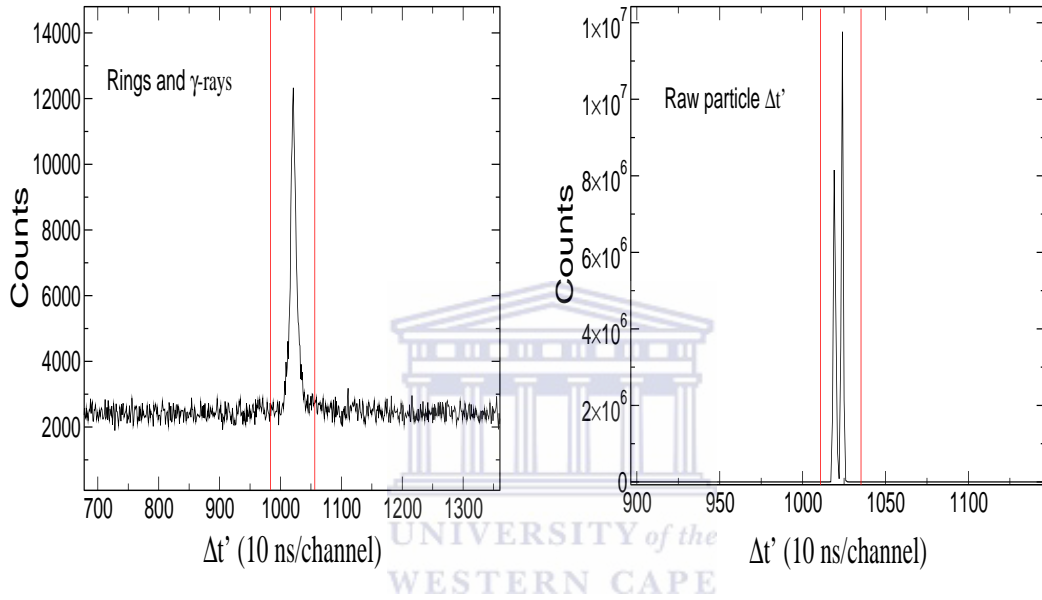


Figure 5.13: Particle (left) and particle- γ (right) $\Delta t'$ spectra for the $^{208}\text{Pb}(^{40}\text{Ar}, ^{40}\text{Ar}^*)^{208}\text{Pb}^*$ experiment.

The events registered in each of the clovers within a time interval equal to $\Delta t'$ between a particular ring and each of crystal were used to generate the non-Doppler corrected add-back γ -ray energy spectrum for all of the rings is shown in figure 5.14. The total Doppler corrected add-back γ -ray energy spectrum adding all clovers in coincidence with all the rings is shown in figure 5.15.

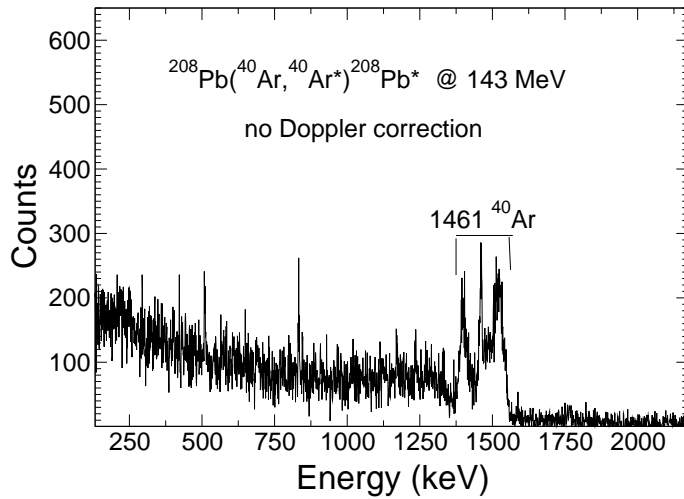


Figure 5.14: $^{208}\text{Pb}(^{40}\text{Ar}, ^{40}\text{Ar}^*)^{208}\text{Pb}^*$ non-Doppler corrected γ -ray spectrum.

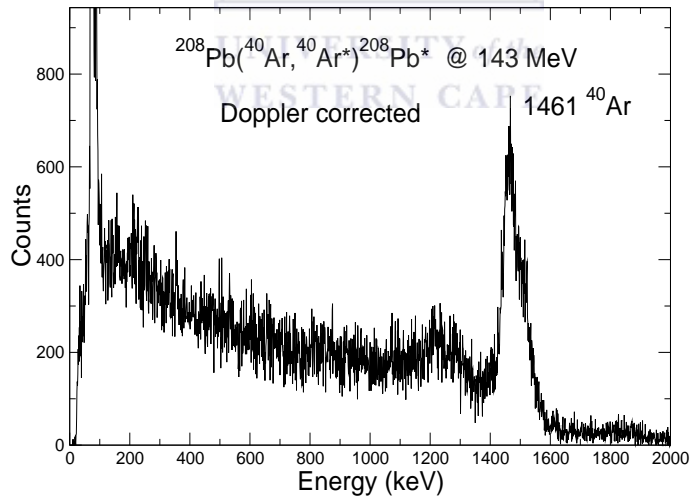


Figure 5.15: $^{208}\text{Pb}(^{40}\text{Ar}, ^{40}\text{Ar}^*)^{208}\text{Pb}^*$ Doppler corrected γ -ray spectrum.

5.3 Discussions

A sorting code for Coulomb excitation measurements was applied to the $^{194}\text{Pt}(^{20}\text{Ne}, ^{20}\text{Ne}^*)^{194}\text{Pt}^*$ and $^{208}\text{Pb}(^{40}\text{Ar}, ^{40}\text{Ar}^*)^{208}\text{Pb}^*$ data. A 2D histogram for the $^{208}\text{Pb}(^{40}\text{Ar}, ^{40}\text{Ar}^*)^{208}\text{Pb}^*$ experiment in which the ring energy signal (x-axis) is plotted against the clover detector signal (y-axis), where both energies are divided by 4 is shown in figure 5.3. This 2D histogram was used to check for a synchronization signal, obtained by using a cable to the link the signal between the crates used for particles and γ -rays. Based on the analysis of $^{194}\text{Pt}(^{20}\text{Ne}, ^{20}\text{Ne}^*)^{194}\text{Pt}^*$ and $^{208}\text{Pb}(^{40}\text{Ar}, ^{40}\text{Ar}^*)^{208}\text{Pb}^*$ data, the modifications to the experimental setup in the $^{208}\text{Pb}(^{40}\text{Ar}, ^{40}\text{Ar}^*)^{208}\text{Pb}^*$ experiment, together with synchronized γ -rays and particles ensured that the data obtained were usable.

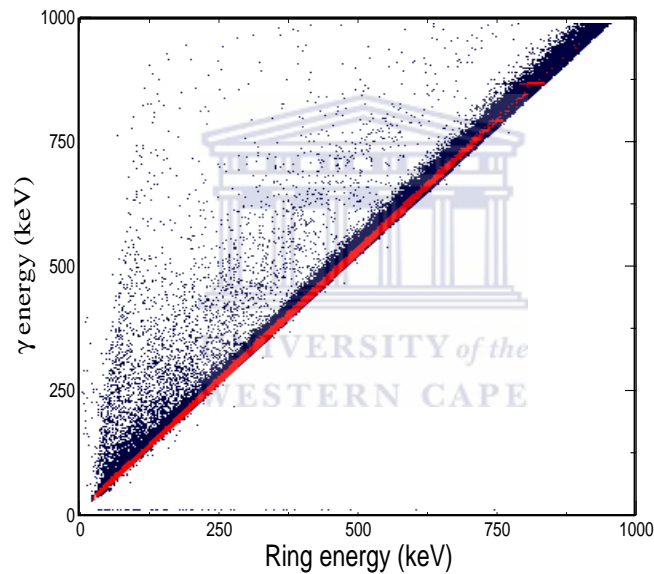


Figure 5.16: 2D histogram showing the ring energy vs γ -ray energy for the $^{208}\text{Pb}(^{40}\text{Ar}, ^{40}\text{Ar}^*)^{208}\text{Pb}^*$ experiment.

The conditions implemented to reduce the background in the γ -ray energy spectra showed that the addition of an energy sharing condition which consisted of applying energy gates to the ring and sector energy differences also reduced the background in the γ -ray spectra, when used in conjunction with the time and energy coincidence conditions.

Figure 5.17 shows the effect on the background as a result of imposing a broad energy gate together an energy sharing condition on the γ -ray energy spectra. These conditions were used in conjunction with the time and energy coincidence conditions (black spectrum), along with the γ -ray energy spectrum, in which the time and energy coincidence conditions were applied with no energy sharing condition (red spectrum).

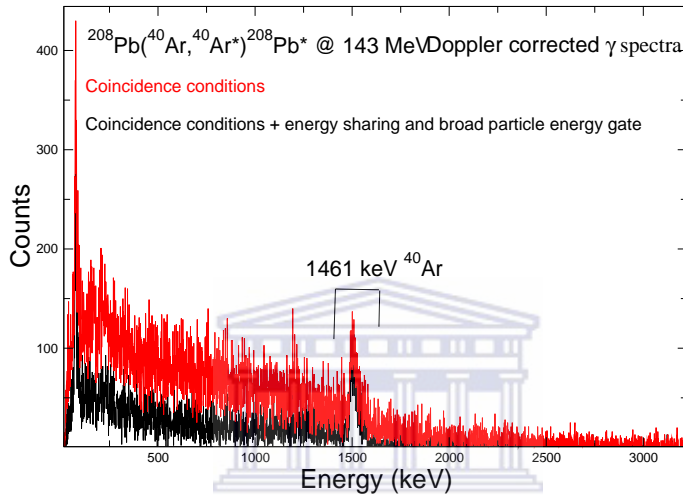


Figure 5.17: Effect of coincidence conditions on the background of the γ -ray energy spectra.

Based on the data analysis of these experiments, the absence of a synchronization signal in the $^{194}\text{Pt}(^{20}\text{Ne}, ^{20}\text{Ne}^*)^{194}\text{Pt}^*$ data over the energy range in which the γ -ray peak of interest appears, may be related to the lack of counts in the 1.633 MeV γ -ray peak in ^{20}Ne . As opposed to the $^{208}\text{Pb}(^{40}\text{Ar}, ^{40}\text{Ar}^*)^{208}\text{Pb}^*$ experiment, the 2D histogram in which the ring energy signal (x-axis) is plotted against the clover detector signal (y-axis), where both energies are divided by 4 (figure 5.18), does not appear to be not synchronized over the entire particle- γ energy range. The events shown in figure 5.18 are responsible for the presence of the 328 keV peak in ^{194}Pt in figures 5.6, 5.7, 5.10 and 5.11. This observation was made by taking projections of the γ -ray energy onto the x-axis.

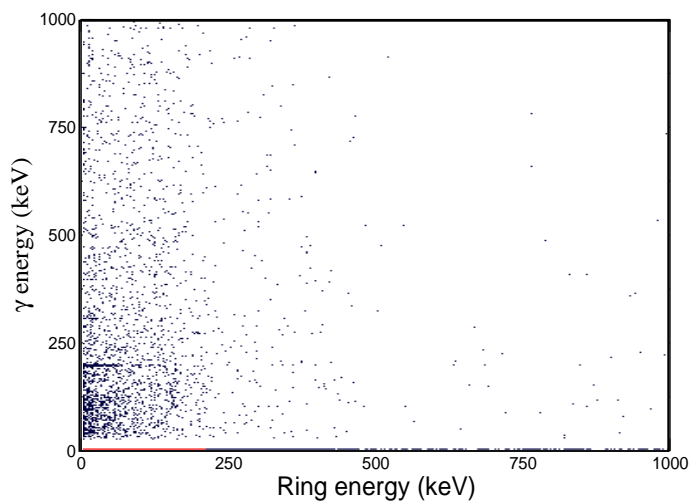


Figure 5.18: 2D histogram showing the ring energy vs γ -ray energy for the $^{194}\text{Pt}(^{20}\text{Ne}, ^{20}\text{Ne}^*)^{194}\text{Pt}^*$ experiment.



Chapter 6

Conclusion

Coulomb excitation RE experiments have been carried out at iThemba LABS. The $^{194}\text{Pt}(^{20}\text{Ne},^{20}\text{Ne}^*)^{194}\text{Pt}^*$ experiments were primarily aimed at bringing to closure the discrepancies between the predictions of current nuclear mean field models and the experimental determination of $Q_S(2_1^+)$ in ^{20}Ne [2] and to investigate whether or not the idea of nuclear clustering is realized in ^{20}Ne [16]. The second Coulomb excitation experiment is aimed at $Q_S(2_1^+)$ value in ^{40}Ar .

The role of this study in the above mentioned work is the development of sorting codes that can be used to perform the offline and online data analysis in Coulomb excitation experiments carried out using the AFRODITE array in conjunction with double sided silicon detectors. The details of the sorting codes that were used during the data analysis of the $^{194}\text{Pt}(^{20}\text{Ne},^{20}\text{Ne}^*)^{194}\text{Pt}^*$ and $^{208}\text{Pb}(^{40}\text{Ar},^{40}\text{Ar}^*)^{208}\text{Pb}^*$ measurements together with the results of the data analysis were presented.

In the case of the $^{208}\text{Pb}(^{40}\text{Ar},^{40}\text{Ar}^*)^{208}\text{Pb}^*$ experiment the $Q_S(2_1^+)$ value in ^{40}Ar will be determined by Mr Mokgolobotho as part of his MSc thesis. This work will provide the first experimental value of $Q_S(2_1^+)$ in ^{40}Ar at safe energies. The necessary equipment and electronics (S3 detectors, MPR32, MHV4, MSCF-16, DDAS, etc) to carry out these kind of particle- γ coincidence measurements were also put together during this work. The addition of a collimator plate in front of the S3 detector and a slit in front of the AFRODITE chamber was found to provide a reliable means to conduct such experiments when the target is placed behind the S3 detector. A solution to prevent the beam alignment problems when the S3 detector is placed downstream in front of the target is still being explored. The results of taking such precautions, together with ensuring that a synchronization signal is present

over the energy range of interest are evident in the data acquired during the $^{208}\text{Pb}(^{40}\text{Ar}, ^{40}\text{Ar}^*)^{208}\text{Pb}^*$. In particular, the addition of a collimator plate to the experimental setup carried out with the S3 detector, placed behind the target prevented damage to the S3 detector. This study shows that Coulomb excitation experiments can be carried out successfully at iThemba LABS if the experimental precautions discussed in this study are taken.

The task of creating the online and offline sorting codes, has been simplified by the creation of a program that can be used to generate similar sorting codes in the MTsort language [38] based on the explicit experimental parameters, such as the beam energy, the atomic masses, charge and mass numbers, excitation energies, together with the geometric details of the experiment. In addition, the program allows the user to select the conditions that should be included in the code. The program then outputs a sorting code that contains the commands to generate required spectra and impose the selected conditions used to reduce the background in the particle and γ -ray spectra. The resulting spectra can be used to get the counts in the γ -ray spectra for each ring of the S3 detector required as input to the *Gosia* code which can be used to determine the transitional and diagonal matrix elements required to determine $Q_S(2_1^+)$ values. The online sorting code allows monitoring of the incoming data during the experiments.

The program used to generate the online and offline sorting codes is currently limited to particle- γ coincidence experiments carried out using the AFRODITE array in conjunction with double sided silicon detectors. Some of the future improvements to the program used to generate these sorting codes, will include a Monte Carlo simulation of the energy loss and Doppler corrections similar to simulation used by Orce and collaborators [49] as well as possibly extending the code to other types of experiments carried out at iThemba LABS and other facilities.

Appendices



UNIVERSITY *of the*
WESTERN CAPE

Appendix A

Development of sort codes

A.1 Introduction

A C++ based multi-task program has been developed. This program is capable of generating sorting codes for particle- γ coincidence experiments. The resulting code is capable of sorting multi-parameter data online, as well as offline. The main aim of this program was to analyze the Coulomb excitation data involved in particle- γ coincidence measurements. The program is designed to generate the online and offline sorting codes in the MTsort language [38], which can be run in the MTsort software package [38], to generate the spectra that will be used for monitoring online Coulomb excitation measurements using the AFRODITE array in conjunction with the double sided silicon detectors. The details of how to use the program and the content of the resulting sorting codes are discussed in this appendix.

A.2 Installation

The program used to generate the sorting codes in the MTsort language [38] can be installed by executing *.install_s.sh* in the terminal. The program can be run by executing *.s_code* name of the input file.dat.

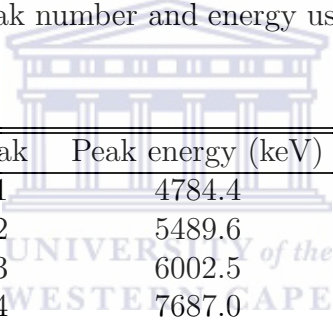
A.3 Sorting code options

The conditions explained in the data analysis section can be chosen by the user. When the *.s_code* (name of the input file).dat is executed, three options are presented and can be selected by entering the option number.

A.3.1 Online sorting code

The first option generates an online sorting code which can be used during the running of an experiment. The sort file generated by this option contains the commands to generate the particle and γ -ray energy spectra. This code includes the hit-patterns for the rings, sectors and HPGe crystals, time difference spectra between the rings and sectors, time difference spectra between the rings, sectors and clover detectors. This code also generates a 2D histograms that can be used to check the synchronization signal between the S3 detector and the HPGe clover detectors.

The remaining options requires the input of additional parameters at the terminal, namely the beam energy in MeV, the energy of 2_1^+ state of the beam in MeV, the beam and target atomic numbers, masses in amu, the target thickness in $\text{mg}\cdot\text{cm}^{-2}$, the density of the target in $\text{mg}\cdot\text{cm}^{-3}$, the SRIM value energy loss for the reaction. The α peak energies and peak numbers of the ^{226}Ra source that will be used for the two point calibration. The mapping between the source peak number and energy used in the sorting code is tabulated below.



Peak	Peak energy (keV)
1	4784.4
2	5489.6
3	6002.5
4	7687.0

Mapping between the ^{226}Ra source peak number and energy used in the sorting code.

The geometric parameters required are the distances from the center of the target position to the clover detectors and to the S3 detector, as well as the angular configuration of the S3 detector (forward or backward angles). The program uses these parameters in conjunction with the input file to do the energy loss and kinematics calculations and energy calibrations.

A.3.2 Offline sorting code for calibrations

The second option generates a sorting code similar to the first one, with the addition of two 2D histograms. The first one contains the ring and γ -ray time difference on the horizontal axis and the add-back γ -ray energy on the vertical axis. The second of these 2D histograms contains the sector and

γ -ray time difference on the horizontal axis and the add-back γ -ray energy on the vertical axis. These 2D histograms can be used to select 1) the ring and γ -ray time difference gates used to set up the particle- γ coincidence condition, 2) the ring and γ time difference gates that are used to subtract background in the γ -ray energy spectra, as well and 3) the projections of add-back γ -ray energy spectra corresponding to a particular ring and γ -ray time difference gate. The 2D histogram containing the sector and γ -ray time difference spectra plotted on the horizontal axis and the add-back γ -ray energy on the vertical axis can be used in the same way.

A.3.3 Sorting code optimized for Coulomb excitation

The third option allows the user to generate a sorting code which contains the commands used to implement the time and energy coincidence conditions between the HPGe crystals and the rings and sectors. The resulting sorting code generates the calibrated particle and γ -ray energy spectra for each clover detector crystal and each ring and sector, together with calibrated add-back γ -ray energy spectrum for all of the HPGe crystals, the hitpatterns for the rings, sectors and HPGe crystals, time difference spectra between the rings and sectors. This option also includes the commands to perform the Doppler correction of the γ -ray energies and generate the Doppler corrected γ -ray energy spectra for each clover detector crystal, the Doppler corrected add-back γ -ray energy spectrum as well as the Doppler corrected add-back γ -ray energy spectra for each of the rings.

Gates

The options for the energy difference and inelastic gates require the values of these gates from the user. If this option is selected the values in the `rgates.h` header file have to be changed from zero to the required values. This must be done prior to executing `.s_code`.

A.3.4 Clover detector geometry

The θ and ϕ angles to the center of the front face of each clover detector go in the `Cvg.h` file.

A.4 Input file

The input file contains the centroids of the rings and sectors which can be obtained by integrating the elastics peaks in the ring and sector particle energy spectra that have been generated using the sorting code obtained by selecting option two as well as the centroids of the α source that will be used for the calibration of the rings and sectors of the S3 detector and gains for each crystal of the clover detector. The format of the input file should be as follows

1	2	3	4	5	6	7	8	9	10
R_c	R_α	0	0	S_c	S_α	0	0	Ge_g	Ge_o

Table A.1: Input file format, first row corresponds to column number, second row corresponds to content of the columns.

- R_c : Centroids of the elastic peak of each ring.
- R_α : Centroids of the α source that will be used by two point calibration of each ring.
- Column of zeros, reserved for future use.
- Column of zeros, reserved for future use.
- S_c : Centroids of the elastic peak of each sector.
- S_α : Centroids of the α source that will be used by two point calibration of each sector.
- Column of zeros, reserved for future use.
- Column of zeros, reserved for future use.
- Ge_g : Gains for each of the clover crystals.
- Ge_o : Offset for each of the clover crystals.

These are floating point numbers correct to two decimal places, each of the columns should have 36 values if nine clover detectors are used and 32 if eight clover detectors are used. The variables that are not used should be entered as zero. In addition, Ge_g and Ge_o should be entered per crystal starting from crystal a to d, that is, the first nine (eight) values correspond to crystal a, the next nine (eight) values correspond to crystal b,.. etc, in numerical order. An example input file has been included in appendix A.7.

A.5 Data files

The location of the data files that will be used in the sorting codes have to be inserted in the **RUNFILES* section of the sorting code, the path to the data files should be added as *DISC* path, as an example, the path to a data file in the home directory is added as *DISC* path.

A.6 Examples of generated sortfiles

Figure ?? shows the execution order of the programs used to generate the sortfiles. Here, the *n2.h*, *k2.h*, *rgates.h* and *Cvg.h* header are used in the main source code, *s_code.cpp*, which is compiled to generate the *s_code* executable file which can then be used in conjunction with the input file to generate sortfiles.

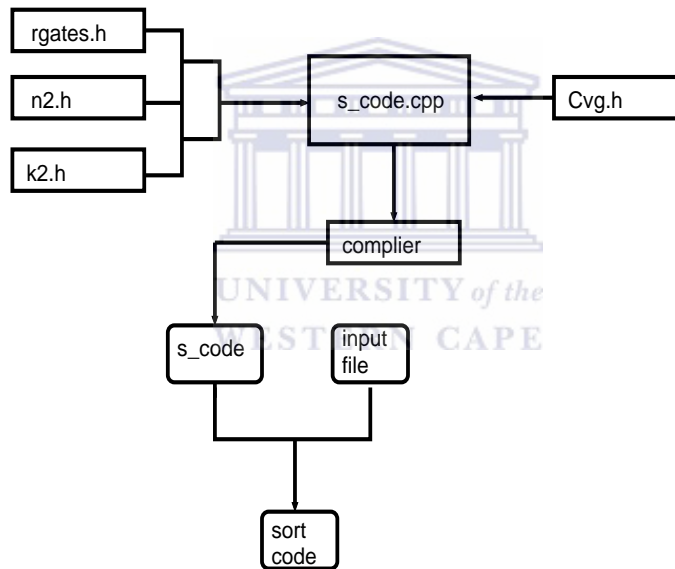


Figure A.1: Execution order of programs used to generate the sortfiles

The following sortfiles are examples of the sorting codes generated by the program.

A.6.1 Online sorting code (option 1 example)

*formats

```
clover[1:8](e1, e2, e3, e4, x1, x2, x3, x4)
sect[21:52](e1, x1)
ring[53:77](e1, x1)
```

```
*data
```

```
longlong tg = 0
longlong ts = 0
longlong tr = 0
longlong td = 0
longlong tga = 0
longlong tgb = 0
longlong tgc = 0
longlong tgd = 0
longlong tdr = 0
longlong tds = 0
longlong tss1 = 0
longlong trr1 = 0
longlong tdgr = 0
longlong tdgs = 0
longlong tdddd = 0
```



```
longlong tdbg_01s1=0
```

```
longlong tdbg_01s2=0
```

```
valuearray eclov[1:8]
0 0 0 0 0 0 0 0
```

```
valuearray tg1[1:8]
0 0 0 0 0 0 0 0
```

```
valuearray energyg1[1:8]
```

0 0 0 0 0 0 0 0

valuearray tg2[1:8]

0 0 0 0 0 0 0 0

valuearray energyg2[1:8]

0 0 0 0 0 0 0 0

valuearray tg3[1:8]

0 0 0 0 0 0 0 0

valuearray energyg3[1:8]

0 0 0 0 0 0 0 0

valuearray tg4[1:8]

0 0 0 0 0 0 0 0

valuearray energyg4[1:8]

0 0 0 0 0 0 0 0



valuearray sum[1:8]

0 0 0 0 0 0 0 0

valuearray energyr[1:24]

0 0 0 0 0 0 0 0

0 0 0 0 0 0 0 0

0 0 0 0 0 0 0 0

valuearray energys[1:32]

0 0 0 0 0 0 0 0

0 0 0 0 0 0 0 0

0 0 0 0 0 0 0 0

0 0 0 0 0 0 0 0

```
valuearray tr1[1:24]
0 0 0 0 0 0 0 0
0 0 0 0 0 0 0 0
0 0 0 0 0 0 0 0
```

```
valuearray ts1[1:32]
0 0 0 0 0 0 0 0
0 0 0 0 0 0 0 0
0 0 0 0 0 0 0 0
0 0 0 0 0 0 0 0
```

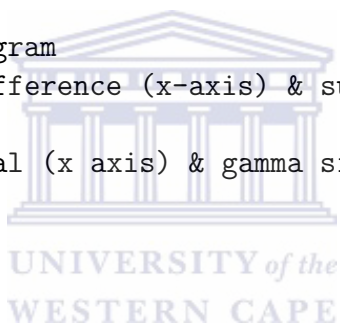
```
valuearray hu[1:2]
0 0
```

```
*spectra
!!!!!!!!!!!!!!!!!!!!!!!!!!!!!!!!!!!!!!!!!!!!!!!!!!!!!!!!!!!!!!!!!!!!!!
!rclovera: gamma spectra for crystal a
!rcloverb: gamma spectra for crystal b
!rcloverc: gamma spectra for crystal c
!rcloverd: gamma spectra for crystal d
!sectors: particle energy spectra for sectors
!ring:particle energy spectra for sectors
!hitpatg: hitpattern for Ge detectors
!hitpatr: hitpattern for rings
!hitpats: hitpattern for sectors
!timesi: ring and time difference spectrum
!timeg1: ring and gamma time difference spectrum
!timeg2: sector and gamma time difference spectrum
!!!!!!!!!!!!!!!!!!!!!!!!!!!!!!!!!!!!!!!!!!!!!!!!!!!!!!!!!!!!!!!!!!!!!!
rclovera[1:8] 16384
rcloverb[1:8] 16384
rcloverc[1:8] 16384
rcloverd[1:8] 16384
sectors[1:32] 65536
rings[1:24] 65536
hitpatg 108 32
```

```

hitpatr 108 32
hitpats 64 32
timesi 4096 32
timeg1 4096 32
timeg2 4096 32
!particle-gamma time difference spectra for each crystal
timegra[1:8] 4096 32
timegsa[1:8] 4096 32
timegrb[1:8] 4096 32
timegsb[1:8] 4096 32
timegrc[1:8] 4096 32
timegsc[1:8] 4096 32
timegrd[1:8] 4096 32
timegsd[1:8] 4096 32
!2D ring-gamma histogram
!(ring-gamma time difference (x-axis) & sum of all clover energies (y-axis))
pgr_mat 2048 2d
!2D sector-gamma histogram
!(sector-gamma time difference (x-axis) & sum of all clover energies (y-axis))
pgs_mat 2048 2d
!sync_mat: 2d (si signal (x axis) & gamma signal (y axis)) histogram
syncmat 1024 2d

```



*commands

```

doloop i from 1 to 32 step +1
{
  energys(i) = 0
  ts1(i) = 0
}

```

```

doloop i from 1 to 24 step +1
{
  energyr(i) = 0
  tr1(i) = 0
}

```

```

doloop i from 1 to 8 step +1
{

```

```
sum(i)=0
energyg1(i)=0
tg1(i)=0
energyg2(i)=0
tg2(i)=0
energyg3(i)=0
tg3(i)=0
energyg4(i)=0
tg4(i)=0
}
```

```
ns = 0
nr = 0
nga = 0
ngb = 0
ngc = 0
ngd = 0
```



```
createlist glist from clover
createlist slist from sect
createlist rlist from ring
doloop i from 1 to 2 step +1
{
hu(i)=0
}
```

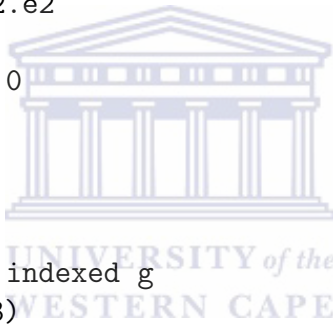
```
doloop i from 1 to 8 step +1
{
eclov(i)=0
}
```

```
loopif $g1=glist.e1 gt 0
{
```

```

g = group($g1)
inc hitpatg(g)
energyg1(g)=$g1.e1
inc rclovera($g1.e1) indexed g
tg=timestampof($g1.e1)
tg1(g) = timestampof($g1.e1)
sum(g) = sum(g) + $g1.e1
}
loopif $g2=glist.e2 gt 0
{
g = group($g2)
inc hitpatg(g)
energyg2(g)=$g2.e2
inc rcloverb($g2.e2) indexed g
tg=timestampof($g2.e2)
tg2(g) = timestampof($g2.e2)
sum(g) = sum(g) + $g2.e2
}
loopif $g3=glist.e3 gt 0
{
g = group($g3)
inc hitpatg(g)
energyg3(g)=$g3.e3
inc rcloverc($g3.e3) indexed g
tg=timestampof($g3.e3)
tg3(g) = timestampof($g3.e3)
sum(g) = sum(g) + $g3.e3
}
loopif $g4=glist.e4 gt 0
{
g = group($g4)
inc hitpatg(g)
energyg4(g)=$g4.e4
inc rcloverd($g4.e4) indexed g
tg=timestampof($g4.e4)
tg4(g) = timestampof($g4.e4)
sum(g) = sum(g) + $g4.e4
}
loopif $r=rlist.e1 gt 0
{
g = group($r) - 52

```



```

inc hitpatr(g)
energyr(g) = $r.e1
inc rings($r.e1) indexed g
tr = timestampof($r.e1)
tr1(g) = timestampof($r.e1)
trr1 = tr1(g)
nr=nr + 1
}

```

```

loopif $s=slist.e1 gt 0
{
g = group($s) - 20
inc hitpats(g)
energys(g) = $s.e1
inc sectors($s.e1) indexed g
ts = timestampof($s.e1)
ts1(g) = timestampof($s.e1)
tss1 = ts1(g)
ns=ns + 1
}

```



```

td=(ts-tr)+1024
inc timesi(td)

```

```

td=(tg-tr)+1024
inc timeg1(td)

```

```

td=(tg-ts)+1024
inc timeg2(td)

```

```

hu(1)=tr
hu(2)=ts
doloop r from 1 to 2 step +1
{
h = hu(r)
doloop k from 1 to 8 step +1
{
h4 = tg1(k)
if h ne 0

```

```
{
if h4 ne 0
{
td = (h-h4) +1024
if r eq 1
{
inc timegra(td) indexed k
}
else if r eq 2
{
inc timegsa(td) indexed k
}
}
h4 = tg2(k)
if h4 ne 0
{
td = (h-h4) +1024
if r eq 1
{
inc timegrb(td) indexed k
}
else if r eq 2
{
inc timegsb(td) indexed k
}
}
h4 = tg3(k)
if h4 ne 0
{
td = (h-h4) +1024
if r eq 1
{
inc timegrc(td) indexed k
}
else if r eq 2
{
inc timegsc(td) indexed k
}
}
h4 = tg4(k)
if h4 ne 0
```



```

{
td = (h-h4) +1024
if r eq 1
{
inc timegrd(td) indexed k
}
else if r eq 2
{
inc timegsd(td) indexed k
}
}
}
}
}

```

```

ebg_0s=0
doloop v from 1 to 8 step +1
{
eclov(v)=energyg1(v) + energyg2(v) + energyg3(v) + energyg4(v)
ebg_0s=eclov(v)
tdbg_01s1=(tg-tr) +1024
tdbg_01s2=(tg-ts) +1024
if ebg_0s gt 0
{
inc pgr_mat(tdbg_01s1,ebg_0s)
inc pgs_mat(tdbg_01s2,ebg_0s)
}
}
inc syncmat(ring[77].e1/4, clover[1].e1/4)
*runfiles

```

*finish

A.6.2 Offline sorting code for calibrations (option 2 example)

```

*formats
clover[1:8](e1, e2, e3, e4, x1, x2, x3, x4)
sect[21:52](e1, x1)

```

ring[53:77](e1, x1)

*data

Gainarray SegA

1 (2.02092 0.408275 0.000)
2 (2.61341 0.55439 0.000)
3 (0.73663 0.38937 0.000)
4 (0.71045 0.38499 0.000)
5 (1.2227 0.36788 0.000)
6 (1.45362 0.37296 0.000)
7 (1.86504 0.5693 0.000)
8 (0.06463 0.36838 0.000)

Gainarray SegB

1 (1.85431 0.38056 0.000)
2 (-0.5197 0.53791 0.000)
3 (-0.041 0.37137 0.000)
4 (1.15026 0.3937 0.000)
5 (2.05163 0.37744 0.000)
6 (1.38623 0.37284 0.000)
7 (1.15731 0.54095 0.000)
8 (0.60726 0.38316 0.000)



Gainarray SegC

1 (4.80752 0.407212 0.000)
2 (0.584231 0.372242 0.000)
3 (0.685853 0.46781 0.000)
4 (0.182871 0.669081 0.000)
5 (1.67886 0.359602 0.000)
6 (2.1086 0.36313 0.000)
7 (2.50293 0.354192 0.000)
8 (0.50562 0.590173 0.000)

Gainarray SegD

1 (1.66992 0.422171 0.000)
2 (0.86854 0.422403 0.000)
3 (1.74068 0.39989 0.000)

4 (0.902344 0.377175 0.000)
5 (1.75371 0.36044 0.000)
6 (1.26998 0.362504 0.000)
7 (1.67919 0.524756 0.000)
8 (0.46295 0.361294 0.000)

Gainarray ring

53 (-574.68 2.52 0.000)
54 (-561.79 2.61 0.000)
55 (-550.16 2.53 0.000)
56 (-535.20 2.46 0.000)
57 (-524.69 2.45 0.000)
58 (-518.26 2.51 0.000)
59 (-505.11 2.49 0.000)
60 (-495.88 2.48 0.000)
61 (-487.50 2.39 0.000)
62 (-432.81 2.36 0.000)
63 (-479.49 2.44 0.000)
64 (-521.38 2.43 0.000)
65 (-408.68 2.30 0.000)
66 (-471.17 2.39 0.000)
67 (-462.13 2.35 0.000)
68 (-423.11 2.31 0.000)
69 (-423.06 2.33 0.000)
70 (-405.60 2.33 0.000)
71 (-430.72 2.37 0.000)
72 (-415.45 2.34 0.000)
73 (-422.13 2.34 0.000)
74 (-400.27 2.31 0.000)
75 (-442.10 2.33 0.000)
76 (-368.48 2.24 0.000)
77 (0.00 0.00 0.000)



Gainarray sect

21 (-507.63 0.86 0.000)
22 (-514.35 0.89 0.000)
23 (-513.33 0.90 0.000)
24 (-515.94 0.86 0.000)
25 (-519.71 0.87 0.000)

26 (-530.08 0.89 0.000)
27 (-528.78 0.87 0.000)
28 (-516.79 0.86 0.000)
29 (-524.92 0.87 0.000)
30 (-502.81 0.87 0.000)
31 (-530.65 0.90 0.000)
32 (-635.04 0.92 0.000)
33 (-473.81 0.86 0.000)
34 (-580.51 0.91 0.000)
35 (-526.96 0.89 0.000)
36 (-602.75 0.92 0.000)
37 (-528.43 0.88 0.000)
38 (-557.42 0.90 0.000)
39 (-555.37 0.89 0.000)
40 (-536.48 0.89 0.000)
41 (-546.12 0.90 0.000)
42 (-545.11 0.90 0.000)
43 (-540.99 0.89 0.000)
44 (-539.24 0.89 0.000)
45 (-520.40 0.86 0.000)
46 (-528.43 0.88 0.000)
47 (-526.36 0.89 0.000)
48 (-518.39 0.87 0.000)
49 (-519.68 0.87 0.000)
50 (-515.88 0.87 0.000)
51 (-515.59 0.90 0.000)
52 (0.00 0.00 0.000)



longlong tg = 0
longlong ts = 0
longlong tr = 0
longlong td = 0
longlong tga = 0
longlong tgb = 0
longlong tgc = 0
longlong tgd = 0
longlong tdr = 0
longlong tds = 0
longlong tss1 = 0
longlong trr1 = 0

```
longlong tdgr = 0
longlong tdgs = 0
longlong tdddd = 0
```

```
valuearray tg1[1:8]
0 0 0 0 0 0 0 0
```

```
valuearray energyg1[1:8]
0 0 0 0 0 0 0 0
```

```
valuearray tg2[1:8]
0 0 0 0 0 0 0 0
```

```
valuearray energyg2[1:8]
0 0 0 0 0 0 0 0
```

```
valuearray tg3[1:8]
0 0 0 0 0 0 0 0
```

```
valuearray energyg3[1:8]
0 0 0 0 0 0 0 0
```

```
valuearray tg4[1:8]
0 0 0 0 0 0 0 0
```

```
valuearray energyg4[1:8]
0 0 0 0 0 0 0 0
```

```
longlong tdbg_01s1=0
```

```
longlong tdbg_01s2=0
```

```
valuearray eclov[1:8]
0 0 0 0 0 0 0 0
```

```
valuearray sum[1:8]
0 0 0 0 0 0 0 0
```



```
valuearray energyr[1:24]
0 0 0 0 0 0 0 0
0 0 0 0 0 0 0 0
0 0 0 0 0 0 0 0
```

```
valuearray energys[1:32]
0 0 0 0 0 0 0 0
0 0 0 0 0 0 0 0
0 0 0 0 0 0 0 0
0 0 0 0 0 0 0 0
```

```
valuearray tr1[1:24]
0 0 0 0 0 0 0 0
0 0 0 0 0 0 0 0
0 0 0 0 0 0 0 0
```

```
valuearray ts1[1:32]
0 0 0 0 0 0 0 0
0 0 0 0 0 0 0 0
0 0 0 0 0 0 0 0
0 0 0 0 0 0 0 0
```

```
valuearray hu[1:2]
0 0
```



```
*spectra
!!!!!!!!!!!!!!!!!!!!!!!!!!!!!!!!!!!!!!!!!!!!!!!!!!!!!!!!!!!!!!!!!!!!!!!!!!!!!!
!rclovera: gamma spectra for crystal a
!rcloverb: gamma spectra for crystal b
!rcloverc: gamma spectra for crystal c
!rcloverd: gamma spectra for crystal d
!sectors: particle energy spectra for sectors
!ring:particle energy spectra for sectors
!hitpatg: hitpattern for Ge detectors
!hitpatr: hitpattern for rings
!hitpats: hitpattern for sectors
!timesi: ring and time difference spectrum
!timeg1: ring and gamma time difference spectrum
```

```

!timeg2: sector and gamma time difference spectrum
!!!!!!!!!!!!!!!!!!!!!!!!!!!!!!!!!!!!!!!!!!!!!!!!!!!!!!!!!!!!!!!!!!!!!!!!!!!!!!
rclovera[1:8] 16384
rcloverb[1:8] 16384
rcloverc[1:8] 16384
rcloverd[1:8] 16384
sectors[1:32] 65536
rings[1:24] 65536
hitpatg 108 32
hitpatr 108 32
hitpats 64 32
timesi 4096 32
timeg1 4096 32
timeg2 4096 32
!particle-gamma time difference spectra for each crystal
timegra[1:8] 4096 32
timegsa[1:8] 4096 32
timegrb[1:8] 4096 32
timegsb[1:8] 4096 32
timegrc[1:8] 4096 32
timegsc[1:8] 4096 32
timegrd[1:8] 4096 32
timegsd[1:8] 4096 32
!2D ring-gamma histogram
!(ring-gamma time difference (x-axis) & sum of all clover energies (y-axis))
pgr_mat 1024 2d
!2D sector-gamma histogram
!(sector-gamma time difference (x-axis) & sum of all clover energies (y-axis))
pgs_mat 1024 2d

*commands

doloop i from 1 to 32 step +1
{
  energys(i) = 0
  ts1(i) = 0
}

doloop i from 1 to 24 step +1

```



```
{
  energyr(i) = 0
  tr1(i) = 0
}
```

```
doloop i from 1 to 8 step +1
{
  sum(i)=0
  energyg1(i)=0
  tg1(i)=0
  energyg2(i)=0
  tg2(i)=0
  energyg3(i)=0
  tg3(i)=0
  energyg4(i)=0
  tg4(i)=0
}
```

```
ns = 0
nr = 0
nga = 0
ngb = 0
ngc = 0
ngd = 0
```



```
doloop i from 1 to 2 step +1
{
  hu(i)=0
}
doloop i from 1 to 8 step +1
{
  eclov(i)=0
}
createlist glist from clover
createlist slist from sect
```

```

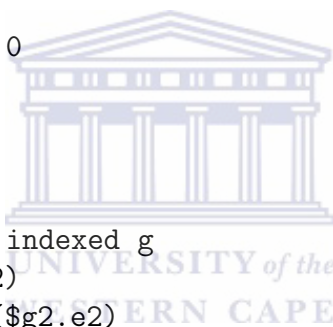
createlist rlist from ring
gain glist.e1 segA factor 1.00
gain glist.e2 segB factor 1.00
gain glist.e3 segC factor 1.00
gain glist.e4 segD factor 1.00

```

```

loopif $g1=glist.e1 gt 0
{
  g = group($g1)
  inc hitpatg(g)
  energyg1(g)=$g1.e1
  inc rclovera($g1.e1) indexed g
  tg=timestampof($g1.e1)
  tg1(g) = timestampof($g1.e1)
  sum(g) = sum(g) + $g1.e1
}
loopif $g2=glist.e2 gt 0
{
  g = group($g2)
  inc hitpatg(g)
  energyg2(g)=$g2.e2
  inc rcloverb($g2.e2) indexed g
  tg=timestampof($g2.e2)
  tg2(g) = timestampof($g2.e2)
  sum(g) = sum(g) + $g2.e2
}
loopif $g3=glist.e3 gt 0
{
  g = group($g3)
  inc hitpatg(g)
  energyg3(g)=$g3.e3
  inc rcloverc($g3.e3) indexed g
  tg=timestampof($g3.e3)
  tg3(g) = timestampof($g3.e3)
  sum(g) = sum(g) + $g3.e3
}
loopif $g4=glist.e4 gt 0
{
  g = group($g4)
  inc hitpatg(g)

```



```
energyg4(g)=$g4.e4
inc rcloverd($g4.e4) indexed g
tg=timestampof($g4.e4)
tg4(g) = timestampof($g4.e4)
sum(g) = sum(g) + $g4.e4
}
```

```
gain slist.e1 sect factor 1.00
gain rlist.e1 ring factor 1.00
```

```
loopif $r=rlist.e1 gt 0
{
  g = group($r) - 52
  inc hitpatr(g)
  energyr(g) = $r.e1
  inc rings($r.e1) indexed g
  tr = timestampof($r.e1)
  tr1(g) = timestampof($r.e1)
  trr1 = tr1(g)
  nr=nr + 1
}
```



```
loopif $s=slist.e1 gt 0
{
  g = group($s) - 20
  inc hitpats(g)
  energys(g) = $s.e1
  inc sectors($s.e1) indexed g
  ts = timestampof($s.e1)
  ts1(g) = timestampof($s.e1)
  tss1 = ts1(g)
  ns=ns + 1
}
```

```
td=(ts-tr)+1024
inc timesi(td)
```

```

td=(tg-tr)+1024
inc timeg1(td)

td=(tg-ts)+1024
inc timeg2(td)

hu(1)=tr
hu(2)=ts
doloop r from 1 to 2 step +1
{
  h = hu(r)
  doloop k from 1 to 8 step +1
  {
    h4 = tg1(k)
    if h ne 0
    {
      if h4 ne 0
      {
        td = (h-h4) +1024
        if r eq 1
        {
          inc timegra(td) indexed k
        }
        else if r eq 2
        {
          inc timegsa(td) indexed k
        }
      }
      h4 = tg2(k)
      if h4 ne 0
      {
        td = (h-h4) +1024
        if r eq 1
        {
          inc timegrb(td) indexed k
        }
        else if r eq 2
        {
          inc timegsb(td) indexed k
        }
      }
    }
  }
}

```



```

    h4 = tg3(k)
    if h4 ne 0
    {
    td = (h-h4) +1024
    if r eq 1
    {
    inc timegrc(td) indexed k
    }
    else if r eq 2
    {
    inc timegsc(td) indexed k
    }
    }
    h4 = tg4(k)
    if h4 ne 0
    {
    td = (h-h4) +1024
    if r eq 1
    {
    inc timegrd(td) indexed k
    }
    else if r eq 2
    {
    inc timegsd(td) indexed k
    }
    }
    }
    }
    }

```



```

    ebg_0s=0
    doloop v from 1 to 8 step +1
    {
    eclov(v)=energyg1(v) + energyg2(v) + energyg3(v) + energyg4(v)
    ebg_0s=eclov(v)
    tdbg_01s1=(tg-tr) +1024
    tdbg_01s2=(tg-ts) +1024
    if ebg_0s gt 0
    {
    inc pgr_mat(tdbg_01s1,ebg_0s)
    }
    }

```

```
inc pgr_mat(tdbg_01s2,ebg_0s)
}
}
*runfiles
```

```
*finish
```

A.6.3 Offline sorting code (basic option 3 example)

```
*formats
clover[1:8](e1, e2, e3, e4, x1, x2, x3, x4)
sect[21:52](e1, x1)
ring[53:77](e1, x1)
```

```
*data
```

```
Gainarray SegA
```

```
1 (2.02092 0.408275 0.000)
2 (2.61341 0.55439 0.000)
3 (0.73663 0.38937 0.000)
4 (0.71045 0.38499 0.000)
5 (1.2227 0.36788 0.000)
6 (1.45362 0.37296 0.000)
7 (1.86504 0.5693 0.000)
8 (0.06463 0.36838 0.000)
```

```
Gainarray SegB
```

```
1 (1.85431 0.38056 0.000)
2 (-0.5197 0.53791 0.000)
3 (-0.041 0.37137 0.000)
4 (1.15026 0.3937 0.000)
5 (2.05163 0.37744 0.000)
6 (1.38623 0.37284 0.000)
7 (1.15731 0.54095 0.000)
8 (0.60726 0.38316 0.000)
```

```
Gainarray SegC
```

```
1 (4.80752 0.407212 0.000)
```

2 (0.584231 0.372242 0.000)
3 (0.685853 0.46781 0.000)
4 (0.182871 0.669081 0.000)
5 (1.67886 0.359602 0.000)
6 (2.1086 0.36313 0.000)
7 (2.50293 0.354192 0.000)
8 (0.50562 0.590173 0.000)

Gainarray SegD

1 (1.66992 0.422171 0.000)
2 (0.86854 0.422403 0.000)
3 (1.74068 0.39989 0.000)
4 (0.902344 0.377175 0.000)
5 (1.75371 0.36044 0.000)
6 (1.26998 0.362504 0.000)
7 (1.67919 0.524756 0.000)
8 (0.46295 0.361294 0.000)

Gainarray ring

53 (-574.68 2.52 0.000)
54 (-561.79 2.61 0.000)
55 (-550.16 2.53 0.000)
56 (-535.20 2.46 0.000)
57 (-524.69 2.45 0.000)
58 (-518.26 2.51 0.000)
59 (-505.11 2.49 0.000)
60 (-495.88 2.48 0.000)
61 (-487.50 2.39 0.000)
62 (-432.81 2.36 0.000)
63 (-479.49 2.44 0.000)
64 (-521.38 2.43 0.000)
65 (-408.68 2.30 0.000)
66 (-471.17 2.39 0.000)
67 (-462.13 2.35 0.000)
68 (-423.11 2.31 0.000)
69 (-423.06 2.33 0.000)
70 (-405.60 2.33 0.000)
71 (-430.72 2.37 0.000)
72 (-415.45 2.34 0.000)



APPENDIX A. DEVELOPMENT OF SORT CODES

73 (-422.13 2.34 0.000)
74 (-400.27 2.31 0.000)
75 (-442.10 2.33 0.000)
76 (-368.48 2.24 0.000)
77 (0.00 0.00 0.000)

Gainarray sect

21 (-507.63 0.86 0.000)
22 (-514.35 0.89 0.000)
23 (-513.33 0.90 0.000)
24 (-515.94 0.86 0.000)
25 (-519.71 0.87 0.000)
26 (-530.08 0.89 0.000)
27 (-528.78 0.87 0.000)
28 (-516.79 0.86 0.000)
29 (-524.92 0.87 0.000)
30 (-502.81 0.87 0.000)
31 (-530.65 0.90 0.000)
32 (-635.04 0.92 0.000)
33 (-473.81 0.86 0.000)
34 (-580.51 0.91 0.000)
35 (-526.96 0.89 0.000)
36 (-602.75 0.92 0.000)
37 (-528.43 0.88 0.000)
38 (-557.42 0.90 0.000)
39 (-555.37 0.89 0.000)
40 (-536.48 0.89 0.000)
41 (-546.12 0.90 0.000)
42 (-545.11 0.90 0.000)
43 (-540.99 0.89 0.000)
44 (-539.24 0.89 0.000)
45 (-520.40 0.86 0.000)
46 (-528.43 0.88 0.000)
47 (-526.36 0.89 0.000)
48 (-518.39 0.87 0.000)
49 (-519.68 0.87 0.000)
50 (-515.88 0.87 0.000)
51 (-515.59 0.90 0.000)
52 (0.00 0.00 0.000)



```
longlong tg = 0
longlong ts = 0
longlong tr = 0
longlong td = 0
longlong tga = 0
longlong tgb = 0
longlong tgc = 0
longlong tgd = 0
longlong tdr = 0
longlong tds = 0
longlong tss1 = 0
longlong trr1 = 0
longlong tdgr = 0
longlong tdgs = 0
longlong tdddd = 0
```

```
valuearray tg1[1:8]
0 0 0 0 0 0 0 0
```

```
valuearray energyg1[1:8]
0 0 0 0 0 0 0 0
```

```
valuearray tg2[1:8]
0 0 0 0 0 0 0 0
```

```
valuearray energyg2[1:8]
0 0 0 0 0 0 0 0
```

```
valuearray tg3[1:8]
0 0 0 0 0 0 0 0
```

```
valuearray energyg3[1:8]
0 0 0 0 0 0 0 0
```

```
valuearray tg4[1:8]
```



0 0 0 0 0 0 0 0

valuearray energyg4[1:8]
0 0 0 0 0 0 0 0

valuearray sum[1:8]
0 0 0 0 0 0 0 0

valuearray nrr[1:24]
0 0 0 0 0 0 0 0
0 0 0 0 0 0 0 0
0 0 0 0 0 0 0 0

valuearray nss[1:32]
0 0 0 0 0 0 0 0
0 0 0 0 0 0 0 0
0 0 0 0 0 0 0 0
0 0 0 0 0 0 0 0



valuearray energyr[1:24]
0 0 0 0 0 0 0 0
0 0 0 0 0 0 0 0
0 0 0 0 0 0 0 0

valuearray energys[1:32]
0 0 0 0 0 0 0 0
0 0 0 0 0 0 0 0
0 0 0 0 0 0 0 0
0 0 0 0 0 0 0 0

valuearray tr1[1:24]
0 0 0 0 0 0 0 0
0 0 0 0 0 0 0 0
0 0 0 0 0 0 0 0

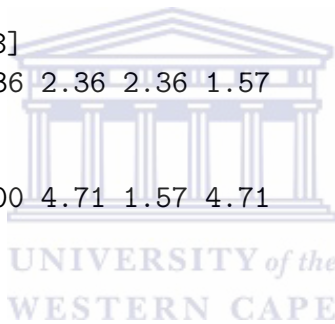
```
valuearray ts1[1:32]
0 0 0 0 0 0 0 0
0 0 0 0 0 0 0 0
0 0 0 0 0 0 0 0
0 0 0 0 0 0 0 0
```

```
float pi = 3.141592654
float d_target2ge = 19.60
float d_target2s3 = -3.00
float A
float B
float thetag0
float phig0
float thetab
```

```
valuearray ge_theta[1:8]
2.36 1.57 1.57 1.57 2.36 2.36 2.36 1.57
```

```
valuearray ge_phi[1:8]
3.14 0.79 3.93 5.50 0.00 4.71 1.57 4.71
```

```
float xa
float xbb
float xc
float xd
float xb
float caax
float ya
float ybb
float yc
float yd
float yb
float cabx
float za
float zbb
float zc
float zd
float zb
float cacx
```



```
float  caa
float  cab
float  cac
float  cad
float  phib
float  cadx
float  x0a
float  x0b
float  x0c
float  x0d
float  y0a
float  y0b
float  y0c
float  y0d
float  z0a
float  z0b
float  z0c
float  z0d
valuearray  sumdop[1:8]
0 0 0 0 0 0 0 0

valuearray  sumdopx[1:8]
0 0 0 0 0 0 0 0

valuearray  sumnodop[1:8]
0 0 0 0 0 0 0 0

valuearray  sumnodopx[1:8]
0 0 0 0 0 0 0 0

valuearray  x_cent[1:8]
0 0 0 0 0 0 0 0

valuearray  y_cent[1:8]
0 0 0 0 0 0 0 0

valuearray  z_cent[1:8]
0 0 0 0 0 0 0 0

valuearray  e11ca[1:8]
0 0 0 0 0 0 0 0
```



valuearray e11cb[1:8]
0 0 0 0 0 0 0 0

valuearray e11cc[1:8]
0 0 0 0 0 0 0 0

valuearray e11cd[1:8]
0 0 0 0 0 0 0 0

valuearray x_1[1:8]
0 0 0 0 0 0 0 0

valuearray x_2[1:8]
0 0 0 0 0 0 0 0

valuearray x_3[1:8]
0 0 0 0 0 0 0 0

valuearray x_4[1:8]
0 0 0 0 0 0 0 0

valuearray y_1[1:8]
0 0 0 0 0 0 0 0

valuearray y_2[1:8]
0 0 0 0 0 0 0 0

valuearray y_3[1:8]
0 0 0 0 0 0 0 0

valuearray y_4[1:8]
0 0 0 0 0 0 0 0

valuearray z_1[1:8]
0 0 0 0 0 0 0 0

valuearray z_2[1:8]
0 0 0 0 0 0 0 0

valuearray z_3[1:8]



0 0 0 0 0 0 0 0

valuearray z_4[1:8]

0 0 0 0 0 0 0 0

valuearray e11cax[1:8]

0 0 0 0 0 0 0 0

valuearray e11cbx[1:8]

0 0 0 0 0 0 0 0

valuearray e11ccx[1:8]

0 0 0 0 0 0 0 0

valuearray e11cdx[1:8]

0 0 0 0 0 0 0 0

valuearray angdis[1:24]

2.76 2.74 2.71 2.68 2.66 2.63

2.61 2.58 2.56 2.54 2.51 2.49

2.47 2.45 2.43 2.41 2.40 2.38

2.36 2.35 2.33 2.31 2.30 2.29

valuearray beta[1:24]

0.07 0.07 0.07 0.07 0.07 0.07

0.07 0.07 0.07 0.07 0.07 0.07

0.07 0.07 0.07 0.07 0.07 0.07

0.07 0.07 0.07 0.07 0.07 0.07

valuearray sec_phi[1:32]

3.14159 3.33794 3.53429 3.73064 3.92699 4.12334 4.31969 4.51604

4.71239 5.10509 5.30144 5.49779 5.69414 5.89049 6.08684 6.28319

0.19635 0.392699 0.589049 0.785398 0.981748 1.1781 1.37445 1.5708

1.76715 1.9635 1.9635 2.15984 2.35619 2.55254 2.74889 2.94524

valuearray phi_tmp[1:32]

0 0 0 0 0 0 0 0

0 0 0 0 0 0 0 0

```
0 0 0 0 0 0 0 0
0 0 0 0 0 0 0 0
```

```
valuearray sumdr[1:24]
0 0 0 0 0 0 0 0
0 0 0 0 0 0 0 0
0 0 0 0 0 0 0 0
```

```
valuearray sumndr[1:24]
0 0 0 0 0 0 0 0
0 0 0 0 0 0 0 0
0 0 0 0 0 0 0 0
```

```
valuearray sumdrab[1:24]
0 0 0 0 0 0 0 0
0 0 0 0 0 0 0 0
0 0 0 0 0 0 0 0
```

```
valuearray sumndrab[1:24]
0 0 0 0 0 0 0 0
0 0 0 0 0 0 0 0
0 0 0 0 0 0 0 0
```

```
valuearray eegdop[1:9]
0 0 0 0 0 0 0 0 0
```

```
valuearray crys_a_theta[1:8]
2.27 1.48 1.48 1.48 2.27 2.27 2.27 1.48
```

```
valuearray crys_b_theta[1:8]
2.45 1.66 1.66 1.66 2.45 2.45 2.45 1.66
```

```
valuearray crys_c_theta[1:8]
2.45 1.66 1.66 1.66 2.45 2.45 2.45 1.66
```

```
valuearray crys_d_theta[1:8]
2.27 1.48 1.48 1.48 2.27 2.27 2.27 1.48
```

```
valuearray crys_a_phi[1:8]
3.23 0.87 4.02 5.59 0.09 4.80 1.66 4.80
```

```
valuearray crys_b_phi[1:8]
3.23 0.87 4.02 5.59 0.09 4.80 1.66 4.80
```

```
valuearray crys_c_phi[1:8]
3.05 0.70 3.84 5.41 3.05 4.62 1.48 4.62
```

```
valuearray crys_d_phi[1:8]
3.05 0.70 3.84 5.41 3.05 4.62 1.48 4.62
```



```

*spectra
!!!!!!!!!!!!!!!!!!!!!!!!!!!!!!!!!!!!!!!!!!!!!!!!!!!!!!!!!!!!!!!!!!!!!!!!!!!!!!
!rclovera: gamma spectra for crystal a
!rcloverb: gamma spectra for crystal b
!rcloverc: gamma spectra for crystal c
!rcloverd: gamma spectra for crystal d
!sectors: particle energy spectra for sectors
!ring:particle energy spectra for sectors
!hitpatg: hitpattern for Ge detectors
!hitpatr: hitpattern for rings
!hitpats: hitpattern for sectors
!timesi: ring and time difference spectrum
!timeg1: ring and gamma time difference spectrum
!timeg2: sector and gamma time difference spectrum
!!!!!!!!!!!!!!!!!!!!!!!!!!!!!!!!!!!!!!!!!!!!!!!!!!!!!!!!!!!!!!!!!!!!!!!!!!!!!!
rclovera[1:8] 16384
rcloverb[1:8] 16384
rcloverc[1:8] 16384
rcloverd[1:8] 16384
sectors[1:32] 65536
rings[1:24] 65536
hitpatg 108 32
hitpatr 108 32
hitpats 64 32
timesi 4096 32
timeg1 4096 32
timeg2 4096 32
!ge_sum_no_dopplerr: non Doppler corrected
!gamma spectra for individual rings and all clovers (after conditions)
ge_sum_no_dopplerr[1:24] 16384 32
!ge_sum_no_doppler: non Doppler corrected
!gamma spectra for all rings and all clovers (after conditions)
ge_sum_no_doppler 16384 32
!ge_sum_no_dopplerr2: non Doppler corrected
!gamma spectra for individual rings (after conditions)
ge_sum_no_dopplerr2[1:24] 16384 32

```



```

!ge_sum_no_doppler2: non Doppler corrected
!gamma spectra for all rings (after conditions)
ge_sum_no_doppler2 16384 32
!ge_sum_dopplerr: Doppler corrected
!gamma spectra for individual rings and all clovers (after conditions)
ge_sum_dopplerr[1:24] 16384 32
!ge_sum_doppler: Doppler corrected
!gamma spectra for all rings and all clovers (after conditions)
ge_sum_doppler 16384 32
!ge_sum_dopplerr2: Doppler corrected
!gamma spectra for individual rings (after conditions)
ge_sum_dopplerr2[1:24] 16384 32
!ge_sum_doppler2: Doppler corrected
!gamma spectra for all rings (after conditions)
ge_sum_doppler2 16384 32
!ge_sum_doppleradddb[1:24]: Doppler corrected
!gamma spectra for each ring (after conditions)
ge_sum_doppleradddb[1:24] 16384 32
!ge_sum_doppleradddb: add back Doppler corrected
!gamma spectra for all rings (after conditions)
ge_sum_doppleradddb 16384 32
!si_mat: 2d si matrix (sector energy (x axis) & ring energy (y axis))
si_mat 4096 2d

```

*commands

```

doloop i from 1 to 32 step +1
{
  energys(i) = 0
  ts1(i) = 0
}

```

```

doloop i from 1 to 24 step +1
{
  energyr(i) = 0
  tr1(i) = 0
  sumndr(i) = 0
  sumdr(i) = 0
  sumdrab(i) = 0
}

```

```
}  
  
doloop i from 1 to 8 step +1  
{  
  sum(i) = 0  
  sumnodop(i) = 0  
  sumdop(i) = 0  
  x_cent(i) = 0  
  y_cent(i) = 0  
  z_cent(i) = 0  
  eegdop(i) = 0  
  energyg1(i)=0  
  tg1(i)=0  
  e11ca(i) = 0  
  e11cb(i) = 0  
  e11cc(i) = 0  
  e11cd(i) = 0  
  energyg2(i)=0  
  tg2(i)=0  
  x_1(i) = 0  
  x_2(i) = 0  
  x_3(i) = 0  
  x_4(i) = 0  
  energyg3(i)=0  
  tg3(i)=0  
  y_1(i) = 0  
  y_2(i) = 0  
  y_3(i) = 0  
  y_4(i) = 0  
  energyg4(i)=0  
  tg4(i)=0  
  z_1(i) = 0  
  z_2(i) = 0  
  z_3(i) = 0  
  z_4(i) = 0  
}
```

```
ns = 0
```



```

nr = 0
nga = 0
ngb = 0
ngc = 0
ngd = 0

createlist glist from clover
createlist slist from sect
createlist rlist from ring

gain glist.e1 segA factor 1.00
gain glist.e2 segB factor 1.00
gain glist.e3 segC factor 1.00
gain glist.e4 segD factor 1.00

loopif $g1=glist.e1 gt 0
{
  g = group($g1)
  inc hitpatg(g)
  energyg1(g)=$g1.e1
  inc rclovera($g1.e1) indexed g
  tg=timestampof($g1.e1)
  tg1(g) = timestampof($g1.e1)
  sum(g) = sum(g) + $g1.e1
}
loopif $g2=glist.e2 gt 0
{
  g = group($g2)
  inc hitpatg(g)
  energyg2(g)=$g2.e2
  inc rcloverb($g2.e2) indexed g
  tg=timestampof($g2.e2)
  tg2(g) = timestampof($g2.e2)
  sum(g) = sum(g) + $g2.e2
}
loopif $g3=glist.e3 gt 0

```



```

{
  g = group($g3)
  inc hitpatg(g)
  energyg3(g)=$g3.e3
  inc rcloverc($g3.e3) indexed g
  tg=timestampof($g3.e3)
  tg3(g) = timestampof($g3.e3)
  sum(g) = sum(g) + $g3.e3
}
loopif $g4=glist.e4 gt 0
{
  g = group($g4)
  inc hitpatg(g)
  energyg4(g)=$g4.e4
  inc rcloverd($g4.e4) indexed g
  tg=timestampof($g4.e4)
  tg4(g) = timestampof($g4.e4)
  sum(g) = sum(g) + $g4.e4
}

gain slist.e1 sect factor 1.00
gain rlist.e1 ring factor 1.00

loopif $r=rlist.e1 passes (4509.00,7973.00)
{
  g = group($r) - 52
  inc hitpatr(g)
  energyr(g) = $r.e1
  inc rings($r.e1) indexed g
  tr = timestampof($r.e1)
  tr1(g) = timestampof($r.e1)
  trr1 = tr1(g)
  nr=nr + 1
}

loopif $s=slist.e1 passes (4509.00,7973.00)
{
  g = group($s) - 20

```

```

inc hitpats(g)
energys(g) = $s.e1
inc sectors($s.e1) indexed g
ts = timestampof($s.e1)
ts1(g) = timestampof($s.e1)
tss1 = ts1(g)
ns=ns + 1
}

```

```

td=(ts-tr)+1024
inc timesi(td)

```

```

td=(tg-tr)+1024
inc timeg1(td)

```

```

td=(tg-ts)+1024
inc timeg2(td)

```

```

doloop iii from 1 to 32 step +1

```

```

{
  es = energys(iii)
  tss = ts
  nsss = nss(iii)
  if es gt 10
  {
    ss = iii
    es1 = energys(ss)
  }
}

```

```

if ns eq 1

```

```

{
  nsss = ns
}

```

```

doloop ii from 1 to 24 step +1

```

```

{
  er = energyr(ii)
  trr = tr
  nrrr = nrr(ii)
  if er gt 10
  {

```



```

rr = ii
er1 = energyr(rr)
}
}
if nr eq 1
{
nrrr = nr
}

c_si = nr + ns
td = (tss-trr) +1024
if td passes (990,1013)
{
if c_si eq 2
{
ee = (es1-er1)+1024
inc si_mat(es1,er1)

ee123 = 0
ecad = 0
ee312 = 0
ecbd = 0
ee321 = 0
eccd = 0
ee213 = 0
ecdd = 0
doloop i from 1 to 8 step +1
{
x_cent(i) = d_target2ge*sin(ge_phi(i))*sin(ge_theta(i))
y_cent(i) = d_target2ge*sin(ge_theta(i))
z_cent(i) = d_target2ge*cos(ge_phi(i))*sin(ge_theta(i))
xb = d_target2s3*sin(angdis(rr))*sin(sec_phi(ss))
yb = d_target2s3*cos(angdis(rr))
zb = d_target2s3*sin(angdis(rr))*cos(sec_phi(ss))
ee123 = energyg1(i)
if ee123 gt 10
{
x_1(i)=d_target2ge*sin(crys_a_phi(i))*sin(crys_a_theta(i))
xa = x_1(i)

```



```

y_1(i)=d_target2ge*sin(crys_a_phi(i))
  ya = y_1(i)
z_1(i)=d_target2ge*cos(crys_a_phi(i))*sin(crys_a_theta(i))
  za = z_1(i)
}

caa=(xa*xb+ya*yb+za*zb)/(sqrt(xa*xa+ya*ya+za*za)*sqrt(xb*xb+yb*yb+z*zb))
e11ca(i)=energyg1(i)*(1-beta(rr)*caa)/sqrt(1-beta(rr)*beta(rr))
ecad=e11ca(i)
  tgg = tg1(i)
  trr = tr1(rr)
  tss = ts1(ss)
  tdgs = (tgg - tss) +1024
  tddd = (tgg - trr) +1024
if tdgs passes (1085,1095)
{
if tddd passes (1085,1095)
{
sumdr(rr)=sumdr(rr)+ecad
sumndr(rr)=sumndr(rr)+ee123
sumnodop(i)=sumnodop(i)+ee123
sumdop(i)=sumdop(i)+ecad
}
}

  ee312 = energyg2(i)
if ee312 gt 10
{
x_2(i)=d_target2ge*sin(crys_b_phi(i))*sin(crys_b_theta(i))
  xbb = x_2(i)
y_2(i)=d_target2ge*sin(crys_b_phi(i))
  ybb = y_2(i)
z_2(i)=d_target2ge*cos(crys_b_phi(i))*sin(crys_b_theta(i))
  zbb = z_2(i)
}
cab=(xbb*xb+ybb*yb+zbb*zb)/(sqrt(xbb*xbb+ybb*ybb+zbb*zbb)*sqrt(xb*xb+yb*yb+z*zb))
e11cb(i)=energyg2(i)*(1-beta(rr)*cab)/sqrt(1-beta(rr)*beta(rr))
ecbd=e11cb(i)
  tgg = tg2(i)
  trr = tr1(rr)
  tss = ts1(ss)

```



```

tdgs = (tgg - tss) +1024
tddd = (tgg - trr) +1024
if tdgs passes (1085,1095)
{
if tddd passes (1085,1095)
{
sumdr(rr)=sumdr(rr)+ecbd
sumndr(rr)=sumndr(rr)+ee312
sumnodop(i)=sumnodop(i)+ee312
sumdop(i)=sumdop(i)+ecbd
}
}

ee321 = energyg3(i)
if ee321 gt 10
{
x_3(i)=d_target2ge*sin(crys_c_phi(i))*sin(crys_c_theta(i))
xc = x_3(i)
y_3(i)=d_target2ge*sin(crys_c_phi(i))
yc = y_3(i)
z_3(i)=d_target2ge*cos(crys_c_phi(i))*sin(crys_c_theta(i))
zc = z_3(i)
}
cac=(xc*xb+yc*yb+zc*zb)/(sqrt(xc*xc+yc*yc+zc*zc)*sqrt(xb*xb+yb*yb+zb*zb))
e11cc(i)=energyg3(i)*(1-beta(rr)*cac)/sqrt(1-beta(rr)*beta(rr))
eccd=e11cc(i)
tgg = tg3(i)
trr = tr1(rr)
tss = ts1(ss)
tdgs = (tgg - tss) +1024
tddd = (tgg - trr) +1024
if tdgs passes (1085,1095)
{
if tddd passes (1085,1095)
{
sumdr(rr)=sumdr(rr)+eccd
sumndr(rr)=sumndr(rr)+ee321
sumnodop(i)=sumnodop(i)+ee321
sumdop(i)=sumdop(i)+eccd
}
}
}

```

```

    ee213 = energyg4(i)
if ee213 gt 10
{
x_4(i)=d_target2ge*sin(crys_d_phi(i))*sin(crys_d_theta(i))
  xd = x_4(i)
y_4(i)=d_target2ge*sin(crys_d_phi(i))
  yd = y_4(i)
z_4(i)=d_target2ge*cos(crys_d_phi(i))*sin(crys_d_theta(i))
  zd = z_4(i)
}
cad=(xd*xb+yd*yb+zd*zd)/(sqrt(xd*xd+yd*yd+zd*zd)*sqrt(xb*xb+yb*yb+zb*zb))
e11cd(i)=energyg4(i)*(1-beta(rr)*cad)/sqrt(1-beta(rr)*beta(rr))
ecdd=e11cd(i)
  tgg = tg4(i)
  trr = tr1(rr)
  tss = ts1(ss)
  tdgs = (tgg - tss) +1024
  tddd = (tgg - trr) +1024
if tdgs passes (1085,1095)
{
if tddd passes (1085,1095)
{
sumdr(rr)=sumdr(rr)+ecdd
sumndr(rr)=sumndr(rr)+ee213
sumnodop(i)=sumnodop(i)+ee213
sumdop(i)=sumdop(i)+ecdd
}
}

  sndop = sumnodop(i)
  sndopr = sumndr(rr)
  sdop = sumdop(i)
  sdopr = sumdr(rr)

if sndop passes (1,16384)
{
inc ge_sum_no_dopplerr(sndop) indexed rr
inc ge_sum_no_doppler(sndop)
}
if sndopr passes (1,16384)

```

```

{
inc  ge_sum_no_dopplerr2(sndopr) indexed rr
inc  ge_sum_no_doppler2(sndopr)
}

if sdop passes (1,16384)
{
inc  ge_sum_dopplerr(sdop) indexed rr
inc  ge_sum_doppler(sdop)
}
if sdopr passes (1,16384)
{
inc  ge_sum_dopplerr2(sdopr) indexed rr
inc  ge_sum_doppler2(sdopr)
}
eegdop(i)=e11ca(i) + e11cb(i) + e11cc(i) + e11cd(i)
eegdop1 = eegdop(i)
tddd = (tg - trr) +1024
if tddd passes (1085,1095)
{
sumdrab(rr)=sumdrab(rr)+eegdop1
}
sdopaddb = sumdrab(rr)
if sdopaddb passes (1,16364)
{
inc  ge_sum_doppleraddbb(sdopaddb) indexed rr
inc  ge_sum_doppleraddb(sdopaddb)
}
}

}

*runfiles

*finish

```

A.7 Input file example

668.21	0.00	0.00	11675.93	681.50	0.00	0.00	-0.69	0.41
682.31	0.00	0.00	11466.89	681.20	0.00	0.00	-0.21	0.55
674.27	0.00	0.00	11418.97	681.00	0.00	0.00	-1.37	0.39
677.92	0.00	0.00	11309.90	662.30	0.00	0.00	-1.13	0.39
669.34	0.00	0.00	11242.82	661.20	0.00	0.00	-1.28	0.37
677.01	0.00	0.00	11412.75	670.10	0.00	0.00	-1.71	0.57
649.68	0.00	0.00	11407.19	660.30	0.00	0.00	-1.72	0.56
673.37	0.00	0.00	11435.24	671.80	0.00	0.00	-3.42	0.80
662.33	0.00	0.00	12050.01	660.00	0.00	0.00	-2.80	0.59
674.59	0.00	0.00	11921.93	679.10	0.00	0.00	0.23	0.38
670.42	0.00	0.00	12245.41	675.40	0.00	0.00	-1.75	0.54
673.15	0.00	0.00	12275.66	670.70	0.00	0.00	-1.89	0.47
683.55	0.00	0.00	12156.55	660.60	0.00	0.00	-0.95	0.40
663.90	0.00	0.00	11935.49	669.10	0.00	0.00	-0.87	0.37
648.78	0.00	0.00	11995.59	679.90	0.00	0.00	-1.31	0.57
671.30	0.00	0.00	11976.25	670.90	0.00	0.00	-1.82	0.54
660.15	0.00	0.00	11674.54	664.00	0.00	0.00	-1.16	0.38
667.92	0.00	0.00	11667.89	664.00	0.00	0.00	-1.78	0.56
666.37	0.00	0.00	11456.33	661.10	0.00	0.00	0.32	0.41
656.23	0.00	0.00	11188.07	660.70	0.00	0.00	-0.71	0.37
666.17	0.00	0.00	11289.52	669.00	0.00	0.00	-2.18	0.57
648.90	0.00	0.00	11653.14	674.60	0.00	0.00	-1.17	0.67
646.07	0.00	0.00	11655.27	672.30	0.00	0.00	-0.63	0.36
646.07	0.00	0.00	11634.28	668.50	0.00	0.00	-1.75	0.55
0.00	0.00	0.00	11520.61	662.00	0.00	0.00	-0.66	0.36
0.00	0.00	0.00	11388.69	675.80	0.00	0.00	-1.21	0.60
0.00	0.00	0.00	11544.86	671.00	0.00	0.00	-1.75	0.54
0.00	0.00	0.00	11394.01	680.50	0.00	0.00	-0.44	0.41
0.00	0.00	0.00	11537.18	673.10	0.00	0.00	-1.07	0.42
0.00	0.00	0.00	11478.13	675.60	0.00	0.00	-1.24	0.39
0.00	0.00	0.00	11478.13	675.60	0.00	0.00	-0.28	0.38
0.00	0.00	0.00	11478.13	675.60	0.00	0.00	-1.00	0.37
0.00	0.00	0.00	0.00	0.00	0.00	0.00	-1.79	0.57
0.00	0.00	0.00	0.00	0.00	0.00	0.00	-1.03	0.53
0.00	0.00	0.00	0.00	0.00	0.00	0.00	-0.30	0.36
0.00	0.00	0.00	0.00	0.00	0.00	0.00	-0.84	0.36

Appendix B

Non-relativistic kinematics

This appendix presents the non-relativistic kinematics implemented in the sorting code to perform the particle energy calibrations, the calculation of β values as well as the calculations of the projectile and target scattering angles that are used in the Doppler corrections.

Consider the diagrammatic representation of the two-body scattering problem, in which a particle of mass, m_p , having an initial velocity, $u_{p,i}$, collides inelastically with a stationary particle of mass m_t shown in figure B.1. Given the energies of the incident particles as well as their masses the non-relativistic two-body scattering problem involves finding the changes in the energies and momenta of the particles before and after the scattering process using the conservation of energy and momentum under the assumption that any interactions between the m_t and m_p occur at very small distances. so that the problem can be solved using the methods of classical mechanics.

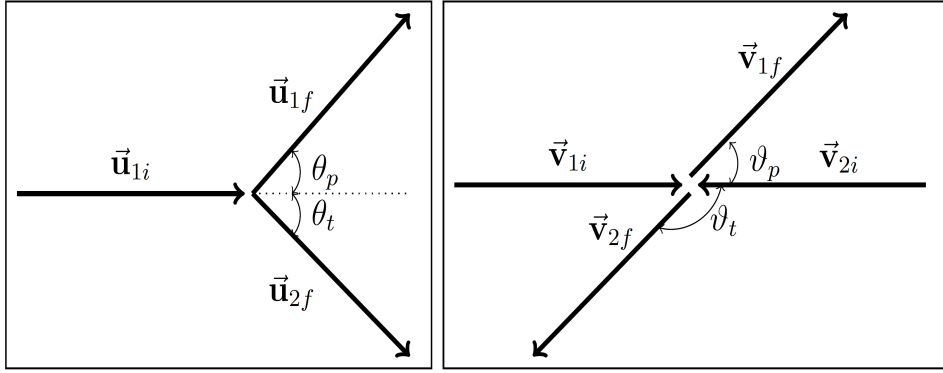


Figure B.1: Two-body scattering in the lab (left) and center of mass (right) frames.

The notation that will be used for the variables in these equations are as follows, in the center of mass (*CM*) frame $v_{p,i}$ denotes the magnitude of the initial projectile velocity, $v_{t,i}$ denotes the magnitude of the initial target velocity, ϑ_p and ϑ_t denote the scattering angles of the projectile and target after the collision, while the magnitudes of the final velocities of the projectile and target nuclei are $v_{p,f}$ and $v_{t,f}$ respectively. The initial and final energies of the projectile will be denoted by E_{pci} and E_{pcf} , while the initial and final target energies will be denoted by E_{tci} and E_{tcf} .

In the laboratory frame, $u_{p,i}$ denotes the magnitude of the initial projectile velocity, $u_{t,i}$ denotes the magnitude of the initial target velocity which is zero since m_t is at rest in the laboratory frame, θ_p and θ_t denote the scattering angles of m_p and m_t after the collision, while the magnitudes of the final velocities of the projectile and target nuclei in the laboratory frame are $u_{p,f}$ and $u_{t,f}$ respectively. The projectile energy in the laboratory frame prior to the collision will be denoted by E_p , while the energies of m_t and m_p in the laboratory frame after the collision will be denoted by E_{tlf} and E_{plf} , respectively. In addition, subscripts including 1 represent a projectile variable, while subscripts including a 2 denote a target variable.

In the *CM* frame, the total momenta of the particles before and after the collision are zero, so

$$\sum_{k=1}^2 m_k \vec{v}_{k,i} = \vec{0} \quad \text{and} \quad \sum_{k=1}^2 m_k \vec{v}_{k,f} = \vec{0} \quad (\text{B.1})$$

The summations in equation B.1 can be used to show that

$$v_{t,i} = \frac{m_p}{m_t} v_{p,i} \quad \text{and} \quad v_{t,f} = \frac{m_p}{m_t} v_{p,f} \quad (\text{B.2})$$

here the expression for $v_{t,f}$ can be obtained by using the x-component of $v_{t,f}$ in conjunction with that fact that $\vartheta_t = \pi - \vartheta_p$ to eliminate $\cos(\vartheta_t)$ from the expression of $v_{t,f}$. The conservation of energy in CM frame which is given by:

$$\frac{1}{2} \sum_{k=1}^2 m_k v_{k,i}^2 + Q = \frac{1}{2} \sum_{k=1}^2 m_k v_{k,f}^2 \quad (\text{B.3})$$

where Q denotes the additive inverse of the excitation energy ΔE . By using the result of equation B.2 equation B.3 can be expressed as

$$\frac{m_t + m_p}{2} m_p v_{p,i}^2 - \Delta E = \frac{m_t + m_p}{2} m_p v_{p,f}^2 \quad (\text{B.4})$$

since $\vec{v}_{p,i}$ and $\vec{u}_{p,f}$ are related by

$$\vec{v}_{p,i} = \vec{u}_{p,f} - \vec{V}_{CM} \quad (\text{B.5})$$

where $\vec{V}_{CM} = \frac{m_p}{m_t + m_p} \vec{u}_{p,i}$, the magnitude of $\vec{v}_{p,i}$ can be expressed as

$$v_{p,i} = \frac{m_t}{m_p + m_t} u_{p,i} \quad (\text{B.6})$$

by inserting equation B.6 into equation B.4 $E_{pcf} = \frac{1}{2} m_p v_{p,f}^2$ can be expressed in terms of m_p , m_t , E_p and ΔE as follows

$$E_{pcf} = \left(\frac{m_t}{m_p + m_t} \right)^2 \epsilon_b \quad (\text{B.7})$$

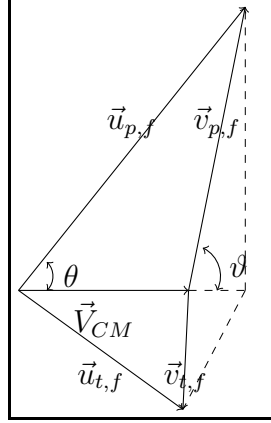
where

$$\epsilon_b = E_p - \left(1 - \frac{m_p}{m_t} \right) \Delta E \quad (\text{B.8})$$

is the reduced bombarding energy [7], so that $v_{p,f}$ and $v_{t,f}$ can be expressed in terms m_p , m_t and ϵ_b as

$$v_{p,f} = \left(\frac{m_t}{m_t + m_p} \right) \sqrt{\frac{2}{m_p} \epsilon_b} \quad \text{and} \quad v_{t,f} = \left(\frac{m_p}{m_t + m_p} \right) \sqrt{\frac{2}{m_p} \epsilon_b} \quad (\text{B.9})$$

The energies in the CM frame can now be transformed to lab frame. By considering the CM frame as the stationary inertial frame of reference and defining the lab frame to be the inertial frame of reference moving with


 Figure B.2: Lab and CM frame angles.

uniform velocity $\vec{V}_{CM} = \vec{v}_{t,i}$ relative to the CM frame in which m_t is rest. The energy of m_p in lab frame after the collision, E_{plf} , can then be found by using the geometric relations of the magnitudes of \vec{V}_{CM} , $u_{p,i}$ and $v_{p,f}$ together with figure B.2. The cosine rule and the cosine of θ_p can be used in conjunction with B.2 figure to express $u_{p,f}$ in terms of V_{CM} , $v_{p,f}$ and $\cos(\vartheta_p)$, as follows

$$u_{p,f}^2 = v_{p,f}^2 + 2V_{CM}v_{p,f} \cos(\vartheta_p) + V_{CM}^2 \quad (\text{B.10})$$

here the cosine rule was used to express $v_{p,f}^2$ in terms of $u_{p,f}$, V_{CM} and $\cos(\theta_p)$, which gave

$$v_{p,f}^2 = u_{p,f}^2 - 2V_{CM}u_{p,f} \cos(\theta_p) + V_{CM}^2 \quad (\text{B.11})$$

The cosine of θ_p was then eliminated from equation B.11, by using figure B.2, which gives,

$$\cos(\theta_p) = \frac{V_{CM} + u_{p,f} \cos(\vartheta_p)}{u_{p,f}} \quad (\text{B.12})$$

Since $\vec{V}_{CM} \parallel \vec{u}_{p,i}$ and $E_p = \frac{1}{2}m_p u_{p,i}^2$, V_{CM}^2 may be written as

$$\vec{V}_{CM} \cdot \vec{V}_{CM} = \left(\frac{m_p}{m_p + m_t} \right)^2 2 \frac{E_p}{m_p} \quad (\text{B.13})$$

so that equation B.10 can be expressed as

$$u_{p,f}^2 = \left(\frac{m_t}{m_p + m_t} \right)^2 \epsilon_b \left[\frac{2}{m_p} + \frac{4}{m_t} \sqrt{\frac{E_p}{\epsilon_b}} \cos(\vartheta_p) + \left(\frac{m_p}{m_t} \right)^2 \frac{2}{m_p} \frac{E_p}{\epsilon_b} \right] \quad (\text{B.14})$$

by multiplying equation B.14 by $\frac{m_p}{2}$, E_{plf} can be expressed as

$$E_{plf} = \left(\frac{m_t}{m_p + m_t} \right)^2 \epsilon_b \left[1 + 2 \frac{m_p}{m_t} \sqrt{\frac{E_p}{\epsilon_b}} \cos(\vartheta_p) + \left(\frac{m_p}{m_t} \right)^2 \frac{E_p}{\epsilon_b} \right] \quad (\text{B.15})$$

and $E_{ulf} = \frac{m_p}{m_t^2}$, so that

$$E_{ulf} = \left(\frac{m_p m_t}{(m_p + m_t)^2} \right) \epsilon_b \left[1 + 2 \frac{m_p}{m_t} \sqrt{\frac{E_p}{\epsilon_b}} \cos(\vartheta_p) + \left(\frac{m_p}{m_t} \right)^2 \frac{E_p}{\epsilon_b} \right] \quad (\text{B.16})$$

The expressions for the *CM* frame angles in terms of the lab angles and vice-versa can be found using figure B.2. If ϑ and θ are arbitrary angles in the *CM* and lab frames, then ϑ can be expressed as a function of θ in the following manner,

$$\vartheta(\theta) = \theta + \sin^{-1} \left(\frac{\sin(\theta)}{\gamma} \right) \quad (\text{B.17})$$

so that

$$\vartheta_p(\theta) = \theta + \sin^{-1} \left(\frac{\sin(\theta)}{\gamma} \right) \quad (\text{B.18})$$

and $\vartheta_t(\theta) = \pi - \vartheta_p(\theta)$. The expression for θ as a function of *vartheta* can be expressed as

$$\theta(\vartheta) = \tan^{-1} \left(\frac{\sin(\vartheta)}{\frac{1}{\gamma} + \cos(\vartheta)} \right) \quad (\text{B.19})$$

so that

$$\theta_p(\vartheta) = \tan^{-1} \left(\frac{\sin(\vartheta)}{\frac{1}{\gamma} + \cos(\vartheta)} \right) \quad (\text{B.20})$$

here $\gamma = \frac{m_p}{m_t} \sqrt{\frac{E_p}{\epsilon_b}}$ and $\theta_t(\theta) = \pi - \theta_p(\vartheta)$. The calibrations of the rings and sections are carried out using equations B.15 and subtracting energy loss discussed in chapter 4 using the $\frac{dE}{dx}$ obtained from *SRIM* [50] with $\Delta E = 0$ since these represent the elastic peaks, while the β values are obtained using equation B.14.



UNIVERSITY *of the*
WESTERN CAPE

Appendix C

S3 detector tables

C.1 S3 detector ring radii

Ring	r_{min} (mm)	r_{max} (mm)
1	11.48	12.366
2	12.466	13.352
3	13.452	14.338
4	14.438	15.324
5	15.424	16.31
6	16.41	17.296
7	17.396	18.282
8	18.382	19.268
9	19.368	20.254
10	20.354	21.24
11	21.34	22.226
12	22.326	23.212
13	23.312	24.198
14	24.298	25.184
15	25.284	26.17
16	26.27	27.156
17	27.256	28.142
18	28.242	29.128
19	29.228	30.114
20	30.214	31.1
21	31.2	32.086
22	32.186	33.072
23	33.172	34.058
24	34.158	35.044

S3 detector inner (r_{min}) and outer (r_{max}) ring radii.

C.2 S3 detector cabling

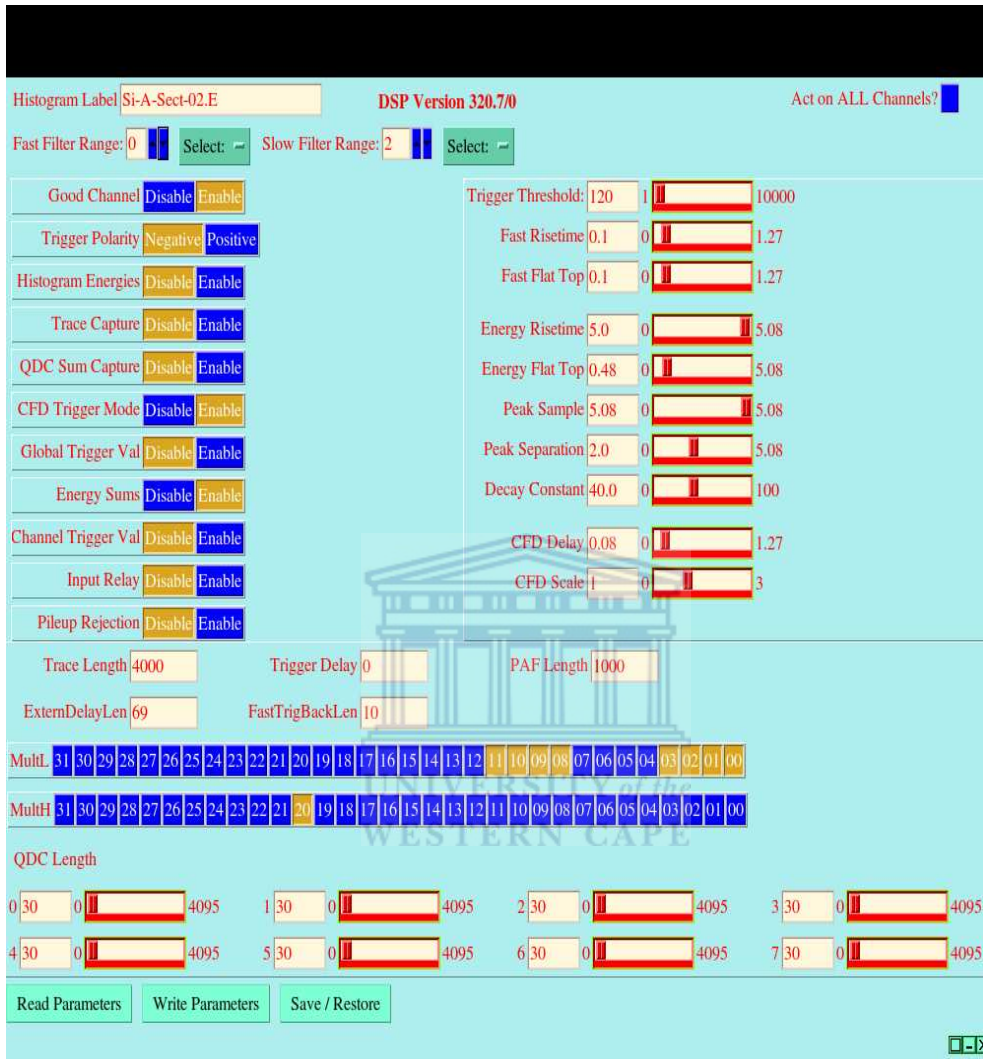
C.2.1 Ring cabling

Ring #	Cable	Patch panel	DDAS module #	DDAS channel #
Ring1	R2	2.6	2	4
Ring2	R2	2.7	2.1	4.1
Ring3	R2	2.8	2.2	4.2
Ring4	R2	15.2	2.3	4.3
Ring5	R2	15.3	2.4	4.4
Ring6	R2	15.4	2.5	4.5
Ring7	R2	15.5	2.6	4.6
Ring8	R2	15.6	2.7	4.7
Ring9	R2	15.7	2.8	4.8
Ring10	R2	15.8	2.9	4.9
Ring11	R2	9.2	2.1	4.1
Ring12	R2	9.3	2.11	4.11
Ring13	R2	9.4	2.12	4.12
Ring14	R2	9.5	2.13	4.13
Ring15	R2	9.6	2.14	4.14
Ring16	R2	9.7	2.15	4.15
Ring17	R1	9.8	3	5
Ring18	R1	3.2	3.1	5.1
Ring19	R1	3.3	3.2	5.2
Ring20	R1	3.4	3.3	5.3
Ring21	R1	3.5	3.4	5.4
Ring22	R1	3.6	3.5	5.5
Ring23	R1	3.7	3.6	5.6
Ring24	R1	3.8	3.7	5.7

C.2.2 Sector cabling

Sector #	Cable	Patch panel	DDAS module #	DDAS channel #
Sector1	S2	14.2	2	0
Sector2	S2	14.3	2.1	0.1
Sector3	S2	14.4	2.2	0.2
Sector4	S2	14.5	2.3	0.3
Sector5	S2	14.6	2.4	0.4
Sector6	S2	14.7	2.5	0.5
Sector7	S2	14.8	2.6	0.6
Sector8	S2	8.2	2.7	0.7
Sector9	S2	8.3	2.8	0.8
Sector10	S1	8.4	2.9	0.9
Sector11	S1	8.5	2.1	0.1
Sector12	S1	8.6	2.11	0.11
Sector13	S1	8.7	2.12	0.12
Sector14	S1	8.8	2.13	0.13
Sector15	S1	7.2	2.14	0.14
Sector16	S1	7.3	2.15	0.15
Sector17	S1	7.4	3	1
Sector18	S1	7.5	3.1	1.1
Sector19	S1	7.6	3.2	1.2
Sector20	S1	7.7	3.3	1.3
Sector21	S1	7.8	3.4	1.4
Sector22	S1	6.2	3.5	1.5
Sector23	S1	6.3	3.6	1.6
Sector24	S1	6.4	3.7	1.7
Sector25	S1	6.5	3.8	1.8
Sector26	S2	6.6	3.9	1.9
Sector27	S2	6.7	3.1	1.1
Sector28	S2	6.8	3.11	1.11
Sector29	S2	2.2	3.12	1.12
Sector30	S2	2.3	3.13	1.13
Sector31	S2	2.4	3.14	1.14
Sector32	S2	2.5	3.15	1.15

C.3 MIDAS digital parameters



Digital parameters used for S3 detector.

Bibliography

- [1] E. Clement et al., Phys. Rev. C **75**, (2007).
- [2] R. H. Spear, Phys. Rep. **73**, 369 (1980).
- [3] D. C. Kean, Lecture Notes in Physics (Springer), Volume **92**, 80 (1976).
- [4] A. Bohr and B. R. Mottelson, Mat. Fys. **27**, no. 16, 8-27 (1953).
- [5] S. Yeager and L. Zamick, arXiv: 0807.4679 (2008).
- [6] S. J. Q. Robinson et al., Phys. Rev. C **73**, 037306 (2006).
- [7] J. de Boer, J. Eichler, Advances in Nuclear Physics (Springer), **1**, 1-65 (1968).
- [8] K. Nakai, F. S. Stephens and R. M. Diamond, Nucl. Phys. A **150**, 114-128 (1970).
- [9] D. Schwalm et al., Nucl. Phys. A **192**, 449-495 (1972).
- [10] D. K. Olsen, A. R. Barnett, S. F. Biagi, N. H. Merrill and W. R. Phillips, Nucl. Phys. A **220**, 541-568 (1974).
- [11] N. J. Stone, At. Data Nucl. Data Tables **90**, 75-176 (2005).
- [12] S. Raman, C. W. Nestor, Jr. and P. Tikkanen, At. Data Nucl. Data Tables **78**, 1-128 (2001).
- [13] NNDC Nuclear Data Base: <http://www.nndc.bnl.gov>.
- [14] M. Freer, Rep. Prog. Phys. **70**, 2149 (2007).
- [15] J. P. Ebran, E. Khan, T. Niksic, and D. Vretenar, Nature **11246**, (2012).
- [16] H. Morinaga, Phys. Rev. **101**, 254 (1956).
- [17] T. Kibedi and R. H. Spear, At. Data Nucl. Data Tables **89**, 77 (2005).

- [18] G. A. Lalazissis, T. Niksic, D. Vretenar, and P. Ring, Phys. Rev. C **71**, 024312 (2005).
- [19] E. Chabanat, P. Bonche, P. Haensel, J. Meyer, and R. Schaeffer. Nucl. Phys. A **635**, 231–256 (1998).
- [20] D. Cline, H. S. Gertzman, H. E. Gove, P. M. S. Lesser and J. J. Schwartz, Nucl. Phys. A **133**, 445. (1969).
- [21] K. Alder and A. Bohr, *Study of Nuclear Structure by Electromagnetic Excitation with accelerated Ions*, Rev. Mod. Phys. **28**, 433-437 (1967).
- [22] N. Zettili, *Quantum Mechanics*, 2nd edition, Wiley, (2009).
- [23] K. Alder, A. Winther, Mat. Fys. **32**, no. 8, 5-6 (1960).
- [24] K. Alder, A. Winther, Mat. Fys. **31**, no. 1, (1956).
- [25] T. Czosnyka, D. Cline, and C. Y. Wu, Bull. Am. Phys. Soc. **28**, 745 (1983).
- [26] T. Czosnyka, D. Cline, C. Y. Wu, A. B. Hayes, *Gosia user manual for simulation and analysis of Coulomb excitation experiments*, 97-98 (2012).
- [27] T. Czosnyka, D. Cline, C. Y. Wu, A. B. Hayes, *Gosia user manual for simulation and analysis of Coulomb excitation experiments*, 15-98 (2012).
- [28] W. R. Leo, *Techniques for nuclear and particle physics experiments*, Springer, (1867).
- [29] J. B. Marion and F. C. Young, *Nuclear reaction analysis, Graphs and tables*, Wiley, (1968).
- [30] N. R. Erasmus, *Simulation of Silicon and Diamond detector systems by Geant4 simulation techniques*, UWC (2014).
- [31] <http://geant4.web.cern.ch/geant4/UserDocumentation/UsersGuides/PhysicsReferenceManual/fo/PhysicsReferenceManual.pdf>
- [32] S. Agostinelli et al., Nucl. Instr. Meth. A, **506**, 250 (2003).
- [33] J. Apostolakis et al., Rad. Phys. Chem. **78**, 859 (2009).
- [34] A. N. Ostrowski et al., Nucl. Instr. Meth. A, **40**, 448-A55 (2002).
- [35] G. Duchene et al., Nucl. Instr. Meth. A **432**, 90-110 (1999).

- [36] P. M. Jones et al., Nucl. Instr. Meth. A **362**, 556-560 (1995).
- [37] <http://npsg.dl.ac.uk/MIDAS/>.
- [38] J. Cresswell and J. Sampson, *MTsort Language-EDOC033*, <http://ns.ph.liv.ac.uk/MTsort-manual/MTsort.html>, (2015).
- [39] <http://www.canberra.com/products/detectors/pdf/Clover-Detector-C39840.pdf>.
- [40] D. Cline, H. S. Gertzman, H. E. Gove, P. M. S. Lesser, and J. J. Schwartz, Nucl. Phys. A. **133**, 445 (1969).
- [41] M. P. Fewell, S. Hinds, D. C. Kean, T. H. Zabel, Nucl. Phys. A **319**, 214 (1979).
- [42] R. H. Spear, T. H. Zabel, D. C. Kean *Systematics of Coulomb-Nuclear interference: Implications for a reliable measurement of the reorientaion effect*, Phys. Lett. B **76**, 559-561 (1978).
- [43] P. M. Jones, R. A. Bark, *Development of the iThemba LABS Digital Data Acquisition System iThemba LABS annual report*, (2003).
- [44] I. Lazarus et al., IEEE Trans. Nucl. Sci., **48(3)**, 567-569 (2001).
- [45] <http://www.mesytec.com/datasheets/MPR16.pdf>.
- [46] <http://www.mesytec.com/datasheets/MHV4.pdf>.
- [47] <http://www.mesytec.com/datasheets/MSCF-16-F.pdf>.
- [48] D. C. Radford, Nucl. Instr. Meth. Phys. Rev. A **361**, 297 (1995).
- [49] J. N. O'rae et al., Phys. Rev. C **86**, 041303(R) (2012).
- [50] J. F. Ziegler, J. P. Biersack, M. D. Ziegler, <http://www.srim.org>.